OPEN ACCESS

EUROPEAN MECHANICAL SCIENCE

E-ISSN: 2587-1110

2024 | Vol. 8(2)

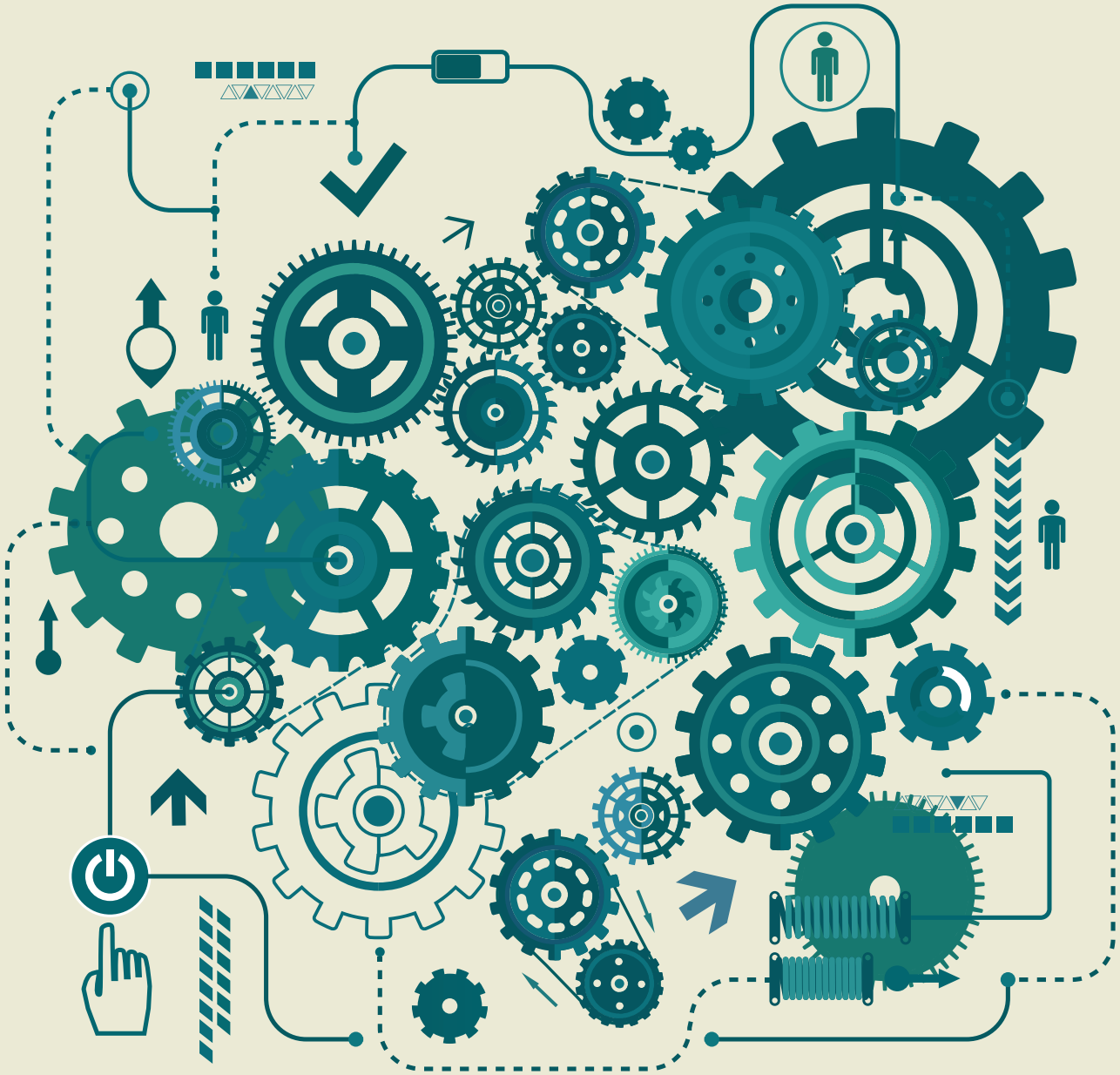

https://dergipark.org.tr/ems

TR DİZİN

EUROPEAN MECHANICAL SCIENCE
e-ISSN: 2587-1110

Indexed / Abstracted in:

TR-Dizin, Scilit, EXALY Full-Text Search Engine, Index Copernicus, Root Indexing, Google Scholar, Harvard, journaltocs, Sobiad, Fatcat, Cite Factor, WorldCat, Freien Universität Berlin, Crossref, DTU Findit, The Open Ukrainian Citation Index (OUCI), Paperity Open Science, Asian Science Citation Index

Aims and Scopes

European Mechanical Science (EMS) is an international, peer reviewed journal which publishes full length original research papers, reviews related to all areas of Mechanical Engineering such as: Solid Mechanics, Materials Engineering, Automotive Engineering, Fluid Mechanics, Thermal Engineering, Engine and Power Engineering, Dynamics & Control, Robotics & Mechatronics, Transportation Engineering, Computational Mechanics, Design, Systems, Manufacturing, BioMedical Engineering; Process Engineering, Aerospace Engineering. No charges are required from the Authors to publish the articles.EMS is a quarterly published journal operating an online submission and peer review system. It allows authors to submit articles online and track their progress via its web interface.

https://dergipark.org.tr/ems

Contents

– *Research Articles*

– *Review Articles*

EUROPEAN MECHANICAL SCIENCE

Research Article

e-ISSN: 2587-1110

Finite element stress analysis and topological optimization of a commercial aircraft seat structure

Christian Dalo Amaze[1], Sireetorn Kuharat[1]*, O. Anwar Bég[1], Ali Kadir[1], Walid Jouri[1], Tasveer A. Bég[2]

[1]MPESG, Corrosion Lab, 3-08, Mechanical Engineering Dept., Salford University, Manchester, M54WT, United Kingdom
[2]Engineering Mechanics Research, Israfil House, Dickenson Rd., Manchester, United Kingdom

Orcid: C.D. Amaze (0009-0005-2696-4195), S. Kuharat (0009-0000-5739-9137), O.A. Beg (0000-0001-5925-6711), A. Kadir (0000-0001-5122-8345)

Abstract: In recent years, the Finite Element Method (FEM) has emerged as a cornerstone in the field of seating design, particularly within the aircraft industry. Over the past decade, significant advancements in Finite Element (FE) analysis techniques have revolutionized the seat industry, enabling the creation of safer and more cost-effective seat designs. The accuracy of FE analysis plays a pivotal role in this transformation. In the process of constructing a reliable finite element model, the selection and precise manipulation of key parameters are paramount. These crucial parameters encompass element size, time scale, analysis type, and material model. Properly defining and implementing these parameters ensures that the FE model produces accurate results, closely mirroring real-world performance. Verification of Finite Element Analysis (FEA) results is commonly accomplished through experimental methods. Notably, when the parameters are appropriately integrated into the modelling process, FE analysis outcomes closely align with experimental results. This study aims to leverage the power of FEM in performing static stress analysis and topology optimization of aircraft seats using the SOLIDWORKS commercial finite element platform. By simulating loading conditions, this research calculates static stresses and displacements experienced by the aircraft seat. For AL7075-T6(SN) the structural analysis demonstrates that this material had a maximum stress of 125.2 N/mm^2 and a minimum stress of 0.0039 N/mm^2. Due to its strong 4.034 factor of safety, the component may have been over-engineered for its intended use. However, at 2.32 kg, the component's mass and $2.304/kg material cost showed a high design cost. The maximum Y-component of displacement was 0.0606 mm, which was acceptable but could have been optimized to decrease material use and expense without affecting structural integrity. After performing topology optimization on Simulation 1 of AL7075-T6(SN), several improvements have been achieved. The maximum stress sustained by the component has been elevated to 189.4 N/mm^2. However, it is worth noting that the minimum stress has also risen, although to a negligible value of 0.0006 N/mm^2. The compromise in this scenario is characterized by a fall in the factor of safety to 2.666, suggesting a design that is more optimal but possibly associated with more risk. The most notable improvements, however, concern weight reduction. The overall mass of the component saw a substantial reduction, reaching 1.89 kg, which represents a notable improvement on the original design. Through a comprehensive topology optimization study, the weight of the airplane seat is remarkably reduced by up to 30%, while still prioritizing passenger safety. The success of this optimization showcases the potential for substantial weight savings in aircraft seat design without compromising safety standards.

Keywords: Finite Element Method (FEM), Aircraft Seat Industry, FE Analysis, Static Stress Analysis, Topology Optimization, Experimental Validation, Material Model, Safety Standards, Weight Reduction, Seating Design.

1. Introduction

The aircraft seat refers to the seating area where passengers sit during their flight journey. These aircraft seats are typically arranged in rows along seat tracks inside the plane. When it comes to aircraft seats, they come with various fundamental characteristics for comfort, functionality and carefully designed features [1]. Since the 1930s when the first passenger airplane was introduced, aircraft manufacturers have been making continuous efforts to ensure the safety of passengers and crew during

*Corresponding author:
Email: S.Kuharat2@salford.ac.uk

Cite this article as:
Amaze, C., Kuharat, S., Bég, O., Kadir, A., Jouri, W., Bég, T. (2024). Finite element stress analysis and topological optimization of a commercial aircraft seat structure. *European Mechanical Science*, *8*(2): 54-70. https://doi.org/10.26701/ems.1441584

History dates:
Received: 28.02.2024, *Revision Request*:11.03.2024, *Last Revision Received*: 12.03.2024, *Accepted*: 15.03.2024

their flights. Safety-related aircraft seat requirements should be considered in 3 major cases: take-off, cruise, and landing. Thus, international flight authorities such as the Federal Aviation Administration (FAA), European Aviation Safety Agency (EASA) and Joint Aviation Authorities (JAA) have implemented strict rules during these three cases [2].

The weight of the aircraft seat also contributes to the total weight of the aircraft, hence why it is recommended to use lightweight materials during the design and manufacturing process. Since the aircraft seat is the focus of comfort for the passengers, it is essential to design a lightweight seat without creating additional load on the aircraft while simultaneously retaining the strength of the seat [3]. The vast majority of aircraft seat manufacturers use aluminium as the main component, although in recent times, carbon composite structures and plastics have been introduced for the sole purpose of reducing weight while maintaining strength. Other manufacturers combine all three materials to produce different types of seat structures. One example of a manufacturer that uses the latter is Avio Interiors [4]. This Italian company claims that the combination of carbon fibre composites and aluminium produces stronger seats rather than using both materials individually. The seats of an aircraft can be designed in various shapes, sizes, and comfort levels depending on the type of aircraft. Commercial aircraft have mainly four classes of seats namely, first-class seats, business-class seats, premium seats, and economy seats. These classes of aircraft seats have various features that vary depending on the ticket price. The 4 main types of commercial aircraft seat are shown Figure 1.

This article focuses on the *computational stress analysis and topological optimization of the support structure of an aircraft seat.* As such this study aims to achieve a better-optimized structure for the base frame assembly of an aircraft seat.

When designing an aircraft seat, the comfort of the passenger must be taken as a priority. In that sense, factors such as the number of seats, space limitations, and location of each seat must be considered. Generally, the most used material for a passenger seat base frame is aluminum. This aluminum material is assembled to form a seat base, seat back, center armrest, and cushion space.

The primary structure for aircraft passenger seats typically consists of two stretcher tubes or rails that span the front and rear of the seat [5]. These stretcher tubes support spreader members, which run along opposite sides of the seat and provide support for the seat cushions and seat backs. Additionally, leg assemblies are positioned at intervals along the length of the stretcher tubes and are connected to tracks mounted on the floor to provide further support for the seats. Depending on the number of seats and the layout, the stretcher tubes' spreaders and legs will be spaced at varying intervals along the length of the tubes. Depending on the layout of the aircraft, the number of seats in a row, and the placement of the row in the aircraft, the legroom at the end of the row may be different from that at the beginning of the row. Whether the seat faces forward or backwards, where the legs are attached to the stretcher tubes, and where the spreaders are attached to the stretcher tubes all affect the quality of the connection between the spreaders and the stretcher tubes, as well as the leg assemblies [6].

To ensure safety, it is imperative to fulfil the essential structural prerequisites, while simultaneously enabling the airline operator to both efficiently and economically maintain the seating arrangements. Frequently, there arises a need to modify the arrangement of seats within an aircraft to accommodate various passenger requirements and adapt to market demands. Historically, the process of assembling and disassembling seats has been intricate, laborious, and costly [7]. Frequently, it necessitated the disassembly of a significant portion of the seat support structure to facilitate the movement or alteration of the seating arrangement. Additionally, any decrease in seat weight that does not compromise the structural va-

Figure 1. Top left- economy class, top right- premium economy class, below left- business class, below right- first class.

lidity of the seats results in fuel savings for the airline's aircraft and a reduction in maintenance costs.

The objective of this study is to introduce an enhanced structure for supporting aircraft seats, wherein the base frame structure can be efficiently and effortlessly attached or detached from the remaining support structure, without compromising the seat's structural integrity. Another objective of the study is to offer an enhanced structure for supporting aircraft seats while minimizing the number of components involved. Finally, this study aims to offer an aircraft seat support structure that can fulfil the standard safety requirements while also being lightweight. In summary, the standard configuration of an airplane seat base frame consists of a front leg structure designed to support a front horizontal stretcher component and a rear leg structure intended to support a rear horizontal stretcher component. The aircraft seat industry plays a pivotal role in ensuring passenger comfort, safety, and satisfaction during air travel. Over the past decade, the use of Finite Element Method (FEM) in the design and analysis of aircraft seats has seen significant growth, revolutionizing the industry's approach to seat development. A detailed literature review explores the critical aspects of FEM utilization in the aircraft seat industry, emphasizing its impact on design efficiency, safety, and weight optimization. The standard class passenger seat used in this research was modelled with the help of SolidWorks software, a computer-aided drawing tool which utilizes the FEM to conduct static analysis on the computer-aided design (CAD) model under various loading and boundary conditions.

2. Finite Element Method Approach

The fundamental principle underlying the FEM involves the process of simplifying a complex problem to facilitate its solution [8]. This technique involves discretizing the domain under investigation into a series of smaller, easier-to-manage components using finite elements and subsequently reconnecting these elements at specific locations referred to as nodes. The FEM is an effective tool for predicting displacements, stresses, and strains in a structure subjected to a given set of loads and is thus widely used in structural analysis. This is exactly the topic that we want to investigate more in this report [9]. To facilitate the essential simulations of finite element analysis, it is imperative to generate a mesh comprising numerous minute elements that collectively define the structural configuration. Each component requires its own set of calculations, the sum of which gives the overall result for the entire structure. There are three distinct phases to the finite element analysis procedure: preprocess, process, and post-process. During the preprocessing, it is paramount to select the type of analysis. For this study, static-structural, topological, and frequency analyses are performed in SOLIDWORKS. The initial phase in the problem-solving process entails the discernment and delineation of the problem at hand. Therefore, before commencing the analysis of a structure, we must inquire about the following questions: What are the primary physical phenomena that exert a significant influence on structural integrity? Does the problem exhibit characteristics of static or dynamic behavior. Do motions or material properties exhibit linearity or non-linearity? What are the specific key results that have been requested? What is the desired level of precision being pursued? The responses to these inquiries are of utmost importance in the process of determining an appropriate structural model.

To conduct a static analysis, the CAD geometry is first subjected to the geometry cleaning, meshing, modelling, and solution processes of the FEA software, afterwards, static load values are applied to the model, and finally, boundary conditions are set [10]. In this analysis, the primary concept of significance revolves around the assumption that temporal factors such as time hold negligible importance and can be disregarded in their impact on the outcomes. In this analysis, the finite element software, SolidWorks effectively converges towards the solution, aligning with the specified boundary conditions and the constructed model. Ultimately, the program provides the user with stress, strain and displacement values, accompanied by visually appealing geometric graphics. Static analysis can be performed using both linear and non-linear methods. In linear static analysis, there are two main assumptions:

- The behavior of the structure is characterized by linearity, meaning it adheres to Hooke's Law.
- The loading is static.

In SOLIDWORKS the FEM used is derived around the Principal of Minimum Energy. Initially, the domains must be divided into many sub domains / subregions which are denoted using the parameter N. Each subdomain is known as an element; It can be stated that the total potential energy in the system is the sum of the potential energy of each of the subdomains as shown below:

$$\pi = \sum_{i=1}^{N} \pi_i \tag{1}$$

Where "π" is the potential energy and "I" is the element number. The energy at each of the subdomains can be calculated using the following equation:

$$\pi = \int_{v_1} \left[\varepsilon^T C \left(\frac{1}{2} \varepsilon - \bar{A} \Delta T \right) - f^T u \right] dV - \int_{S_{\sigma_i}} t^T u dS \tag{2}$$

In the equation above the volume V is related to the volume of the specific element, the term $S_{\sigma i}$ relates to the section of the surface which bounds the element. In order to determine the potential energy in the element, the elastic constant matrix C, the displacement matrix u, the strain matrix ε are used. The displacement matrix can be defined using the displacements and displacement derivatives "q" and interpolation functions "D_i". The combination of these function will define the changes in position of the elements within the system. This can be represented in the equation below:

$$u_i = D_i \times q_i \tag{3}$$

On the other hand, the strain matrix can be created using the displacements and displacement derivatives previously stated and the matrix of strain with respect to the position within the element "B_i". The sum of these components produces the strain matrix as shown below:

$$\varepsilon = B_i \times q_i \tag{4}$$

Using the equations presented above and re-arrangement of the potential energy equation, the equivalent forces applied to each node can be calculated as follows:

$$F_i = \int_{V_i} D_i^T f \, dV + \int_{S_{\sigma_i}} D_i^T t_n \, dS + \int_{V_i} B^T C_i \bar{A}_i \Delta T_i \, dV \tag{5}$$

The stress matrix can be determined when the following manipulations, conditions and parameters are applied:

- The total potential energy equation must be manipulated to include the Stiffness matrix for the entire region "K"; the stiffness matrix for all nodal derivatives, "q" and the assembled nodal load matrix "F".
- The potential energy must now be minimalised when considering the unknown nodal displacements.
- The nodal displacements conditions on the surface of the elements are satisfied.

Once completed the stress at each of the elements can be approximated using the elastic constant matrix "C_i"; the matrix of strain and the matrix of nodal variables "q_i". It is worth noting that all functions stated are with respect to the individual elements and will be applied to all elements in the system. The following equation can be produced:

$$\sigma_i = C_i \times B_i \times q_i \tag{6}$$

However, the equations presented above are only approximations for the true solutions, Increasing the accuracy of the results is a mandatory process in FEA in order to obtain values which closely represent the true solutions. The following Steps can be taken to improve the results produced:

a) The accuracy of the results can be increased by decreasing the size of the elements while increasing the number of elements in the system. This will be the main method used to improve accuracy since the h-adaptive method utilises this process between iterations throughout critical locations.

b) The second method of increasing accuracy is by utilising higher order interpolation methods. This can greatly increase the accuracy of the results at the cost of higher time of investigation. However, this method cannot be used with multi-part assemblies since the meshes are not continuous.

c) The last method is by using the combination of the two methods stated above, this is not feasible for this project since the is more than one component in the simulation meaning only the h-adaptive method can be used.

The deformation computed in SOLIDWORKS is influenced by a number of factors, including the material characteristics. Linear elastic behavior, in which strain is inversely proportionate to applied stress, is the simplest connection between stress and strain. The relationship between these two changes depending on the material and is known as Young's modulus, E. In the situation that a system lacks a linear correlation between the forces exerted and the deformations experienced, it is referred to as a non-linear system. In this study, a non-linear analysis will be conducted. The purpose of this analysis is to evaluate the SOLIDWORKS model characteristics and its ability to withstand loading under specific boundary conditions.

3. Material Selection

The selection of materials is a critical step in the aircraft seat design process. The selection of materials for the system to be designed will have a significant impact on its strength, cost, weight, and other key characteristics. To select the appropriate material, it is imperative to have a comprehensive understanding of the system's requirements that need to be met. The consideration of material characteristics is of utmost significance and serves as the first assumption when representing any material model in Finite Element Analysis (FEA). Incorrect entry of material information might have a significant impact on the outcomes [11]. If erroneous data is provided as input in the FEA process, the resulting output will always be erroneous as well. It is important to consistently exercise caution and attentiveness while inputting material information into the FEA system. The process of defining material in FEA is comparatively less intricate than accurately reflecting real-world materials. Different materials possess a range of material parameters, including yield stress, ultimate stress, Young's modulus, Poisson's ratio, bulk modulus, thermal conductivity, elongation, specific heat, stress-strain curve, and electric properties, among others. In the field of FEA, it is not necessary to explicitly provide all material properties to represent the material. The specific material details that need to be considered depend on the kind of FE analysis being conducted, such as linear or nonlinear solutions, static or dynamic analysis, steady state, or time-dependent analysis.

The necessary qualities of a material that are needed for basic finite element analysis types are shown in Table 1.

When defining the properties of a material, it is essential to specify two specific properties in addition to thermal properties. The key structural analysis parameters are Young's modulus and Poisson ratio. The majority of materials exhibit Poisson ratio values within the range of 0.0 to 0.5. Incompressible substances, such as rubber,

Table 1. Types of finite element analysis

Material Properties	Linear Static	Non-Linear Contact	Non-Linear Material	Non-Linear Dynamic	Fatigue	Linear Dynamic	Thermal	Thermal Structural	Transient structural
Youngs Modulus	Yes	Yes	Yes	Yes	Yes	Yes		Yes	Yes
Poisson Ratio	Yes	Yes	Yes	Yes	Yes	Yes		Yes	Yes
Mass Density	Yes	Yes	Yes	Yes	Yes	Yes		Yes	Yes
Thermal Conductivity							Yes		
Thermal expansion								Yes	
Specific heat									Yes
Stress-Strain curve			Yes						
Fatigue Life curve					Yes				

have a ratio of around 0.5. In this article, the materials AL6061-T6(SS), AL7075-T6(SN), 1023Carbon steel sheet (SS), and KYDEX®T will all be simulated, compared, and used in a certain aspect of either the design of the and/or the assembly of the aircraft seat frame. KYDEX®T, a thermoplastic acrylic-polyvinyl chloride material manufactured by SEKISUI KYDEX, will also be included in the analysis. High-strength aluminium alloys offer lightweight possibilities for aircraft designers due to their low density. Considering this rationale, it is a commonly employed material in the aviation sector. Furthermore, it has been predicted that aluminium satisfies the necessary strength criteria in the context of material investigations.

4. Boundary and Loading Conditions

4.1. Boundary conditions

These refer to the external forces that must be considered to effectively analyse a model or determine the resulting deformations caused by these forces. Boundary conditions are a set of predetermined values that are known and established during the process of constructing a model from scratch [12]. The way the seating design is constrained exerts a substantial influence on the outcomes and necessitates careful consideration. Models that are either over-constrained or under-constrained can result in highly inaccurate stress figures, rendering them essentially useless for the stress engineer. Boundary conditions are essential constraints that must be satisfied to obtain a solution for a boundary value problem. A boundary value problem refers to a mathematical problem involving a system of differential equations that needs to be solved within a specific domain [13]. The known conditions for this problem are provided on the boundary of the domain. In the process of developing a finite element model, it is imperative to commence with the establishment of the mesh model. Subsequently, the contacts are defined, ensuring accuracy and precision. Finally, the appropriate boundary conditions are inserted, guaranteeing the integrity and reliability of the model. To ensure the elimination of rigid-body motion and the accurate representation of physical conditions, the finite element model must be appropriately restrained through the implementation of displacement constraints. In this study, the airplane seat under consideration is *connected to other components using bolts and pins* [14]. It is not advisable to consistently impose constraints upon the nodes situated on the inner surface of the holes where pins or bolts are positioned, as they lack physical constraint. When relocation limits are put around a hole (discontinuity), they often cause an unexpected build-up of stress. This study also incorporates boundary conditions, including both limitations and contacts. In the context of static finite element analysis for an aircraft seat, it is standard to consider the base of the seat as constant i.e., designating it as a fixed support inside the study. The modelling of solid structures often involves the use of a displacement-based model. Boundary conditions often include the imposition of certain displacement values at

Tables 1.a, b, c: Mechanical properties for aircraft seat simulations conducted

Mechanical Properties	Value
Tensile Strength	570MPa
Yield Strength	505MPa
Modulus of Elasticity	72000MPa
Poisons Ratio	0.33

1a). Mechanical Properties of AL6061-T6(SS), 1b) Mechanical Properties of AL7075-T6(SN)

Mechanical Properties	Value
Tensile Strength	310MPa
Yield Strength	275MPa
Modulus of Elasticity	69000MPa
Poisons Ratio	0.33

1c). Mechanical Properties of KYDEX®T

Mechanical Properties	Metric
Tensile Strength	42MPa
Yield Strength	40MPa
Modulus of Elasticity	2600MPa
Poisons Ratio	0.433

designated locations on the structure. The airplane seat is comprised of several components, necessitating the need to establish connections between them. In this article, SolidWorks is used as the pre-and post-processing tool for generating the mesh of the model, computing the stress distributions, and visualizing the outcomes of the finite element analysis.

4.2. Loading Conditions

In the context of an analysis model, the loads refer to the mechanical forces and thermal loading that exert their influence upon the object or component. The primary loading conditions used in FEA are force, pressure, and temperature. These may be applied to many geometric components such as points, surfaces, edges, nodes, and elements, or can be applied remotely from a specific feature [15]. The application of loads and constraints is specified after the selection of the analysis type, setting of fundamental parameters such as materials, and completion of the meshing process for the component. To comprehensively understand probable failure modes, it is essential to establish them based on the maximum predicted loads that the product may encounter during its lifespan, as opposed to the regular loads. To obtain precise and reliable outcomes, it is imperative to verify that the loads being imposed are strategically distributed across the appropriate surfaces or specific sections. The proper application of loads is a critical component of this simulation. The surface or section of a surface on which a force is applied must be carefully considered as it can significantly impact the results. In this analysis, due to the lack of knowledge regarding deformations, the parameters that are entered are limited to the average weight values of passengers occupying an aircraft seat. The loads under consideration are classified as distributed loads within the model. In the context of stress engineering, it is imperative to assume that the weight of a passenger is uniformly distributed on the seat. In the present scenario, the weight of a passenger is considered to be 1000N. However, a total weight of 1500N will be entered to make up for some missing parts, such as the seat cushion, backrest, and seat belt.

5. Topology Optimization

Topology optimization (TO) is a computational technique used for optimizing the arrangement of materials within a specified area, based on a set of predefined loads, conditions, and constraints. It employs algorithmic models to achieve the desired shape optimization. The use of this method enables the attainment of the most optimal geometric structure for the intended model, considering the prescribed boundary conditions and the designated objective function. The use of topology optimization enables the created models to achieve material reductions and maintain a minimal weight [16]. The first phase of its operation necessitates the involvement of an engineer who is responsible for generating a CAD model. During this step, the engineer carefully incorporates various loads and limits while considering the specific specifications of the project. Subsequently, the program eliminates unnecessary parts and produces a single optimized mesh-model idea that is ready for analysis by an engineer. Topology optimization relies on a pre-existing model that is built to operate effectively. Topology optimization is an initial step in the design process that involves identifying the minimum required design space for the subsequent optimization of the structure. Subsequently, the topology optimization software (SolidWorks) virtually generates pressure on the design from various angles, conducts structural integrity analysis, and identifies unnecessary material. It is an excellent tool for aircraft seat design.

6. Solidworks Finite Element Simulation-Walkthrough

6.1. Geometry Design

The process of assembling the airplane seat frame using SolidWorks entails the systematic integration of the many individual components to construct a seating framework that is both operational and secure. The procedure begins by generating an entirely new assembly in SolidWorks, whereby each constituent, such as the seat base, connecting rod, and leg spreaders, is intricately designed. By using the mating features offered by SolidWorks, the components are then joined, therefore guaranteeing precise alignment and optimal operational performance. The process of material selection and structural analysis is undertaken, followed by the generation of precise drawings for the manufacturing process. The separate and assembled components of the aircraft seat are shown in Figure 2 and 3.

6.2. Boundary Conditions

For the boundary conditions, we assume the base of the spreaders is constant, this means we define it as a fixed support in the analysis. The fixed-geometry fixture was selected and applied in the z-direction as shown in Fig. 4.

6.3. Loading Conditions

Since the deformations are unknown in this study, the average passenger weight for an aircraft seat is used as inputs

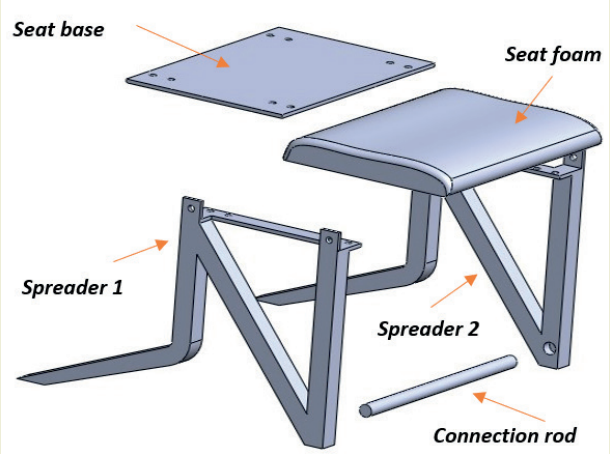

Figure 2. Exploded view of assembled seat frame

instead of random load values. The model considers these loads as the distributed load. This indicates that we assume a constant distribution of a passenger's weight across the seat. The analytical findings are accurate under this assumption. In this case, we will assume that the passenger weighs 1500N. Also, the seat foam was suppressed as it has a minimal effect on the total weight and will remain suppressed for the rest of the simulations (Fig. 5).

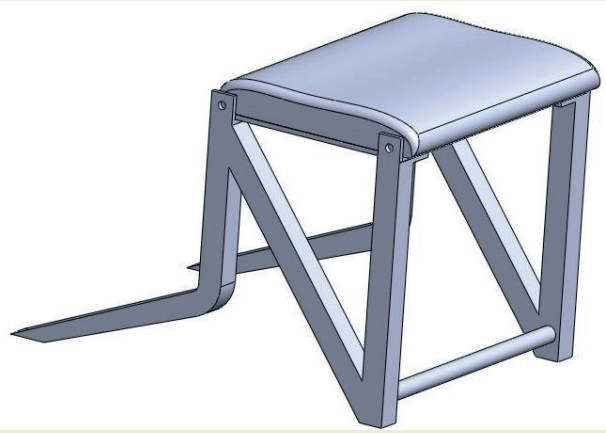

Figure 3. 3D Design of assembled seat frame.

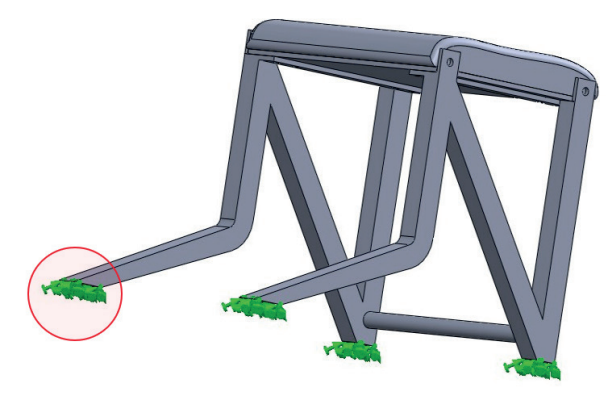

Figure 4. Application of boundary conditions

6.4. Mesh Design and Independence Study

6.4-1 Initial coarse mesh

For the initial simulation, an automatic mesh s designed initially to be coarse (Fig. 6) as shown below. The mesh dimension size is 37.44mm, however, the mesh is not at its finest, Therefore, the mesh size will be subsequently reduced until it accommodates the desired mesh independence criteria.

6.4-2 Jacobian Ratio

Jacobian ratio in SolidWorks often refers to a metric used to determine the mesh element quality inside a finite element analysis (FEA) simulation. The Jacobian ratio is used to evaluate the distortion or deformation of finite elements, such as tetrahedral or hexahedral elements, inside the finite element analysis (FEA) mesh. Obtaining precise simulation results necessitates the use of a high-quality mesh. In simple terms, the Jacobian ratio

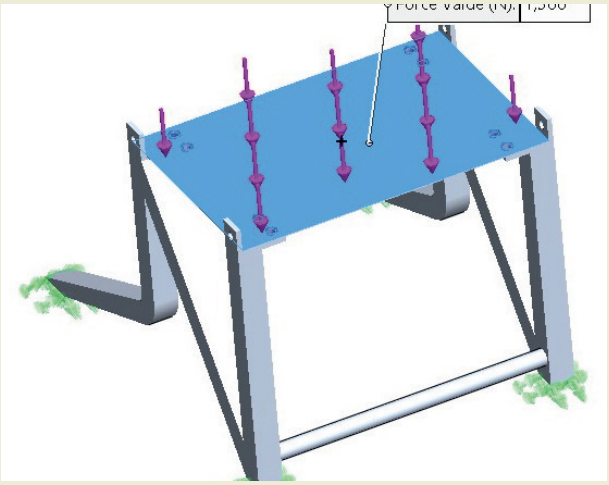

Figure 5. Application of Loading Conditions.

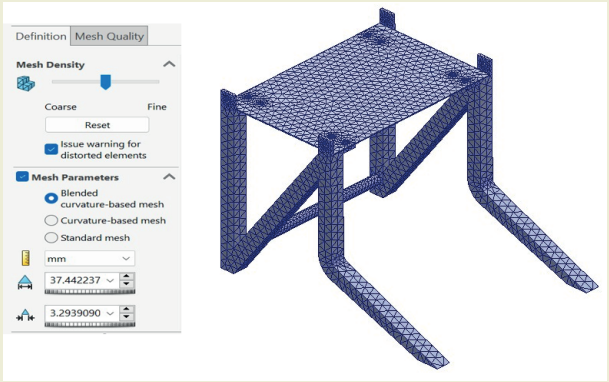

Figure 6. Simple initial mesh

measures the extent to which the form of an element deviates from an ideal shape. It is depicted in Fig. 7 for the current aircraft seat model.

6.4-3 Aspect Ratio

Aspect ratio is the measure of a geometry width to its height. It can also be used to describe any other form of visuals. It is critical to sustain a desirable and ergonomic aspect ratio so that the designs and models are accurate and fit together well. Fig 8 visualizes the different aspect ratios in the seat FEA model.

6.4-4 Connection modelling

A pin connection is selected to connect the seat base to the spreaders as shown in Fig. 9 below.

6.4-5 Mesh Independence Study

For the mesh Independence study, a graph between the mesh size and the maximum stress is plotted to determine the most appropriate mesh for the structure - three different meshes are studied- coarse, intermediate density and fine. However, before the maximum stress can be calculated, the material of the structure must be selected, therefore, for the mesh convergence graph, AL7075-T6(SN) is selected for all the parts of the structure. Fig. 10 shows the 3 different mesh designs used. In all cases

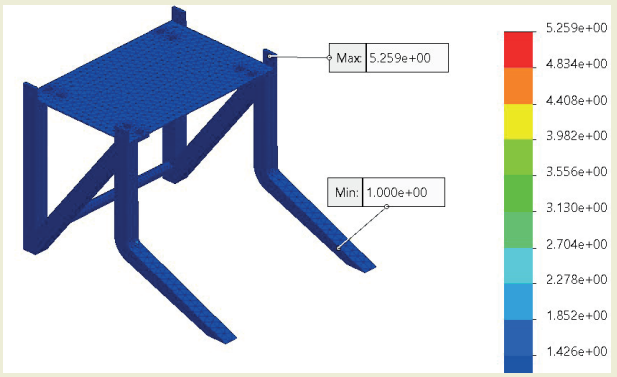

Figure 7. SOLIDWORKS Jacobian Ratio Plot.

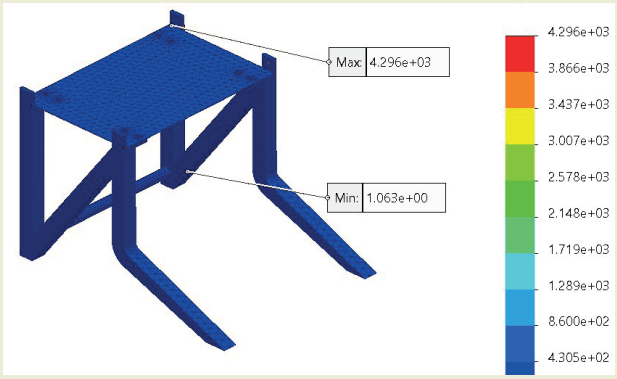

Figure 8. Aspect ratio plot.

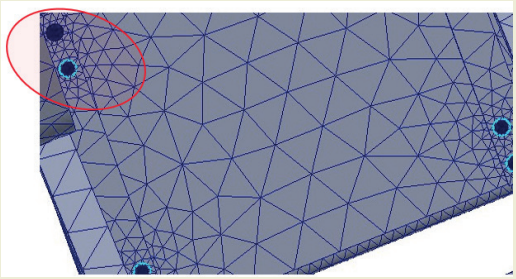

Figure 9. Connection pins prescribed in SOLIDWORKS.

tetrahedral 3-D elements are deployed. Fig. 11 shows the mesh independence plot. Table 2 shows the peak Von Mises stress computed for each of the three meshes designed.

Figures 10, 11 and Table 2 present the computational results for independence of mesh size and maximum stress in pounds per square inch (Psi). The research includes the use of 20, 15 and 10mm mesh sizes. It is evident that the maximum stress in the system is affected by the mesh size. The maximum stress rises gradually when the mesh size is reduced from 20mm to 10mm. This trend indicates that the smaller 10mm grid collects more information about the stress distribution in the system, leading to a more accurate stress calculation due to more interpolation points available in the fine mesh design.

7. Results

3 sets of SOLIDWORKS finite element simulations have been performed for the three different materials documented in Table 1- a) AL6061-T6(SS), b) AL7075-T6(SN) and c) KYDEX®T. All these materials are commonly employed in seat design in the aircraft industry. Additionally, a 4th simulation has been conducted combining these different materials for the different seat structural components.

7.1. Simulation 1 -AL6061-T6(SS)

7.1-1 Stress Analysis - Von-Mises Stress

A total force of 1500N is placed on the seat base as shown in the section, the materials are selected as shown in Table 1, a mesh size of 10mm is selected according to the mesh independence study and the study is run to calculate the maximum and minimum stress as shown in the figures below. Table 3 shows the specifications for the 2 spreaders, seat base and connection rod. The seat foam

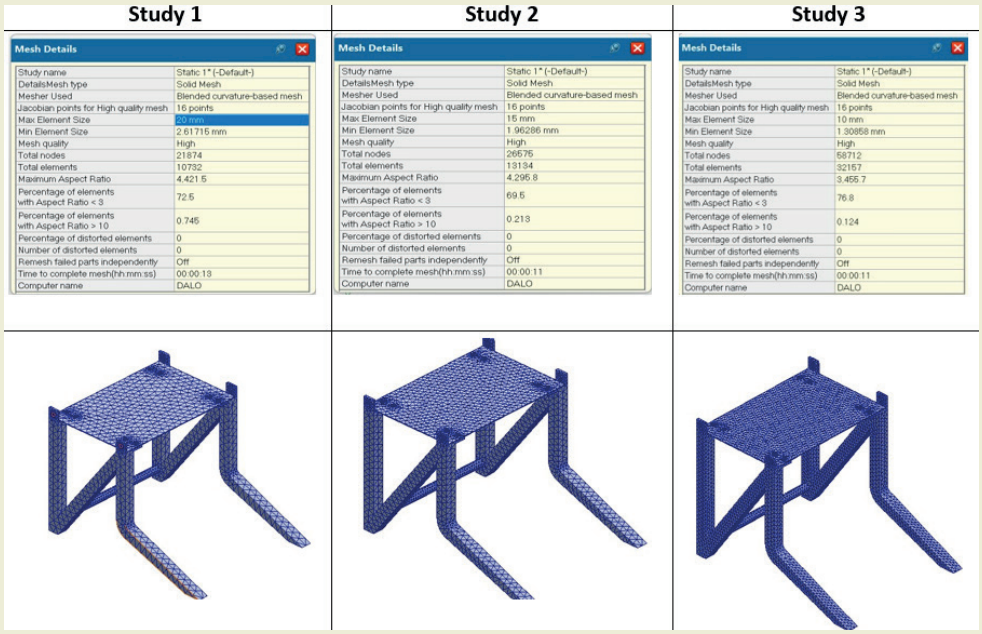

Figure 10. 3 mesh designs developed for the aircraft seat structure.

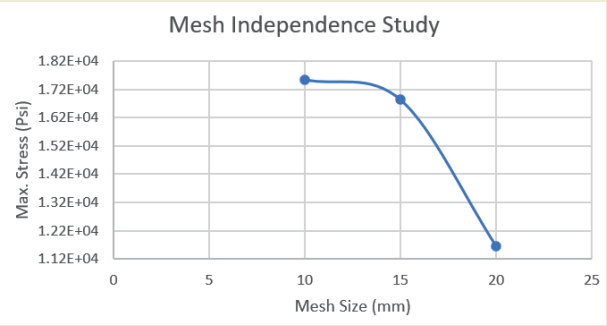

Figure 11. Mesh independence plot

Table 2. Peak stresses computed for 3 mesh design cases with AL7075-T6(SN) design material.

Mesh Study No.	Mesh Size (mm)	Max. Stress (Psi)
1	20	1.164e+04
2	15	1.683e+04
3	10	1.755e+04

is not simulated as it does not contribute to structural integrity and is related to comfort for passengers, not resilience of the seat design.

Table 3. Seat model component materials used in simulation 1.

Component	Material
Spreaders	AL6061-T6(SS)
Seat Base	AL6061-T6(SS)
Connection Rod	AL6061-T6(SS)

The static nodal stress plot is given in Fig. 13.

7.1-2 Displacement Analysis (Y-Component of Displacement)

We focus on the Y-component of the displacement since it is the determining factor in the material's failure. Fig. 14 visualizes the displacement contour plot.

Fig. 15 shows the associated static displacement plot.

The displacement criteria must be satisfied for the maximum Y-Component displacement value to be smaller than 0.01 of the width of the Seat base. The following calculations are performed to check this:

$$\text{i.e., } max.\ y\text{–}component\ of\ displacement < \frac{1}{100}\ of\ (width\ of\ \text{seat base})$$

$$width\ of\ \text{seat base},\ W = 383mm$$

$$max.\ y\text{–}component\ of\ displacement\ \text{of}\ seat\ base = 0.0606mm$$

$$\frac{1}{100} * 383 = 3 \cdot 83\,mm$$

$$0.0606 < 3.38\,. \qquad (7)$$

Therefore, the displacement criteria are met.

7.1-3 Factor of safety (Reserve Factor)

The factor of safety is a safety metric used in structural analysis inside the SolidWorks software. Structural efficiency is defined as the ratio between the maximum load that a structure can sustain and the load that is applied to it. The reserve factor may be determined by dividing the ultimate strength of a material by the applied load. The ultimate load refers to the maximum load capacity of a structure before its failure. The applied load refers to the

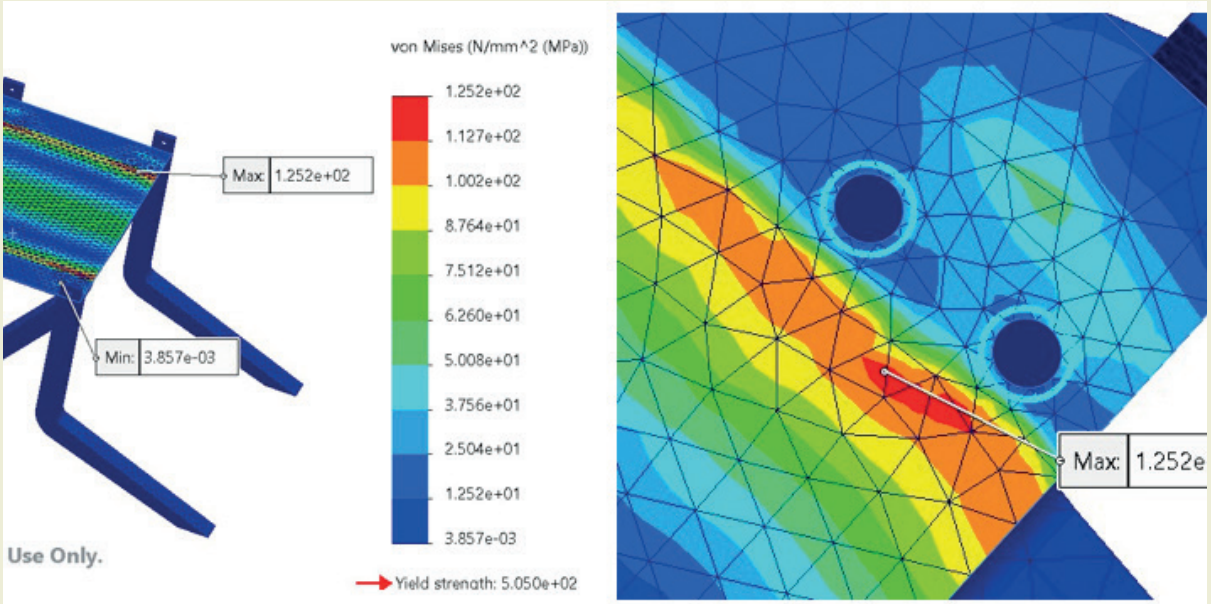

Figure 12. Stress analysis (simulation 1): left- full 3-D contour plots, right - zoom in to connection points.

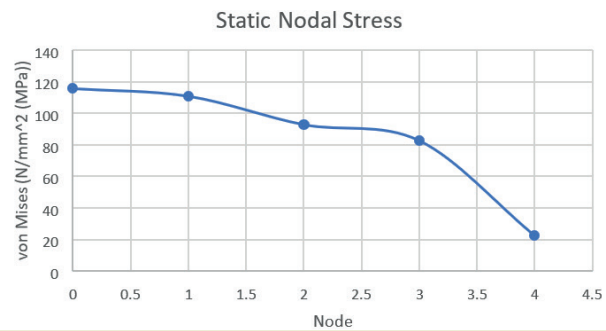

Figure 13. Static nodal stress (simulation 1

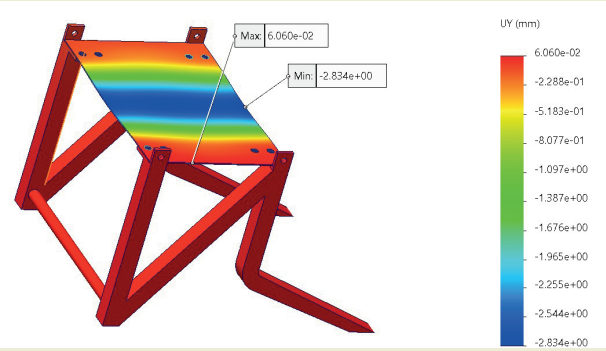

Figure 14. Y-Component of displacement (simulation 1).

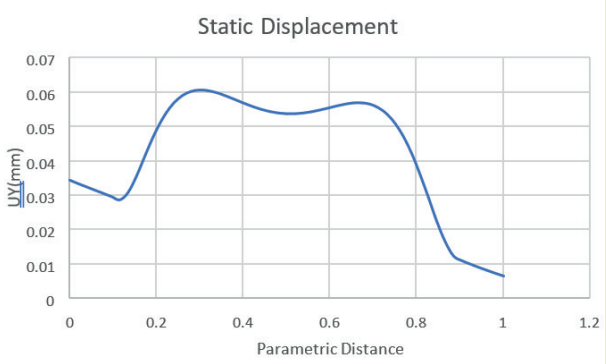

Figure 15. Static displacement plot (simulation 1).

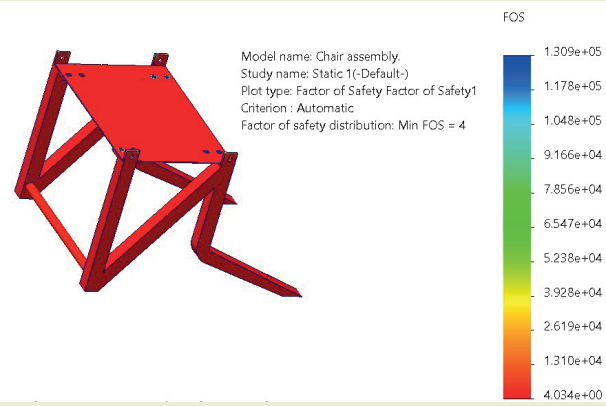

Figure 16. Failure Criteria (factor of safety) computed In SOLIDWORKS for simulation 1

external force or weight that is exerted on the structure during the process of analysis. A Reserve Factor of 1.0 signifies that the structure has the *minimum capacity required to sustain the imposed load*, without any additional safety buffer. A Reserve Factor beyond 1.0 signifies that the structure has a certain degree of safety buffer, while a Reserve Factor below 1.0 suggests that the structure is prone to failure when subjected to the applied load. Fig. 16 shows the contour plot for factor of safety analysis in simulation 1.

Fig. 17 shows the factor of safety distribution plot for simulation 1.

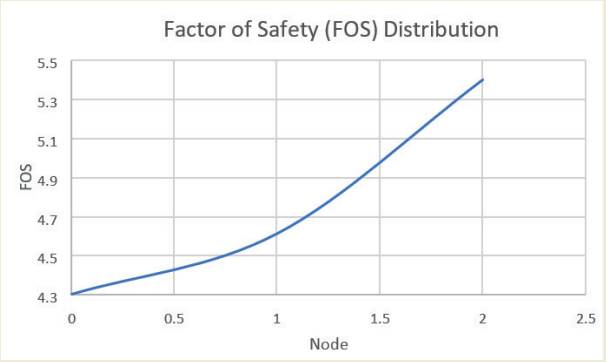

Figure 17. Factor of safety plot for simulation 1.

Table 4 summarizes the results extracted from the finite element analysis for Simulation 1 (AL7075-T6(SN)).

Table 4. Summary of simulation 1 - outputs with associated cost estimation

Properties	Values
Max. Stress	1.252e+02 N/mm^2
Min. Stress	3.857e-03 N/mm^2
Max Y-component of displacement	0.0606 mm
Factor of Safety	4.034
Total Mass	2.32kg
Price	$2.304/kg

7.2. Simulation 2 - AL6061-T6(SS)

Table 5 shows the specifications for the 2 spreaders, seat base and connection rod for simulation 2. Again, the seat foam is not simulated.

7.2-1 Stress Analysis - Von-Mises Stress

The same procedure is executed as for simulation 1.

The static nodal stress plot is given in Fig. 19.

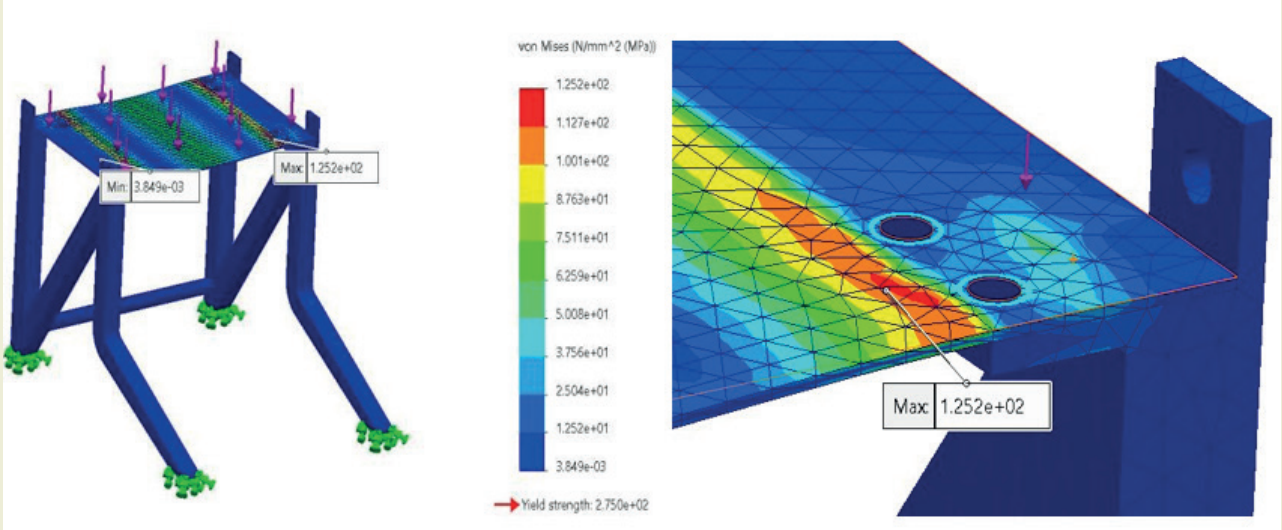

Figure 18. Stress analysis (simulation 2): left- full 3-D contour plots, right - zoom in to connection points.

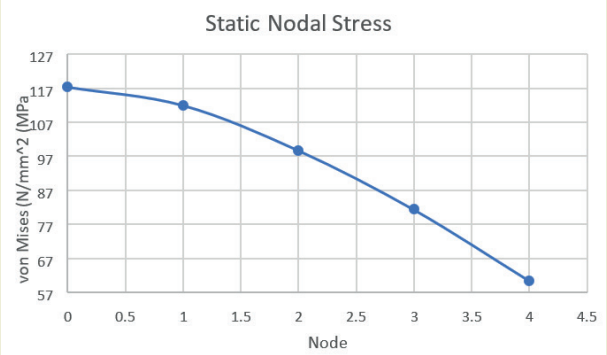

Figure 19. Factor of safety plot for simulation 2.

7.2-2 Displacement Analysis (Y-Component of Displacement).

As for simulation 2, we utilize the Y-component of the displacement as it is the controlling factor for failure of the material (AL6061-T6(SS). Fig. 20 displays the displacement contour plot. Fig. 21 depicts the associated static displacement plot. The displacement criteria as elaborated earlier has to be satisfied for the maximum Y-Component displacement value to be smaller than 0.01 of the width of the aircraft seat base. For simulation 2, we therefore repeat the calculations to verify this, with the appropriate material data:

$$max.\ y{-}component\ of\ displacement < \frac{1}{100}\ of$$

Table 5. Seat model component materials used in simulation 2.

Component	Material
Spreaders	AL6061-T6(SS)
Seat Base	AL6061-T6(SS)
Connection Rod	AL6061-T6(SS)

$$(width\ of\ \text{seat base})$$

$$width\ of\ \text{seat base},\ W = 383mm$$

$$max.\ y{-}component\ of\ displacement\ \text{of}\ seat\ base = 0.0662mm$$

$$\frac{1}{100} * 383 = 3 \cdot 83\,mm$$

$$0.0662 < 3.38 \qquad (8)$$

Therefore, the displacement criteria are also satisfied for simulation 2.

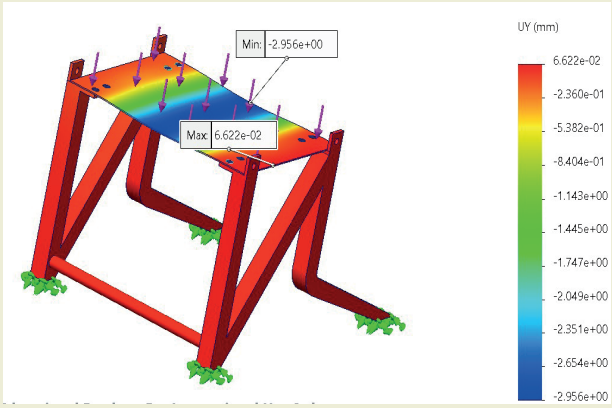

Figure 20. Y-Component of displacement- simulation 2.

7.2-3 Factor of safety (Reserve Factor)

Fig. 22 shows the contour plot for factor of safety analysis in simulation 2. Fig. 23 illustrates the factor of safety distribution plot for simulation 2. Table 6 summarizes the results extracted from the finite element analysis for Simulation 2 i. e. AL6061-T6(SS).

7.3. Simulation 3 - KYDEX®T

Table 7 shows the specifications for the 2 spreaders, seat base and connection rod. The seat foam as before is not analysed.

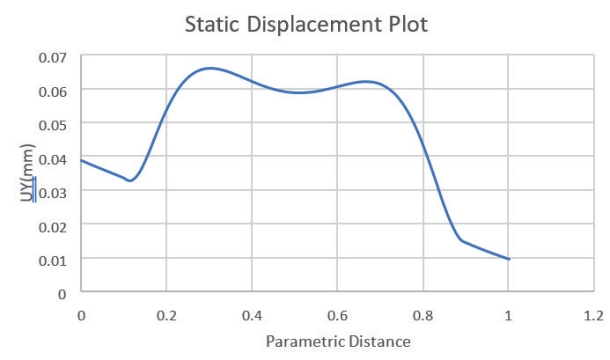

Figure 21. Static displacement plot (simulation 2)

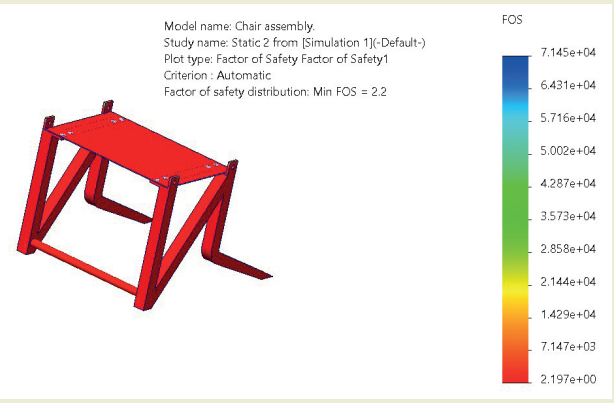

Figure 22. Failure Criteria (factor of safety) computed In SOLIDWORKS for simulation 2

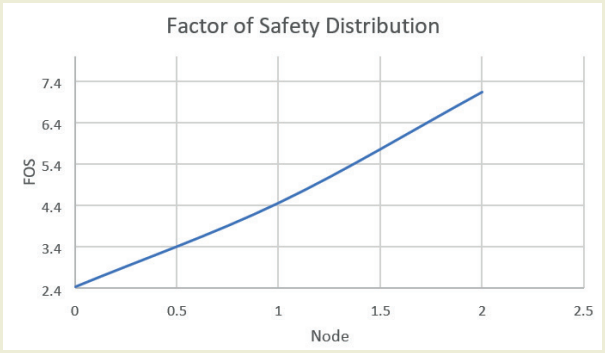

Figure 23. Factor of safety plot for simulation 2.

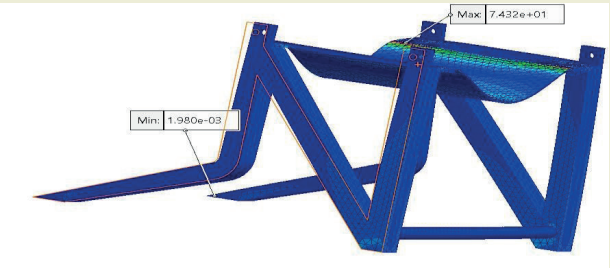

Figure 24. *Total deformation contour plots (simulation 3)*

Table 6. Summary of simulation 2 - outputs with associated cost estimation

Properties	Values
Max. Stress	1.252e+02 N/mm^2
Min. Stress	3.857e-03 N/mm^2
Max. Y-component of displacement	0.0662 mm
Factor of Safety	2.197
Total Mass	2.32kg
Price	$2.228/kg

Table 7. Seat model component materials used in simulation 1.

Component	Material
Spreaders	KYDEX®T
Seat Base	KYDEX®T
Connection Rod	KYDEX®T

Table 8. Summary of stress analysis, displacement and other results (simulation 3)

Properties	Values
Max. Stress	$7.432e+01\ N/mm^2$
Min. Stress	$1.980e-03\ N/mm^2$
Max. Y-component of displacement	$10.04mm$
Factor of Safety	0.57
Total Mass	$1.6kg$
Price	$51/kg

For brevity, in this 3rd simulation we do not give the entire finite element results as in simulations 1 and 2; instead, we have summarized the total deformation in Fig. 24 and the key results again are documented in Table 8.

7.4. Simulation 4 – combined material design

7.4-1 Stress Analysis - Von-Mises Stress

Table 9 shows the specifications for the 2 spreaders, seat base and connection rod. The seat foam once again is omitted in the finite element simulation. Fig. 25 visualizes the 3-D Von Mises stress distribution.

Table 9. Seat model component materials used in simulation 4.

Component	Material
Spreaders	AL7075-T6(SN)
Seat Base	KYDEX®T
Connection Rod	AL6061-T6(SS)

The static nodal stress plot is given in Fig. 26.

7.4-2 Displacement Analysis (Y-Component of Displacement)

As for the other simulations, we utilize the Y-component of the displacement as it is the controlling factor for fail-

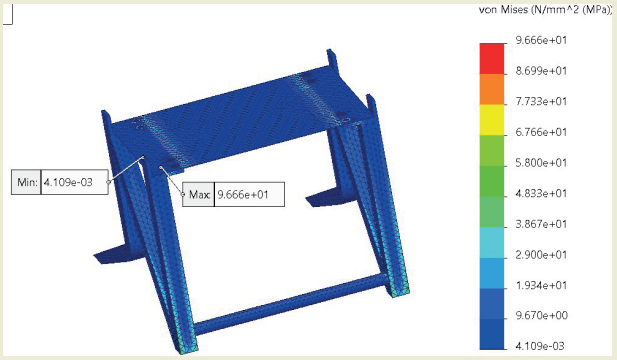

Figure 25. 3-D Von Mises stress contour plot (simulation 4).

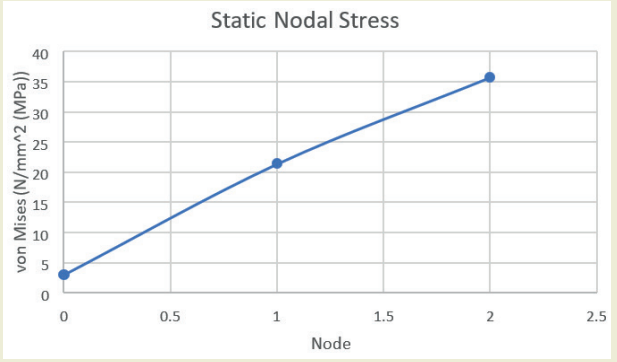

Figure 26. Static nodal stress (simulation 4)

ure of all the materials deployed in this final case. Fig. 27 shows the displacement contour plot. Fig. 28 depicts the associated static displacement plot. The displacement criteria, as elaborated earlier had to be satisfied, for the maximum Y-Component displacement value to be smaller than 0.01 of the width of the aircraft seat base. For simulation 4, again the same calculations are executed to verify this, with the appropriate material data:

In this case, the following calculations are used:

$$max.\ y\text{–}component\ of\ displacement < \frac{1}{100}\ of\ (width\ of\ \text{seat base})$$

$$width\ of\ \text{seat base},\ W = 383mm$$

$$max.\ y\text{–}component\ of\ displacement\ \text{of}\ seat\ base = 1.301mm$$

$$\frac{1}{100} * 383 = 3 \cdot 83\,mm$$

$$1.301 < 3.38 \qquad (9)$$

Evidently this confirms that the displacement criteria are also satisfied for simulation 4.

7.4-3 Factor of safety (Reserve Factor)

Fig. 29 depicts the contour plot for factor of safety analysis in simulation 4. Table 10 summarizes the results extracted from the finite element analysis for Simulation 4 i. e. with all three materials utilized for different seat components.

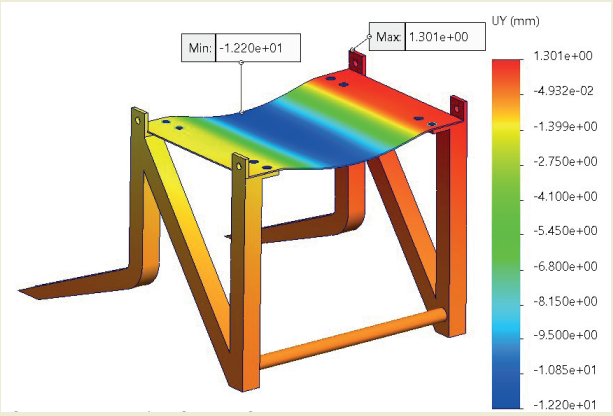

Figure 27. Y-Component of Displacement (simulation 4).

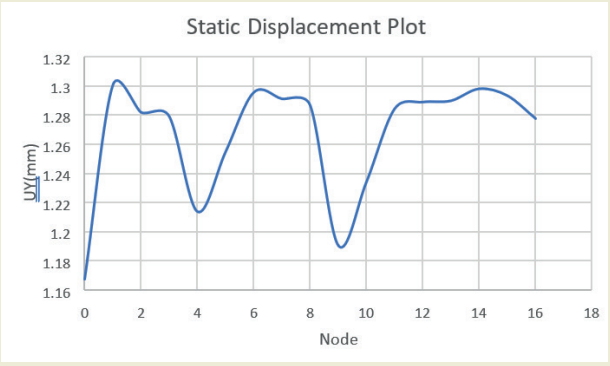

Figure 28. Static displacement plot (simulation 4)

Figure 29. Failure Criteria (factor of safety) computed In SOLIDWORKS for simulation 4.

Finally in Table 11, we present a comparison of the main results for all 4 simulations conducted in SOLIDWORKS.

To provide the most suitable material recommendations for a certain application, it is essential to consider many elements such as safety, displacement, and overall mass for each simulation. The objective is to identify a material that offers a favourable equilibrium between safety (higher safety factor), minimum displacement (lower Y-Comp of Displacement) and an appropriate overall mass.

Table 10. Summary of stress analysis, displacement and other results (simulation 4)

Properties	Values
Max. Stress	9.666e+01 N/mm^2
Min. Stress	4.109e-03 N/mm^2
Max. Y-component of displacement	1.301 mm
Factor of Safety	1.1
Total Mass	2.3kg

Table 11. Summary of all 4 SOLIDWORKS simulations

SIMULATIONS	FACTOR OF SAFETY	Y-COMP OF DISPLACEMENT	TOTAL MASS
SIMULATION 1	4	0.0606 mm	2.32kg
SIMULATION 2	2.2	0.0662 mm	2.32kg
SIMULATION 3	0.57	10.04mm	1.6kg
SIMULATION 4	1.1	1.301 mm	2.3kg

a) Factor of safety: Typically, larger values are favoured due to their association with a greater margin of safety. Simulation 1 exhibits the greatest factor of safety, with a value of 4. It is followed by Simulation 2, which has a factor of safety of 2.2. Following this, Simulation 4 demonstrates a factor of safety of 1.1, while Simulation 3 exhibits the lowest factor of safety, with a value of 0.57.

b) Y-Comp of Displacement: Smaller numbers are preferable as they indicate a lower degree of deformation or displacement. Simulation 1 exhibits the lowest displacement value of 0.0606 mm, while Simulation 2 follows with a displacement of 0.0662 mm. Simulation 4 displays a displacement of 1.301 mm, while Simulation 3 has the highest displacement value of 10.04 mm.

c) Total Mass: Lower total mass is preferable since it helps keep the structure light and cheap. Here, Simulation 3 weighs in as the lightest at 1.6 kg, followed by Simulations 1 and 2 at 2.32 kg each, and finally, Simulation 4 at 2.3 kg.

Considering all these criteria, Simulation 1 emerges as the most prominent option due to its superior factor of safety, minimized displacement and comparable overall mass in comparison to Simulation 2. Hence, if the key considerations revolve around safety and minimum displacement, it can be concluded that Simulation 1 would be the most suitable option. Therefore, AL7075-T6(SN) is the best material selection and is considered for the subsequent topology optimization analysis.

8. Topology Optimization

In Simulation 1, the choice of AL7075-T6(SN) as the optimal design material inspires the objective to optimize the design to improve its structural durability, minimize deformation and also optimize the total mass while upholding safety standards. The primary aim is to achieve the best capabilities of the selected material via the optimization of its topology. This entails ensuring that the material is employed in the most efficient way possible, surpassing safety standards while simultaneously minimizing deformation and weight.

8.1. Loading Simulation for single component

To begin the process of topology optimization, the first step involves simulating the application of a 750N remote load on the airplane seat spreader i. e. a single component of the seat. SolidWorks software provides the capability to accurately specify the load conditions, including both the orientation and amplitude of the applied force. In this scenario, the load is executed with the purpose of replicating real-world circumstances, hence guaranteeing the spreader ability to endure the stresses that it would encounter.

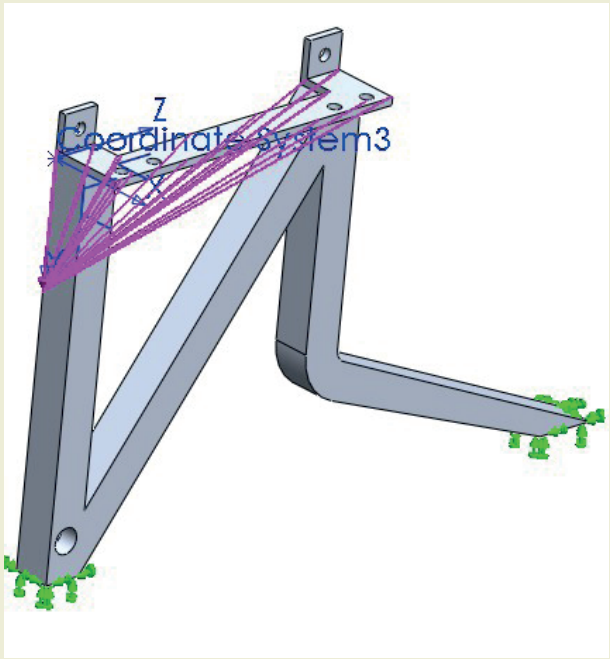

Figure 30. Remote load application.

8.2. Meshing

The same meshing procedure is repeated during the topology optimization process to refine the structure.

8.3. Topology Optimization Analysis:

After the load and material characteristics have been determined, SolidWorks proceeds with conducting a topology optimization study. The computational approach used in this study involves the iterative evaluation of various material distribution scenarios within the design space of the spreader. The objective is to selectively eliminate material from areas with lower stress concentrations while simultaneously strengthening sections that are exposed to greater stress levels. The result of this research is a structural design that effectively reduces weight while also ensuring the necessary structural integrity to endure the applied load. The final design will

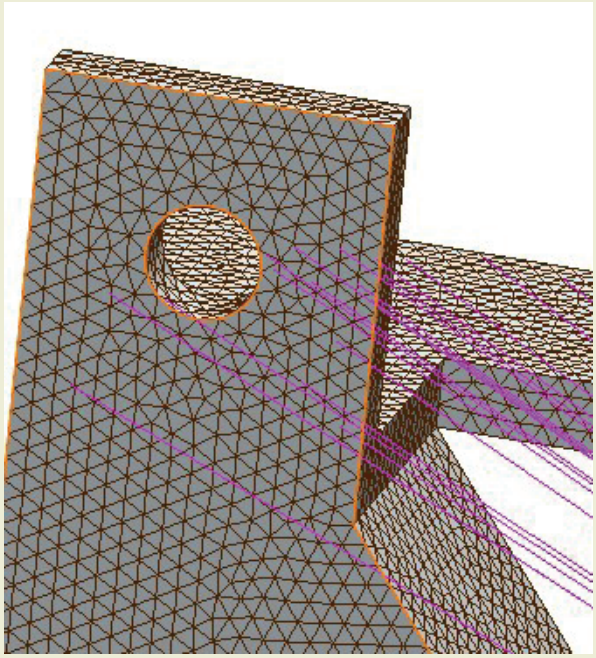

Figure 31. Meshed structure.

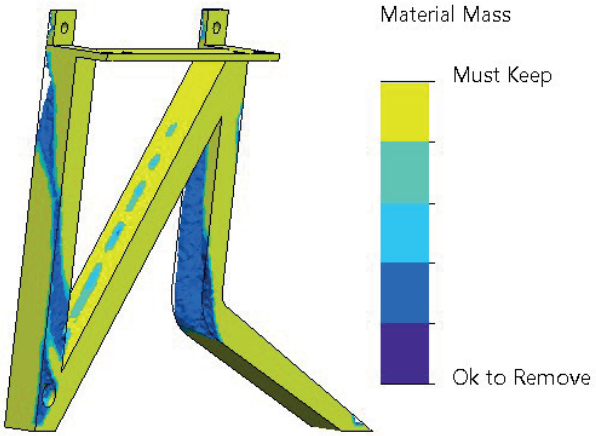

Figure 32. Topology visualization.

demonstrate a refined distribution of material, prioritizing regions that are essential for supporting loads. The results are summarized in Table 12.

Table 12. Topology optimization simulations

Study Name	Topology optimization
No. of Nodes	23049
Number of Elements	108606
Total Simulation Time	00:06:49
Mass Reduction	30%

8.4. Visualization and Results

The improved design can be seen using SolidWorks' visualization capabilities (Figure 32). Stress distribution patterns, regions where material has been removed, and weak spots can all be analysed. The design may be thoroughly tested and improved to ensure it is secure and functional.

Table 13. Topology optimization-key results for simulation 1 material choice (AL7075-T6(SN))

Properties	Values
Max. Stress	1.894e+02 N/mm^2
Min. Stress	6.357e-04 N/mm^2
Max Y-component of displacement	0.0543 mm
Factor of Safety	2.666
Total Mass	1.89kg
Price	$2.304/kg

The results after topology optimization of Simulation 1 (AL7075-T6(SN)) are given in Table 13 below.

8.5. Improved Design

The optimized design is shown for simulation 1 above in Figure 33.

8.6. Comparison

Table 14 summarizes the comparison for the original simulation 1 and new topologically optimized computations. In Simulation 1 of AL7075-T6(SN), structural analysis showed remarkable findings. The material had a maximum stress of 125.2 N/mm2 and a minimum stress of 0.0039 N/mm2. Due to its strong 4.034 factor of safety, the component may have been over-engineered for its intended use. However, at 2.32 kg, the component's mass and $2.304/kg material cost showed a high design cost. The maximum Y-component of displacement was 0.0606 mm, which was acceptable but could have been optimized to decrease material use and expense without affecting structural integrity. After performing topology optimization on Simulation 1 of AL7075-T6(SN), several

Figure 33. Improved design via topological optimization for simulation 1.

improvements have been achieved. The maximum stress sustained by the component has been elevated to 189.4 N/mm2. However, it is worth noting that the minimum stress has also risen, although to a negligible value of 0.0006 N/mm2. The compromise in this scenario is characterized by a fall in the factor of safety to 2.666, suggesting a design that is more optimal but possibly associated with more risk. The most notable improvements, however, concern weight reduction. The overall mass of the component saw a substantial reduction, reaching 1.89 kg, which represents a notable improvement on the original design. This suggests that there may be significant cost reductions in terms of material prices, as well as lower inertial loads and improved handling.

Table 14. Comparison of original simulation 1 and topology optimization results for simulation 1 - material choice (AL7075-T6(SN))

Properties	Initial Design	Optimized Design
Max. Stress	1.252e+02 N/mm^2	1.894e+02 N/mm^2
Min. Stress	3.857e-03 N/mm^2	6.357e-04 N/mm^2
Max Y-component of displacement	0.0606 mm	0.0543 mm
Factor of Safety	4.034	2.666
Total Mass	2.32kg	1.89kg

8.7. Fully Assembled Optimized Design

Following the single component (spreader) topological optimization, a second fully assembled structural seat case has also been optimized, again for simulation 1. This is visualized in Figure 34 and elaborated upon in the next section.

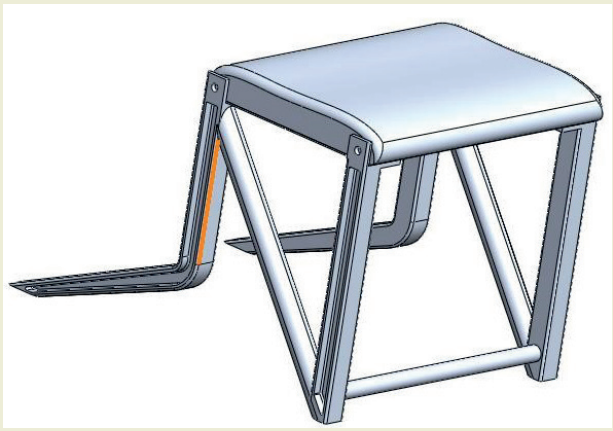

Figure 34. Fully Assembled Optimized Seat Frame (for simulation 1-AL7075-T6(SN).

9. Discussion

This article has examined the static stress analysis of an aircraft seat. The work focuses primarily on 3-D modelling, static stress analysis and topology optimization studies and their outcomes. In this research, Acro Aircraft Seating Company provided the aircraft seat model to be analysed. In the next stage of the study, model preparation studies for the seat's static analysis have been initiated. Prior to analysing the seat components with the FEA technique, a mesh analysis was conducted. This is one of the most crucial steps of model preparation by far. Since the mesh quality and mesh size are crucial for the created model to achieve convergence to the correct results, they must be carefully considered. After setting the proper mesh parameters for the analyses, the boundary conditions and determined loads for the seat were established. Next, the intended materials for the designed seat were inputted into the SOLIDWORKS program, and materials were designated to the seat parts. Thereafter, the model is defined with the required solution methodologies. The model was then run, and the results are visualized.

9.1. Static Analysis

The results derived from the static analysis demonstrate that the stress and strain values obtained from the calculations were found to be within the anticipated range for static analysis. Upon evaluation of the obtained findings, it becomes apparent that the maximum anticipated stress level reaches around 189 MPa. Upon examination of the yield strength and tensile strength properties of the material used, it was noted that the stress values exhibited a substantial difference when compared to the strength values. Based on the findings obtained from the analysis, it can be concluded that the aircraft seat design successfully satisfying the requirements of static analysis criteria.

9.2. Topology Optimization

Topology optimization plays a crucial role in the context of airplane seats because of the significant cost implications associated with the weight of flight-related parts within the aviation sector. Within this context, each instance of weight reduction work that is carried out, while still adhering to the necessary strength limitations of the seat, results in a financial benefit. To achieve this objective, research on topology optimization has been undertaken for the rear seat leg (spreader), a critical component influencing the overall weight of the seat. The topology optimization procedure was iteratively performed using three objective functions. The findings from the topology optimization investigations have shown that the structural integrity of the CAD model under consideration can be maintained even after the removal of 30% of the original material. This suggests that the FE approach proposed in this study may be successfully used for aircraft seat design. Based on the findings, it can be said that the use of topology optimization in the research yields a weight and material reduction of 30% for the seat leg. The use of computer-aided engineering design tools in this investigation has underscored the significance of their efficient application in the design of crucial engineering structures. These tools not only contribute to weight reduction but also provide a decrease in product development duration. Furthermore, they offer valuable insights into seat design.

10. Conclusions

In this article, SOLIDWORKS finite element stress analyses were performed to examine the structural integrity of an aircraft seat. The results of these analyses were visualized carefully. The comparison between the finite element (FE) analysis findings of various aerospace mate-

rials demonstrates a satisfactory analysis, hence enhancing the level of trust in the accuracy and reliability of the finite element method (FEM). Nevertheless, it is worth noting that some analysis phases may benefit from a more complete approach, and there is potential for doing future research to further enhance the depth of analysis. For the current study, the loads identified as the boundary condition in the topology optimization were deemed acceptable. This acceptability was achieved by the incorporation of supplementary loads in conjunction with the loads derived through statistical analysis. In the preceding phase, prior to conducting topology optimization, the inclusion of dynamic analysis with static analysis would enable the determination of *more precise boundary conditions* for the purpose of topology optimization. Topology optimization has also yielded approximate outcomes; however, as previously indicated, further efforts may be undertaken to generate even higher precision. Another concern is the potential development of a novel design after the completion of topology optimization. In the present context, after the completion of the topology optimization analysis, the acquired results may be transferred to computer-aided design (CAD) software to generate a novel CAD model. This implies that it is possible to do an engineering-design iteration. It is important to note that the results derived from the present finite element analysis would of course in industrial manufacturing require validation by physical experimentation. It is acknowledged that, despite the reliability and accuracy of the present findings it is necessary to subject the proposed aircraft seat design to physical testing to ascertain the validity of the SOLIDWORKS finite element modelling, prior to implementation of the seat design as a finalized product. Additionally, since in the present simulations, the foam seat was ignored (due to negligible contribution to structural integrity), however, in future studies it may be incorporated using a suitable hyper-elastic material model in SOLIDWORKS or indeed other FEA codes e. g. ANSYS. Dynamic loading of the seat with human occupants may also be achieved using MATLAB SIMULINK approaches. Efforts in these directions are currently underway and will be communicated imminently.

Research Ethics

Ethical approval not required.

Author Contributions

The author(s) accept full responsibility for the content of this article and have approved its submission.

Competing Interests

The author(s) declare that there are no competing interests.

Research Funding

Not reported.

Data Availability

Not applicable.

References

[4] Sriram, T. C. (2018). Effect of Anthropometric Variability on Middle-Market Aircraft Seating. *International Journal of Aviation, Aeronautics, and Aerospace*, *5*(1), 7. https://doi.org/10.15394/ijaaa.2018.1208

[5] Caputo, F., De Luca, A., Marulo, F., Guida, M., & Vitolo, B. (*2018*). Numerical-experimental assessment of a hybrid FE-MB model of an aircraft seat sled test. *International Journal of Aerospace Engineering*, 2018, 8943826. https://doi.org/10.1155/2018/8943826

[6] Bhonge, P., & Lankarani, H. (*2008*). Finite element modeling strategies for dynamic aircraft seats. *SAE Technical Paper*, *2008*, 2272. https://doi.org/10.4271/2008-01-2272.

[7] Alexander, R. (1997). Building Composite Aircraft Part 1. Retrieved from Experimental Aircraft Association: https://www.eaa.org/eaa/aircraft-building/builderresources/while-youre-building/building-articles/composite/building-composite-aircraft-part-1#:~:text=Three%20types%20are%20used%20most,varying%20physical%20characteristics%20and%20cost.

[8] Bilezikjian, V. (1996). U.S. Patent No. 5,553,923. Washington, DC: U.S. Patent and Trademark Office.

[9] Ahmadpour, N., Lindgaard, G., Robert, J. M., & Pownall, B. (2014). The thematic structure of passenger comfort experience and its relationship to the context features in the aircraft cabin. *Ergonomics*, *57*(6), 801-815. https://doi.org/10.1080/00140139.2014.899632

[10] Bouwens, J., Tsay, W. J. J., & Vink, P. (2017). The high and low comfort peaks in passengers' flight. *Work*, *58*(4), 579-584. https://doi.org/10.3233/WOR-172637

[11] Alan, G., & Hanser, V. (2009). Finite element analysis. In: Gent, A.N. (Ed.), Elasticity in Engineering with Rubber. In R. Finney, *How to design Rubber components* (pp. 36-46).

[12] Hwang, H. Y., Choi, K. K., & Chang, K. H. (1997). Second-order shape design sensitivity using P-version finite element analysis. *Structural optimization*, *14*, 91-99. https://doi.org/10.1007/BF01812510

[13] Nayroles, B., Touzot, G., & Villon, P. (1992). Generalizing the finite element method: diffuse approximation and diffuse elements. *Computational mechanics*, *10*(5), 307-318. https://doi.org/10.1007/BF00364252

[14] Meola, C., Boccardi, S., & Carlomango, G. (2017). *In Infrared Thermography in the Evaluation of Aerospace Composite Materials. Composite Materials in the Aeronautical Industry*, 1-24.

[15] Atkinson, K. (1991). An in*troduction to numerical analysis. John* wiley & sons.

[16] Brauer, J. (2010). What Every Engineer Should Know About Finite Element Analysis. In Finite *Element Analysis (pp.* 36-40).

[17] Kassapoglou, C. (2013). Desig*n and analysis of composite structures: with applications to aerospace structures. John* Wiley & Sons.

[18] Cook, R. (1995). Finite *Element Modeling for Stress Analysis. New Jersy.*

[19] Bhonge, P. (2016). Metho*dology for Aircraft Seat Certification by Dynamic Finite Element Analysis. Wi*chita State University.

EUROPEAN MECHANICAL SCIENCE

Research Article

e-ISSN: 2587-1110

An analysis of the impact of nanofluids on the cooling effectiveness of pin and perforated heat sinks

Taha Tuna Göksu[1]*

[1]Adiyaman University, Mechanical Engineering Department, Türkiye

Orcid: T. T. Göksu (0000-0003-2028-3362)

Abstract: In the presented numerical study, the effect of the use of mono and hybrid (CuO/Water at 2% volume concentration and CuO + Fe/Water (1% CuO + 1% Fe)) type nanofluid in heat sinks designed in new geometric structures used to increase the processor cooling performance was investigated. The geometries used are circular, triangular, square, hexagonal, square, and hexagonal, and their perforated structures and their effects on a total of eight geometries were analyzed. In addition to these, the rate of improving the temperature distribution and heat transfer in the heat sink, i.e., the Performance Evaluation Criterion (PEC), was also examined. According to the results obtained, the lowest thermal resistance value is seen in the circular cross-section with R_{th} = 0.289 K/W, while the highest thermal, i.e., cooling performance is seen in the triangular perforated structure with R_{th} = 0.63 K/W and at the lowest pressure inlet condition. In terms of temperature distribution, the most uniform distribution was obtained between 311.82 and 308.98 K in the circular section. The most interesting result in terms of the results was the PEC = 1.4 for the triangular hole structure in the heat transfer improvement performance. The main reason for this is that the range of the temperature distribution shown is very high (319–311.5K).

Keywords: heat sink, mono-hybrid nanofluid, PEC, thermal resistance

1. Introduction

Thermal problems in central processing unit (CPU) equipment need the use of passive cooling methods, such as pin or plate fin heat sinks (HS), to ensure effective heat transfer and cost efficiency [1–4]. The research conducted by Chiu et al. [5,6] examined the cooling effectiveness of pin-type HS with circular cross-sections using both computational and experimental approaches. HS performance is highly influenced by factors such as fin dimensions, forms, quantity, arrangement, heat surface placement, and coolant type. Göksu et al. [7,8] have obtained important results of heat transfer improvement by using passive methods, i.e., geometrical modifications, in their studies. Kuru [9] investigates the performance of triangular ribbed plate fin HS, focusing on their thermal efficiency, weight, volume, and cost reduction. The results show that increasing velocity, fin height, number of fins, and triangular rib height leads to lower pressure drop and increased HS volume and weight. Different manufacturing techniques also play an important role in the design of heat sinks; for example, pin-type geometry with additive manufacturing was designed and its effects analyzed [10]. Thangavel and Sekar [11] designed a lotus-type heat sink, analyzed the temperature distributions in laminar and turbulent flow, and observed that they decreased up to 302 K.

Nanofluids (NFs) are being used more and more to improve heat transfer in different HS setups because to their high thermal conductivity and density. The computational study conducted by Kavitha et al. [12] demonstrated a significant 68% enhancement in heat transfer for a fin-type HS by utilizing Al_2O_3/water nanofluid. Choi [13] initially introduced the notion of employing nanoparticles in coolant. Choi and Eastman [14] employed NFs to enhance thermal control in electronic applications. Wu et al. [15] investigated the use of Al_2O_3-water NF in copper microchannel HS, as well as graphene/water NF for cooling serpentine and sinusoidal spiral architectures in heat sinks. In a study, it was shown that the utilization of a sinusoidal winding fin design was more effective when combined with a graphene/water NF on HS that had serpentine and sinusoidal spiral designs [16].

*Corresponding author:
Email: tgoksu@adiyaman.edu.tr

Cite this article as:
Göksu, T. T. (2024). An analysis of the impact of nanofluids on the cooling effectiveness of pin and perforated heat sinks. *European Mechanical Science*, *8*(2): 71-77. https://doi.org/10.26701/ems.1466806

History dates:
Received: 08.04.2024, *Revision Request*:24.04.2024, *Last Revision Received*: 30.04.2024, *Accepted*: 01.05.2024

An investigation was conducted on a mini-channel HS with a wavy design to assess its cooling performance using supercritical CO_2. Results showed a significant 8.58-fold rise in the heat transfer coefficient at the lowest input temperature of 305 K [17]. The combination of wavy fins and square fins greatly enhances the performance of an inclined cooler box that contains magnetized-radiative NF, resulting in a notable improvement [18,19]. The utilization of NF-cooled fins with circular, square, and triangular shapes led to significant enhancements in the Nusselt number, with increases of 23.1%, 16.5%, and 8%, correspondingly [20]. The integration of the Eulerian-Lagrangian approach with NF results in a significant 16% improvement in the heat transfer coefficient of a micro pin-fin HS [21,22]. Cabir [23] and Uçkan et al. [24,25] are noteworthy in this regard in their studies on fuels.

Moreover, a study investigating the utilization of MgO/water, TiO_2/water, and Al_2O_3/water, NFs in a rectangular microchannel HS revealed that Al_2O_3/water and MgO/water NFs yielded superior outcomes [26]. The study examines [27] the impact of nanoparticle morphology on thermal conductivity in microchannels, focusing on hybrid and mono NFs. Results show that Al_2O_3 mono NF increases thermal conductivity by 12%, while hybrid NF based water increases it by 18.6%. TiO_2 nanoparticles have the highest thermal resistance. Ozbalcı et al. [28] conducted research indicating that the combination of nanofluids and metal foam is an economical and energy-efficient method for cooling electronic systems. Karaaslan and Menlik [29] conducted a study to examine the effects of mono and hybrid NFs on the cooling of solar panels. The mono-hybrid nanofluids they use are CuO/Water and CuO+Fe/Water. The reason for choosing these two fluid types is that the thermophysical properties of nanofluids are better, as mentioned above. The behavior of hybrid nanofluids can be more precisely estimated at lower concentrations of nanoparticles. Therefore, a concentration of 2% is deemed the most appropriate for this experiment [30]. In their study, Ho et al. [31] investigated the impact of ultrapure water and water-based alumina NFs with volume concentrations of 0.5% and 1% on a micro-channel HS. They observed a significant 14.43% enhancement in the heat transfer coefficient. Sriharan et al. [32] conducted a study to examine how the use of nanofluids Al_2O_3, MgO, and CuO affects the convective heat transfer coefficient in a HS with a hexagonal tube. The results indicated a significant increase of 40%, 28%, and 22% for Al_2O_3, MgO, and CuO, respectively.

Göksu[33] investigated the cooling performance of mono and hybrid NFs in block-type HS, and the results showed that mono NF provided much better thermal resistance than water fluid and partially lower thermal resistance than hybrid NF. It was observed that Al_2O_3 NF provides lower thermal resistance than water fluid when used in block-type structures [34]. In another study, Göksu [35] designed heat sinks with circular, triangular, square, and hexagonal cross-sections and their perforated versions and investigated their cooling performance using water fluid. The results showed that R_{th} = 0.29 K/W had the lowest thermal resistance. The present study examined the effects of using mono and hybrid nanofluid instead of water in HS designed in circular, triangular, square, and hexagonal sections, as well as their perforated versions from the previous study. The primary driving force behind this examination was the impact of mono and hybrid nanofluids on block-type structures in a previous study, which raised questions about the cooling capabilities of pin and perforated pin structures. Within this framework, it will assess and contrast the cooling and heat transfer enhancements achieved by water, mono nanofluids, and hybrid nanofluids.

2. Geometry and Boundary Condition

The geometries used in the present study are the same as those used in the previous study [35]. These geometries are circular, triangular, square, square, hexagonal, and their perforated versions. Four different inlet pressures are used as boundary conditions (689, 1370, 2040, 2750 Pa), and a constant heat flux is applied to the bottom side of the heat sink. Central Processing Unit (CPU) analyses were carried out using the ANSYS FLUENT module. The k-ε turbulence module was used, and SIMPLE was selected as the solver. The residual stress values were kept the same as in the previous study. Equation 1 uses the thermal resistance (R_{th}) as the fundamental parameter to gauge the system's cooling efficiency. The system cools more efficiently the lower this value is. Equations 2–5 display the heat transfer coefficient, friction factor, Reynolds number, and Performance Evaluation Criteria (PEC). The present study uses both mono (CuO/Water-2% concentration) and hybrid (CuO-1%+Fe/Water-1% concentration) solutions. The equations used in the calculation of the physical properties of the fluids are given in 6–13 equations [33].

$$R_{th} = \frac{T_{CPU,m} - T_{in}}{q''}, \tag{1}$$

$$h = \frac{q''}{T_{CPU,m} - T_{bf,\mathrm{th}}}, \tag{2}$$

$$Re = \frac{\rho . V . D_h}{\mu}, \tag{3}$$

$$f = \frac{2 . \Delta P . D_h}{\rho . L . V^2}, \tag{4}$$

$$PEC = \frac{{h_a}/{h_0}}{\left({f_a}/{f_0}\right)^{1/3}}. \tag{5}$$

$$\rho_{nf} = \varphi\rho_p + (1-\varphi)\rho_{bf}, \tag{6}$$

$$\mu_{nf} = \frac{\mu_{bf}}{(1-\varphi)^{2.5}}, \tag{7}$$

$$\frac{k_{nf}}{k_{bf}} = \frac{3\left(\frac{k_f}{k_{bf}} - \varphi\right)}{\left(\frac{k_f}{k_{bf}} + 2\right) - \left(\frac{k_f}{k_{bf}} - 1\right)\varphi}, \tag{8}$$

$$(\rho C)_{nf} = \varphi_p \rho_p C_p + (1-\varphi_p)\rho_{bf} C_{bf}. \quad (9)$$

$$\rho_{hnf} = \varphi_1 \rho_{p1} + \varphi_2 \rho_{p2} + (1-(\varphi_1+\varphi_2))\rho_{bf}, \quad (10)$$

$$\mu_{hnf} = \mu_{bf}(1 + 32.795\varphi - 7214\varphi^2 + 714600\varphi^3 - 0.194110^8\varphi^4), \quad (11)$$

$$\frac{k_{nf}}{k_{bf}} = \left(\frac{1.747.10^6 + \varphi_p}{1.747.10^6 - 1.498.10^6\varphi_p + 1.117.10^8\varphi_p^2 + 1.997.10^9\varphi_p^3} \right), \quad (12)$$

$$(\rho C)_{hnf} = \varphi_{p1}\rho_{p1}C_{p1} + \varphi_{p2}\rho_{p2}C_{p2} + (1-\varphi_{p1}-\varphi_{p2})C_{bf}. \quad (13)$$

3. Result and Discussion

This chapter will be analyzed in three sections. The sections are categorized according to the fluids used, and the first one highlights the results of the previous study [35], i.e., when water fluid is used, the second one highlights the results when mono nanofluid is used, and the last section highlights the results when hybrid nanofluid is used. According to the numerical data, the highest flow rate shows a maximum deviation of 4.69% in R_{th}, while the maximum variation in $\dot{V}$ is 6.42% at a pressure of 1370 Pa. These variations are worth mentioning as they are within the permissible range of less than 10%, which demonstrates the accuracy of the numerical simulations.

3.1. Water Utilization Findings

The thermal resistance, temperature distribution, and PEC results obtained in the previous study [35] are shown in Figures 1, 2, and 3, respectively. As can be seen from the figures, the thermal resistance values decrease with increasing pressure, and the lowest thermal resistance was obtained as R_{th} = 0.29 K/W at P = 2750 Pa. It is clearly seen from the figure that the geometry that can be used in terms of cooling performance after the circular cross-sectional structure is the heat sink in the square hole structure. The specified value was obtained in the circular-section pin heat sink. In the temperature distribution, the situation is the same; that is, it is seen that the temperature decreases with increasing pressure, and the most uniform temperature distribution (311.3–308.73 K) was obtained in the circular section pin type heat sink. When the Performance Evaluation Criteria (PEC) were evaluated, the highest PEC = 1.18 was obtained at P = 689 Pa. Another important result is that the heat sink with a triangular cross-sectional structure has the lowest PEC values.

3.2. Mono-Nanofluid Utilization Findings

Figures 4, 5, and 6 display the thermal resistance, temperature distribution, and PEC results obtained using mono (CuO/Water, 2% concentration) nanofluid, respectively. The numerical results indicate that the heat sink in the circular cross-section has the lowest thermal resistance value of R_{th} = 0.289 K/W. Overall, the circular cross-section yields better results than the other cross-sections. It is evident that the value is lower than that of water fluid. This finding is one of the most significant outcomes of using nanofluid to cool heat sinks. Among the perforated structures, the square hole structure exhibited the lowest thermal resistance, with R_{th}=0.302 K/W. The most uniform temperature distribution was achieved in the 311.34–308.67 K range, particularly in the circular section heat sink. This range is comparatively better than that achieved using water fluid. One of the key findings

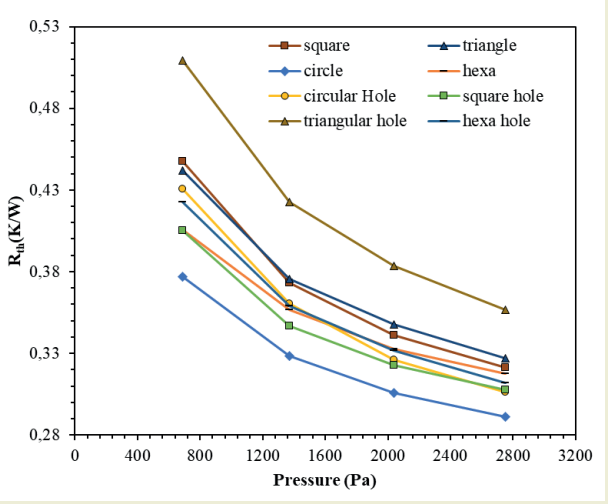

Figure 1. Compare of pressure vs. thermal resistance.

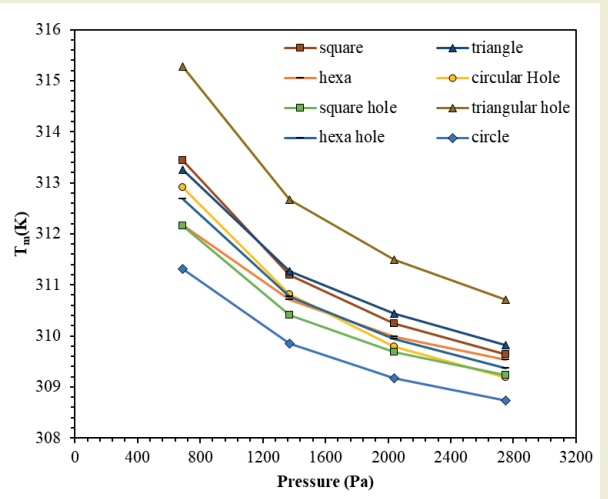

Figure 2. Mean temperature vs. pressure.

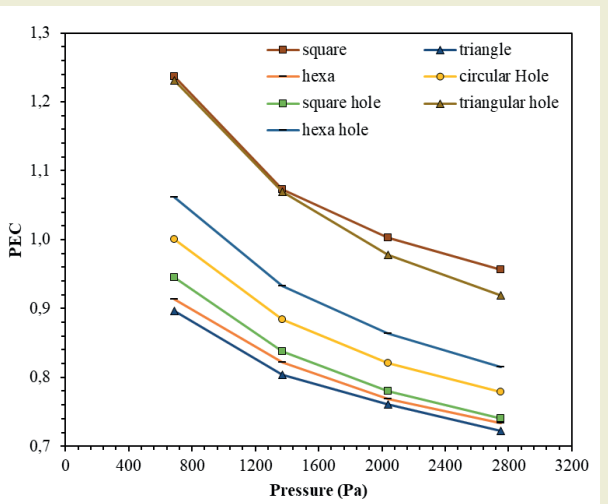

Figure 3. PEC vs. pressure drop.

of this study is the PEC value. As shown in Figure 6, the triangular hole structure at P = 689 Pa yielded the highest PEC value of 1.32, which is significantly higher than the highest PEC value of 1.18 observed in water fluid. This indicates that the mono-nanofluid has a considerable impact on PEC values compared to water fluid. From Figure 3, it is evident that the lowest PEC value of 0.71 was obtained when using mono nanofluid, compared to 0.67 when using water fluid.

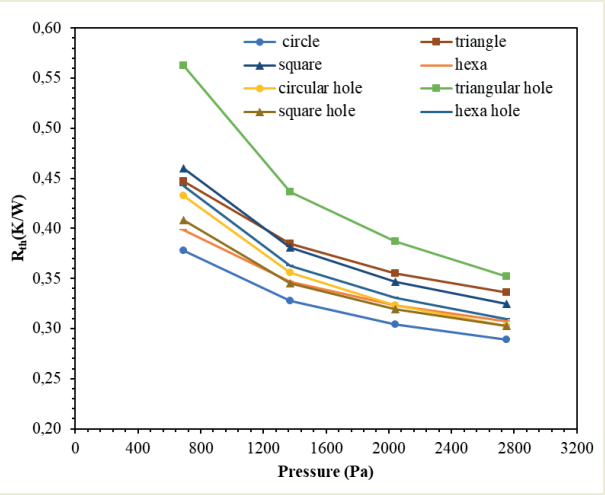

Figure 4. Compare of pressure vs. thermal resistance for mono nanofluid.

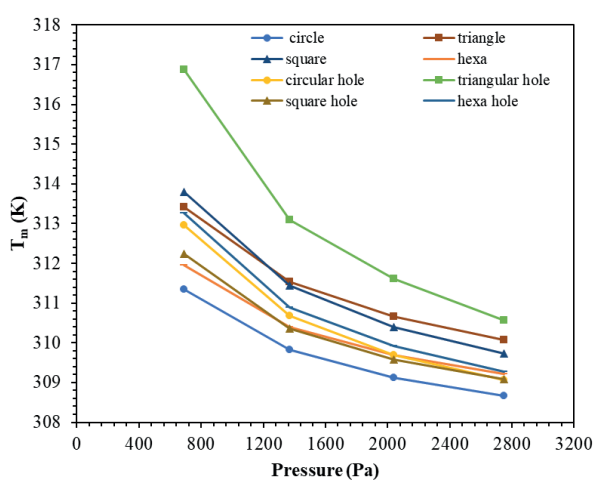

Figure 5. Mean temperature vs. pressure for mono nanofluid.

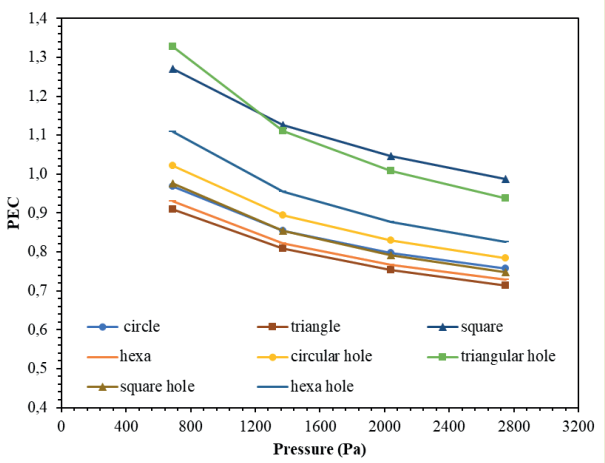

Figure 6. PEC vs. pressure drop for mono nanofluid.

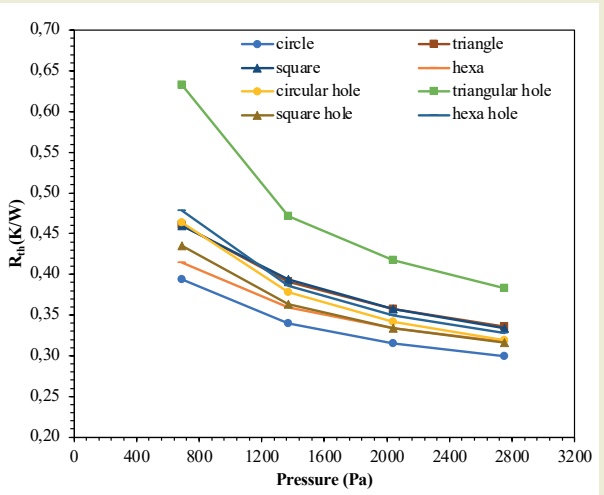

Figure 7. Compare of pressure vs. thermal resistance for hybrid nanofluid.

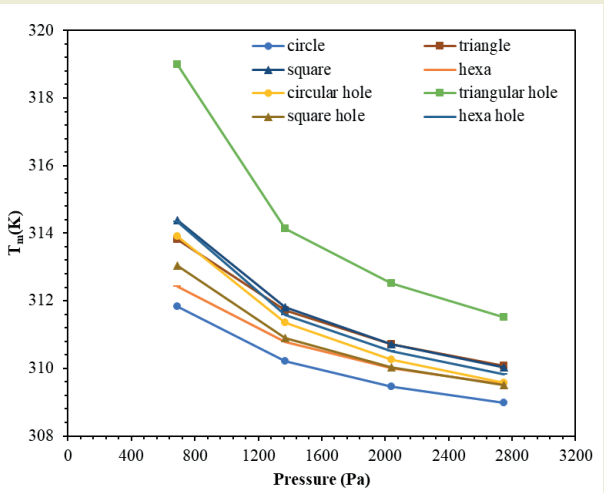

Figure 8. Mean temperature vs. pressure for hybrid nanofluid.

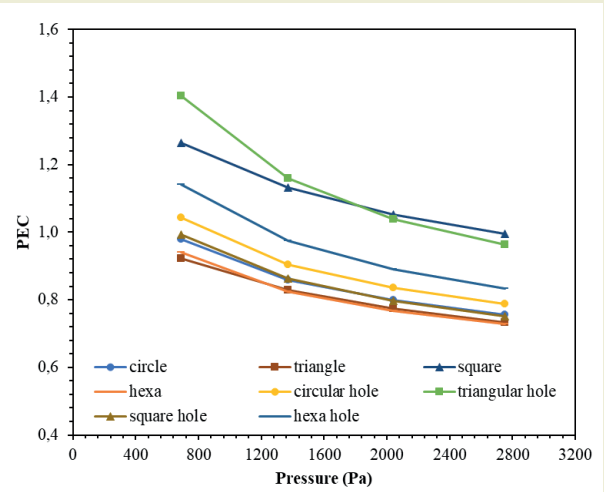

Figure 9. PEC vs. pressure drop for hybrid nanofluid.

3.3. Hybrid-Nanofluid Utilization Findings

Figures 7, 8, and 9 display the thermal resistance, temperature distribution, and PEC results obtained using mono (CuO+Fe/Water) nanofluid, respectively. The circular cross-section heat sink exhibited the lowest thermal resistance and the most uniform temperature distribution, with values of R_{th} = 0.299 K/W and 311.82–308.98 K, respectively. These values are higher than those of the mono nanofluid. The study concludes that the hybrid nanofluid is not more efficient than the mono nanofluid in terms of thermal resistance and temperature distribution. However, it is quite efficient in terms of heat enhancement factor (PEC). Figure 9 shows that the maximum PEC is 1.32 in the mono nanofluid, while it is 1.40 in the hybrid nanofluid. Although the lowest PEC value in mono nanofluid is 0.67, the value of 0.733 in hybrid nanofluid indicates its superior efficiency in terms of heat recovery.

4. Conclusion

The key findings regarding the cooling, temperature distribution, and heat recovery performances of mono and hybrid nanofluids in the heat sink are as follows:

1. The heat resistance of the mono nanofluid was reduced compared to both the water fluid and the hybrid nanofluid. The circular sectioned heat sink achieved the lowest thermal resistance, with a value of R_{th}=0.289 K/W.

2. The evaluation of temperature distribution indicated that the mono nanofluid exhibited a more consistent temperature distribution compared to the hybrid and water fluids.

3. The temperature distribution was obtained in the range of approximately 311-308 K for both mono and hybrid nanofluids. This range's narrowness is an indication of how uniform the temperature distribution is.

4. Upon comparing the results in terms of PEC, it was seen that the hybrid nanofluid exhibited much higher values compared to both the mono nanofluid and water fluid. The heat sink with triangular holes achieved the greatest PEC value of 1.40. The impact of perforated structures, particularly in PEC outcomes, serves as the fundamental measure of the effectiveness of the planned geometries.

Nomenclature

a	results parameter of specified study
C_p	specific heat, J.kg^{-1}·K^{-1}
D_h	hydraulic diameter, m
f	friction factor
h	convection heat transfer coefficient, W.m^{-2}·K^{-1}
k	thermal conductivity, W.m^{-1}·K^{-1}
q''	heat flux, W.m^{-2}
R_{th}	effective thermal resistance K.W^{-1}
T	temperature, K

Greeks

μ	dynamic viscosity, Pa·s
ρ	density, kg.m^{-3}
0	results parameters of experimental study

Abbreviations

CFD	computational fluid dynamics
CPU	central processing unit
HS	heat sink
NF	nanofluid
PEC	performance evaluation criterion

Research Ethics

Ethical approval not required.

Author Contributions

The author(s) accept full responsibility for the content of this article and have approved its submission.

Competing Interests

The author(s) declare that there are no competing interests.

Research Funding

Not reported.

Data Availability

Not applicable.

References

[1] Ajayan, J., Nirmal, D., Tayal, S., Bhattacharya, S., Arivazhagan, L., Fletcher, A. A., & Ajitha, D. (2021). Nanosheet field effect transistors-A next generation device to keep Moore's law alive: An intensive study. *Microelectronics Journal, 114*: 105141. https://

doi.org/10.1016/j.mejo.2021.105141.

[2] Matallana, A., Ibarra, E., López, I., Andreu, J., Garate, J. I., Jordà, X., & Rebollo, J. (2019). Power module electronics in HEV/EV applications: New trends in wide-bandgap semiconductor technologies and design aspects. *Renewable and Sustainable Energy Reviews*, *113*, 109264. https://doi.org/10.1016/j.rser.2019.109264.

[3] Jayaramu, P., Gedupudi, S., & Das, S. K. (2021). Experimental investigation of the influence of boiling-induced ageing on high heat flux flow boiling in a copper microchannel. *International Journal of Heat and Mass Transfer*, *181*: 121862. https://doi.org/10.1016/j.ijheatmasstransfer.2021.121862.

[4] Al-Neama, A. F., Kapur, N., Summers, J., & Thompson, H. M. (2018). Thermal management of GaN HEMT devices using serpentine minichannel heat sinks. *Applied Thermal Engineering*, *140*, 622-636. https://doi.org/10.1016/j.applthermaleng.2018.05.072.

[5] Chiu, H. C., Hsieh, R. H., Wang, K., Jang, J. H., & Yu, C. R. (2017). The heat transfer characteristics of liquid cooling heat sink with micro pin fins. *International communications in heat and mass transfer*, *86*, 174-180. https://doi.org/10.1016/j.icheatmasstransfer.2017.05.027.

[6] Chiu, H. C., Youh, M. J., Hsieh, R. H., Jang, J. H., & Kumar, B. (2023). Numerical investigation on the temperature uniformity of micro-pin-fin heat sinks with variable density arrangement. *Case Studies in Thermal Engineering*, *44*, 102853. https://doi.org/10.1016/j.csite.2023.102853.

[7] Göksu, T. T., & Yılmaz, F. (2021). Numerical comparison study on heat transfer enhancement of different cross-section wire coils insert with varying pitches in a duct. *Journal of Thermal Engineering*, *7*(7), 1683-1693. https://doi.org/10.18186/thermal.1025930.

[8] Yılmaz, İ. H., & Göksu, T. T. (2019). Enhancement of heat transfer using twisted tape insert in a plain tube. *Bitlis Eren Üniversitesi Fen Bilimleri Dergisi*, *8*(1): 251-260. https://doi.org/10.17798/bitlisfen.462169.

[9] Kuru, M. N. (2023). The effect of the triangular rib usage in the plate fin heat sinks on the pressure drop, base plate temperature, and entropy generation. *European Mechanical Science*, *7*(2), 99-108. https://doi.org/10.26701/ems.1276575.

[10] Parlak, M. (2024). Thermal management with double layered heat sink produced by direct metal laser sintering. *International Journal of Energy Studies*, *9*(1): 155-173. https://doi.org/10.58559/ijes.1439889.

[11] Thangavel, P., & SEKAR, A. (2021). Investigations on Heat Transfer Characteristics of Porous type Copper Heat Sink with Bifurcations. *Journal of Thermal Engineering*, *7*(3): 584-594. https://doi.org/10.18186/thermal.888428.

[12] Mukeshkumar, P. C., & Kumar, A. (2023). Numerical study on the performance of Al2O3/water nanofluids as a coolant in the fin channel heat sink for an electronic device cooling.,-*Materials Today: Proceedings*. https://doi.org/10.1016/j.matpr.2023.02.337.

[13] Siginer, D. A., & Wang, H. P. (1995). Developments and Applications of Non-Newtonian Flows, 1995: Presented at the 1995 *ASME International Mechanical Engineering Congress and Exposition*, November 12-17, 1995, San Francisco, California.

[14] Choi, S. U., & Eastman, J. A. (1995). *Enhancing thermal conductivity of fluids with nanoparticles* (No. ANL/MSD/CP-84938; CONF-951135-29). Argonne National Lab.(ANL), Argonne, IL (United States).

[15] Wu, X., Wu, H., & Cheng, P. (2009). Pressure drop and heat transfer of Al2O3-H2O nanofluids through silicon microchannels. *Journal of Micromechanics and Microengineering*, *19*, 105020. https://doi.org/10.1088/0960-1317/19/10/105020.

[16] Ghadikolaei, S. S., Siahchehrehghadikolaei, S., Gholinia, M., & Rahimi, M. (2023). A CFD modeling of heat transfer between CGNPs/H2O Eco-friendly nanofluid and the novel nature-based designs heat sink: Hybrid passive techniques for CPU cooling. *Thermal Science and Engineering Progress*, *37*, 101604. https://doi.org/10.1016/j.tsep.2022.101604.

[17] Khoshvaght-Aliabadi, M., Ghodrati, P., Mortazavi, H., & Kang, Y. T. (2023). Numerical analysis of heat transfer and flow characteristics of supercritical CO2-cooled wavy mini-channel heat sinks. *Applied Thermal Engineering*, *226*, 120307. https://doi.org/10.1016/j.applthermaleng.2023.120307.

[18] Massoudi, M. D., & Hamida, M. B. B. (2023). Combined impacts of square fins fitted wavy wings and micropolar magnetized-radiative nanofluid on the heat sink performance. *Journal of Magnetism and Magnetic Materials*, *574*, 170655. https://doi.org/10.1016/j.jmmm.2023.170655.

[19] Seyf, H. R., & Feizbakhshi, M. (2012). Computational analysis of nanofluid effects on convective heat transfer enhancement of micro-pin-fin heat sinks. *International Journal of Thermal Sciences*, *58*, 168-179. https://doi.org/10.1016/j.ijthermalsci.2012.02.018.

[20] Ambreen, T., Saleem, A., & Park, C. W. (2019). Pin-fin shape-dependent heat transfer and fluid flow characteristics of water-and nanofluid-cooled micropin-fin heat sinks: Square, circular and triangular fin cross-sections. *Applied Thermal Engineering*, *158*, 113781. https://doi.org/10.1016/j.applthermaleng.2019.113781.

[21] Cai, W., Toghraie, D., Shahsavar, A., Barnoon, P., Khan, A., Beni, M. H., & Jam, J. E. (2021). Eulerian-Lagrangian investigation of nanoparticle migration in the heat sink by considering different block shape effects. *Applied Thermal Engineering*, *199*, 117593. https://doi.org/10.1016/j.applthermaleng.2021.117593.

[22] Yasir, M., Khan, M., Alqahtani, A. S., & Malik, M. Y. (2023). Numerical study of axisymmetric hybrid nanofluid MgO-Ag/H2O flow with non-uniform heat source/sink. *Alexandria Engineering Journal*, *75*, 439-446. https://doi.org/10.1016/j.aej.2023.05.062.

[23] Cabir, B., & Yakın, A. (2024). Evaluation of gasoline-phthalocyanines fuel blends in terms of engine performance and emissions in gasoline engines. *Journal of the Energy Institute*, *112*, 101483. https://doi.org/10.1016/j.joei.2023.101483.

[24] Uçkan, İ., Yakın, A., & Behçet, R. (2024). Second law analysis of an internal combustion engine for different fuels consisting of NaBH4, ethanol and methanol mixtures. *International Journal of Hydrogen Energy*, *49*, 1257-1267. https://doi.org/10.1016/j.ijhydene.2023.10.302.

[25] Uçkan, İ., Yakın, A., & Behçet, R. (2024). Investigation of the effect of dead-state temperature on the performance of boron-added fuels and different fuels used in an internal combustion engine. *Heat Transfer Research*, *55*(12). https://doi.org/10.1615/HeatTransRes.2024050089.

[26] Mukherjee, S., Wciślik, S., Khadanga, V., & Mishra, P. C. (2023). Influence of nanofluids on the thermal performance and entropy generation of varied geometry microchannel heat sink. *Case Studies in Thermal Engineering*, *49*, 103241. https://doi.or-

g/10.1016/j.csite.2023.103241.

[27] Al-Fatlawi, A. W., & Niazmand, H. (2024). Thermal analysis of hybrid nanofluids inside a microchannel heat exchanger for electronic cooling. *Journal of Thermal Analysis and Calorimetry*, *149*, 4119-4131. https://doi.org/10.1007/s10973-024-12991-2.

[28] Ozbalci, O., Dogan, A., & Asilturk, M. (2023). Performance of discretely mounted metal foam heat sinks in a channel with nanofluid. *Applied Thermal Engineering*, *235*, 121375. https://doi.org/10.1016/j.applthermaleng.2023.121375.

[29] Karaaslan, I., & Menlik, T. (2021). Numerical study of a photovoltaic thermal (PV/T) system using mono and hybrid nanofluid. *Solar Energy*, *224*, 1260-1270. https://doi.org/10.1016/j.solener.2021.06.072.

[30] Martin, K., Sözen, A., Çiftçi, E., & Ali, H. M. (2020). An experimental investigation on aqueous Fe–CuO hybrid nanofluid usage in a plain heat pipe. *International Journal of Thermophysics*, *41*, 1-21. https://doi.org/10.1007/s10765-020-02716-6.

[31] Ho, C. J., Peng, J. K., Yang, T. F., Rashidi, S., & Yan, W. M. (2023). On the assessment of the thermal performance of microchannel heat sink with nanofluid. *International Journal of Heat and Mass Transfer*, *201*, 123572. https://doi.org/10.1016/j.ijheatmasstransfer.2022.123572.

[32] Sriharan, G., Harikrishnan, S., & Oztop, H. F. (2022). Performance improvement of the mini hexagonal tube heat sink using nanofluids. *Thermal Science and Engineering Progress*, *34*, 101390. https://doi.org/10.1016/j.tsep.2022.101390.

[33] Göksu, T. T. (2024). Enhancing cooling efficiency: Innovative geometric designs and mono-hybrid nanofluid applications in heat sinks. *Case Studies in Thermal Engineering*, 104096. https://doi.org/10.1016/j.csite.2024.104096.

[34] Göksu T. T. (2024) Numerical investigation of the cooling effect of Al2O3 nanofluid in heat sinks. *All Sciences Academy*, 1277–1284.

[35] Göksu, T. T. (2024). Investigation of pin and perforated heatsink cooling efficiency and temperature distribution. *Journal of Thermal Analysis and Calorimetry*, 1-13. https://doi.org/10.1007/s10973-024-13078-8.

EUROPEAN MECHANICAL SCIENCE

Research Article

e-ISSN: 2587-1110

Water park of the future: Monarch butterfly slide with eco-friendly design and smart water management

Yusuf Uzun[1*], Mehmet Kayrıcı[2], Nazmi Türkhan[3], Dila Yaz[3]

[1]Necmettin Erbakan University, Seydisehir Ahmet Cengiz Faculty of Engineering, Department of Computer Engineering, 42370, Konya, Türkiye
[2]Necmettin Erbakan University, Seydisehir Ahmet Cengiz Faculty of Engineering, Department of Mechanical Engineering, 42370, Konya, Türkiye
[3]Polgün Waterparks & Attractions, Mugla, Türkiye

Orcid: M. Kayrici (0000-0003-1178-5168), Y. Uzun (0000-0002-7061-8784), H. Arikan (0000-0003-1266-4982), A. Karaveli (0000-0001-5044-1929)

Abstract: In this study, an innovative water park concept slide that aims to keep water consumption low was designed and produced. Traditional water parks are out of use at a rate of approximately 65% because they are inefficient in water and energy consumption. This work will be a pioneering step in the sector with the combination of environmentally friendly design, smart water management systems, and sustainable technologies. Users entering the 43% inclined butterfly body will reach a speed of 16 m/sec while performing the vertical swing movement and will move with an acceleration of 0.5m/sec^2 on the horizontal axis. Since the high-pressure water coming from the nozzles on the slide will be used only when there is movement, approximately 70% water and 50% energy savings will be achieved and sliding safety will also be increased. The proposed saving system will be produced using the inverter, integrated circuit, smart card, and software developed to be added to the pump and will be adapted to all slides. The fact that this study is a first in the sector will inspire other water parks and lead to the development of projects that consider sustainability and savings issues.

Keywords: waterslide, eco-friendly design, water saving, polgün

1. Introduction

Nowadays, environmental sustainability and the protection of natural resources are becoming increasingly important around the world. Water is one of the most important elements for the continuation of life on Earth. With increasing economic growth and population, water demand also increases; Water availability is constantly being depleted, and increasing pressure on freshwater resources requires monitoring of water consumption. In addition to controlling water supply through an efficient water management system, automation of the system in terms of both monitoring and operation has attracted great attention in recent years and helps reduce operating costs and save energy [1,2]. The responsibility of protecting water resources, reducing clean water consumption, and leaving a cleaner environment for future generations has become a global necessity [3]. In this context, rational and effective use of water, sustainable management of water resources, and reduction of energy consumption are of great importance, especially in the water-related entertainment sector [4].

Rapid urbanization and population growth have affected the environment in many ways, including greenhouse gas emissions (e.g. CO_2). In addition, increasing prosperity has increased human mobility in the world, and the tourism sector has received a large share of this [5]. To reduce energy consumption and use energy more effectively and efficiently in tourism sectors, it is important where and how energy is used [6]. In line with this information, it will be possible to determine the areas where energy savings will be made and to focus on these areas. Performance, optional materials, energy consumption, phase of use, durability, recycling, reuse, and disposal have an important place in eco-design, as well as efficiency issues [7,8]. Eco-design is an industrial approach that aims to reduce environmental impact at every stage of the product life cycle [9]. While early developments in sustainable design stemmed from the desire to reduce environmental impacts throughout the life cycle, recent focus has brought the three aspects of sustainability (environment, economy, and society) into the spotlight more broadly

*Corresponding author:
Email: yuzun@erbakan.edu.tr

Cite this article as:
Uzun, Y., Kayrıcı, M., Türkhan, N., Yaz, D. (2024). Water park of the future: monarch butterfly slide with eco-friendly design and smart water management. *European Mechanical Science, 8*(2): 78-84. https://doi.org/10.26701/ems.1430128

History dates:
Received: 07.02.2024, ***Revision Request***: 25.04.2024, ***Last Revision Received***: 03.05.2024, ***Accepted***: 22.05.2024

[10]. Considering the environmental knowledge and attitudes of tourists in recent years, it has been understood that nature-based water parks are more important in recreational ecosystem services [11,12]. Sustainable development has emerged by including sustainability social, economic, and environmental factors [13]. Over time, the concept of sustainability has taken different dimensions and emerged in different fields such as sustainable tourism, sustainable business, and sustainable living [14]. It is seen that smart applications in tourism are becoming increasingly widespread in these areas. In this context, concepts such as smart tourism, smart destination, smart hotel, smart transportation, and smart activity are frequently encountered [15].

Since tourism-related activities require higher energy consumption, tourism-based growth is achieved at the expense of environmental damage. Additionally, leisure tourism, a subsector of the tourism industry, has a significant and positive impact on energy consumption and economic growth [16]. When the symmetric and asymmetric effects of hotel services on general customer satisfaction are investigated, one of the highest effects is entertainment services. The accelerating development in the tourism sector has led to an increase in the use of theme parks, amusement parks, and water parks. Water parks, established to meet people's needs for many cultural and social activities such as playing games, resting, and doing sports, are water-based active recreational areas that can be designed in different scales and sizes with various activities included [17]. Traditional water parks cause negative environmental impacts in terms of water consumption, water management, and energy.

Therefore, water parks must have innovative and environmentally friendly eco designs and be operated based on sustainability principles. The daily water consumption of a water park can vary greatly depending on its concept, number of visitors, and technological infrastructure. Such parks may attempt to reduce water consumption by using energy efficiency and water conservation techniques [18]. Theme parks generate billions of dollars in revenue, have a substantial effect on local economies and therefore, are considered a significant driver of the hospitality industry [19].

The aim of this study is to be a pioneer in the sector by offering innovative water parks, environmentally friendly design, smart water management systems and sustainable technologies together. The design of the Monarch Butterfly slide presented in the study was developed to allow four people to slide at the same time, with different geometry and sliding behavior. Efficient use of water will be ensured thanks to smart sensors and software installed to control the flow of water during users' sliding movements. This innovative water park concept will provide a significant source of inspiration to the water park and composite manufacturing industry by offering an approach centered on sustainability and water-energy saving, leading to the development of more environmentally friendly projects in the future. This study will contribute to the protection of water resources, energy savings and the dissemination of environmentally friendly entertainment options.

2. Materials and Methods

2.1. Materials

In this study, the Monarch Butterfly waterslide was designed inspired by the butterfly known in nature as the Monarch butterfly. Motifs like those found on the Monarch butterfly are included in the design of the slide. Glass fiber and resin were used as composite materials in the slide (Table 1). The RTM method was preferred because it allows the production of safer and smooth surfaces with precise tolerances. In addition, this system also enables the necessary acoustic and visual designs.

Table 1. Glass-reinforced polyester laminate specification

Material	Material Type	Material Description
Pigmented Gelcoat	İlkester Gin-413	Isophthalic / Neopentyl Glycol / Ultraviolet Lights Gelcoat
Barrier Coat	Bisphenol epoxy	Vinyl ester resin
Reinforcement	Metycore-max-HFD7	RTM / Multiaxial / Roving glass fiber
Polyester Resin	Dewilux Dewester 779 Polyester	RTM / Spray up type polyester resin
Body		6 mm
Flange	S235JR-10	10 mm
Surface Brilliance		Min. 70 gloss
Surface Roughness		Max. 0.08 micron

Raschel fabric used as a pattern is a type of fabric obtained by knitting polyester threads. Thanks to the features and ease of use offered by the fabric, it is frequently preferred in many different sectors. In addition, raschel fabric is preferred over other fabrics due to its weaving structure being durable, flexible, and lightweight. The thinnest version of the raschel fabric is applied between two layers of gelcot to reinforce the composite and give color.

2.2. Methods

Monarch Butterfly will be produced using the Resin Transfer Method (RTM), which is a composite material production technique and is generally used in the manufacturing of parts and hardware in the aviation industry. The most important advantages of this method are that the outer and inner surfaces of the products have the same surface sensitivity, offer excellent visuality, hold less dust, are easy to clean, produce high-quality products, provide standard production, have very low error tolerances, faster and error-free production. It can be expressed as being easier and more importantly, creating less waste in the environment, having more environmentally friendly working conditions, and being sustainable because it is an environmentally friendly technology. At the same time, it is planned to have a transparent pro-

duction with natural light effects and closed sections that will allow ambient light into the slide with different colors and patterns.

In production, after the model is designed, it is separated into molds. In the model design, the model that best reflects the Monarch Butterfly figure, using convex and concave parts with the same radius and slope, was used to give the design a modular structure with minimum cost and a low number of molds. All molds are suitable for production with RTM, and the parts to be removed from the molds are reinforced with 45° woven fibers to provide the desired strength. Patterns will be applied to the parts at the mold stage. These patterns will be machined using RTM technology, a closed molding method in which pre-cut or pre-shaped reinforcing materials are sealed by placing them between the male and female mold. It has become a high-value product with the innovative feature provided by the LED lighting placed on the slide surfaces so that the slide and sensors work at night. RTM process stages are shown in Figure 1.

The metal construction that will ensure the statics of the body is designed by the theme and serves as a hydromechanical installation (Figure 2). This method, used for the first time in the industry, prevents visual pollution caused by PVC pipes.

S235JR was used as steel material (see Figure 3). This steel structure goes through the hot dip galvanization process. It is painted with acrylic-based polyurethane paint as needed. A4 quality stainless steel was used in the fasteners.

Sensors to be placed at critical points on the body of the slide will detect the position of the user and convey the necessary information for the pump, which transfers water to the nozzles on the body, to operate at low or high speed. This system will save approximately 70% of water and 50% of energy when the slide is not used, or the user has not yet reached the body and will increase sliding safety by directing the high-pressure water from the nozzles to the user only when needed. The system will be created using an inverter, integrated circuit, smart card, and developed software to be added to the pump (see Figure 4). In the future, this technology will be adapted to all existing slides. This method, which will be used for the first time in the industry, will lead to the design of sliding geometries that could not be designed before due to safety concerns.

Sustainability-oriented approaches such as efficient use of water used in the study and energy saving play an important role in the design and operation of modern water parks. Additionally, steps have been taken to achieve lower water consumption and high energy efficiency by adopting innovative technologies. These innovations will both sup-

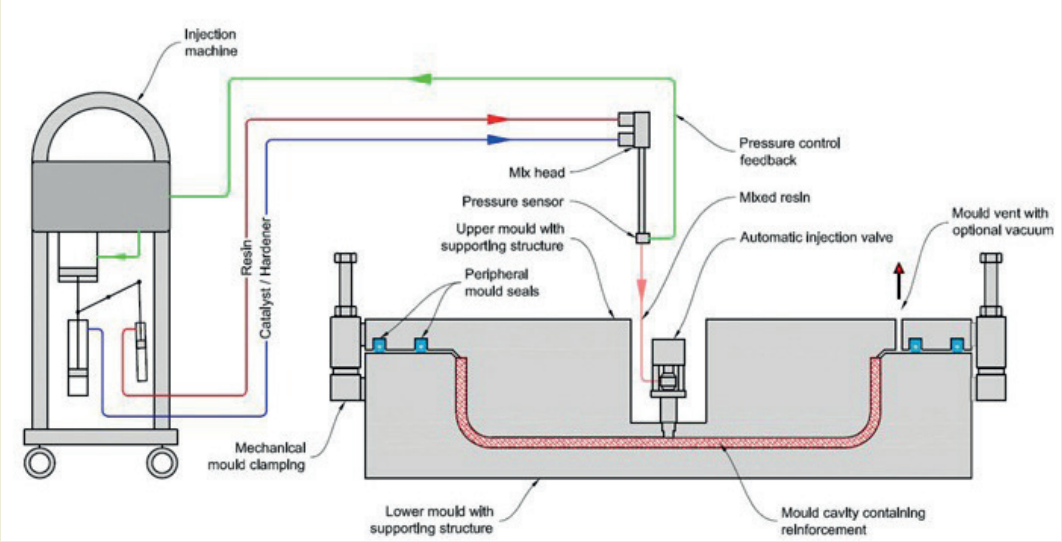

Figure 1. RTM process stages [20]

Figure 2. Monarch Butterfly installation design.

port environmental sustainability and optimize operating energy costs. The comparative technical specifications of the Monarch Butterfly slide are given in Table 2.

Different perspectives of the Monarch Butterfly waterslide are shown in Figure 5.

3. Results and Discussions

The designed waterslide is unique with its unique sliding path, pattern inspired by the Monarch Butterfly, and different color combinations. The slide provides group activity at the same time, allowing 4 people with two boats to have fun by competing. The boats go through bends until they reach the hull, and after a hard landing, the boats that reach the hull rise again and accelerate on the horizontal axis. It gives users the feeling of competition and intense adrenaline at the same time.

Monarch Butterfly offers different geometry and different gliding behaviors together. The slide has three different sliding dynamics. These;

- First, the slide body is reached through the linear classical slide with a near-constant slope. Here, right, and left bends can be preferred within the same section.
- By free falling and climbing within the body, one moves in a valley, first descending, then ascending, and then following the same behavior again.
- While ascending and descending movements are made, with the outward tilt given to the body of the slide, it moves in the horizontal axis within the body and at the same time moves towards the exit of the body.

The slide has two starting entrances placed on the access platform. The sliding platform of the slide is designed to be 1000 m^2 and the sliding capacity is 240 people/hour. The slide with a cross-section of 1400x700 mm is designed to accommodate descent and climbing with a slope of 43% on the Y axis and a slope of 0.78% on the X axis. If the user descends another 10 m on the Y axis, it will allow the user to accelerate to higher speeds although the slope remains constant. The maximum speed reached by users on the butterfly body has been increased to 16 m/s and the average speed has been increased to 9 m/s (Equation 5).

$$E_p = mgh_1, E_k = \frac{1}{2}mV_1^2 \quad (1)$$

$$E_1 = E_p + E_k \quad (2)$$

$$E_2 = \frac{1}{2}mV_2^2 \quad (3)$$

$$f_s = mgk\Delta_x \quad (4)$$

$$E_1 = E_2 + f_s \quad (5)$$

where; h_1 is the initial altitude, V_1 is the initial speed, Δ_x is the total altitude, k is the friction coefficient and V_2 is the final attainable speed (if h_1= 9.08 m, Δ_x = 20.9 m, k= 0.05 (for human), and V_1=10 m/sec then V_2= 16.05 m/sec).

During the swing movement, it will move with an acceleration of 0.5 m/sec^2 on the horizontal axis. A 10 cm deep puddle was created at the exit point of the slide, allowing users to evacuate safely from the slide. The water requirement for Monarch Butterfly is determined as 200m^3/h. Requiring 30% less water than its counterparts, the slide has a significant competitive advantage in water saving. Jet nozzles placed on the sliding surface will be driven by entry and exit sensors, and only when the user reaches the relevant part of the slide, the pump connected to the nozzles will be activated and its speed will be increased by the software and will convey the user to the desired position. This makes the slide an interactive slide according to user behavior. Operating the pump at high speed only when necessary and at idle speed in other cases will reduce the operating costs of the slide. The estimated energy saving is estimated to be approximately 50%.

Monarch Butterfly Waterslide is unique in the industry

Table 2. Comparative technical specifications.

Technical Specifications	Monarch Butterfly	Domestic Competitor	Foreign Competitor
Water consumption	200 m^3/h	250 m^3/h	280 m^3/h
Energy consumption	12 kW	20 kW	24 kW
User capacity in one ride	4 people	4 people	2 people
Used technology	RTM	Hand deposit & RTM	Hand deposit & RTM
Width	24.8 m	24.5 m	20 m
Length	24 m	18.5 m	-
Height	12.7 m	10.5 m	9 m
Tilt	%43	%40	%45-50
Total capacity	240 Persons/h	240 Persons/h	350 Person/h
Start	Platform/Slide	Slide	Platform
Theme	Contains	Contains	Not contain

Figure 3. Preparation of S235JR steel construction

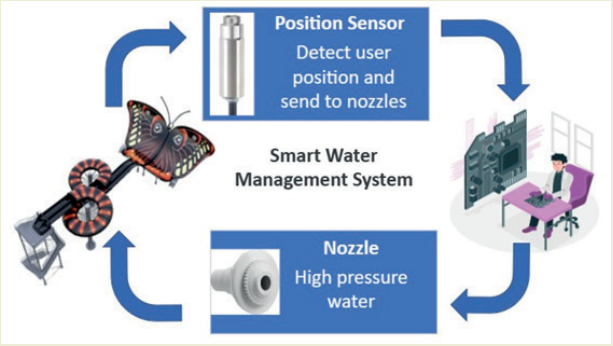

Figure 4. Integrated circuit simulation.

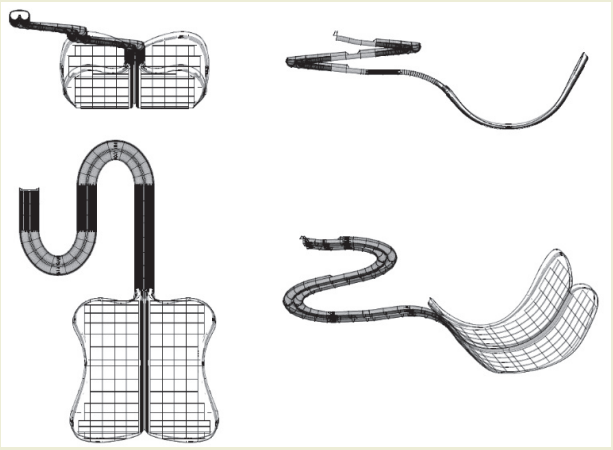

Figure 5. Perspective view of the Monarch Butterfly waterslide

with its design, sliding style, competitive structure, water management technique, and steel construction. With these features, it is aimed to become one of the most prestigious slides in the sector. The Monarch Butterfly waterslide is a slide with double lanes and boats. Since the symmetry used in the slide creates competition between two boats, it is envisaged that the slide will turn into an entertainment vehicle to be slid repeatedly. The developed slide is designed in a way that four people can slide at the same time, unlike general waterslides where a maximum of two people can slide in a single tour. Due to its geometric feature, it provides the user with an entertaining experience thanks to three different sliding dynamics (in the tube, oscillation, and falling) and constantly increasing and decreasing speed. Monarch Butterfly has two starting pieces placed on the access platform. In the two-lane slide, two boats move in the X, Y, and Z axes on the body part after making laps in the same lengths. The sliding platform of the slide is 40 m^2 and the sliding capacity is 200 people/h. High speed (16 m/s) will give users a more enjoyable and exciting sliding experience. The maximum speed reached by users in the sliding process was increased by 15%, from 13m/s to 16m/s. The average speed increased by 6% and reached 9m/s.

According to the laws of physics, individuals with more mass are likely to exceed the height limit because they will slide faster than those with less mass. Placing jet nozzles in the developed slide prevents the user from exceeding the limit levels. The water requirement for Monarch Butterfly is determined as 200 m^3/h and it will provide a significant advantage in saving water as it will require 30% less water than its competitors in the market. Water consumption was measured by placing a flowmeter where the water slide was actively used (PM 15:00 - 21:00). In addition, water and energy efficiency calculations were made by determining the maximum number of users per hour sliding in two lanes, considering sliding speed, acceleration, and safety times between two slides. Considering that 3.3 m^3 of water was consumed per sliding activity and the maximum number of sliding was 60, it was determined that 200 m^3 of water was consumed per hour.

After the sliding process on the Monarch Butterfly waterslide is completed, users will be positioned in the direction of the evacuation ladder. Since the slide has two lanes, the lanes are separated from each other with separators placed in the middle of the body to prevent the transition from lane to lane, and the clean area is protected with propulsion systems. Monarch Butterfly Waterslide was designed to be unique in the industry with its design, sliding style, competitive structure, water technique, and steel construction.

4. Conclusions

The biggest contribution of the developed Monarch Butterfly slide to national development is that it will require 30% less water than its competitors and provides a significant advantage in water saving. This slide is aimed to save water and increase productivity in businesses by consuming less water and providing more entertainment to more people. Energy costs are high in slides produced with traditional technologies. Therefore, energy management needs to be implemented in the system. Thanks to the applied energy management, efficiency increases and approximately 50% energy savings are achieved. It should not be forgotten that the Monarch Butterfly slide, beyond providing energy savings, will also represent an environmentally friendly and sustainable environmental

approach. While it is known that traditional slides cause high energy costs, the aim is to minimize the negative effects on the environment thanks to the new energy management approach. In this way, water resources will not only be used economically but also serve the purpose of long-term environmental protection.

The developed slide can also be considered as an example of transformation in the sector. Innovative approaches and sustainability-focused product development can also inspire other businesses. In addition, issues such as water saving, and energy efficiency have an important place in terms of social awareness today. In this respect, it will reach large masses and contribute to increasing water-saving awareness. Safety is of great importance in the design and operation of water parks. Along with the enjoyable properties of water, maintaining balance and minimizing risks should not be ignored. In addition, sustainable use of water resources and minimization of environmental impacts is critical for the future of such recreational areas. Users entering the 43% inclined butterfly body will reach a speed of 16 m/sec while performing the vertical oscillation movement and will move with an acceleration of 0.5m/sec2 on the horizontal axis during this oscillation. Approximately 70% water and energy savings were achieved when there was no movement on the slide body.

When the practices in the sector are examined, the amount of water used in water parks may vary depending on the size of the park, the circulation system of the water, and the type of water games in the park. Water parks often feature large pools, slides, wave pools and other water-themed entertainment areas. With the developed software and automation, energy and water savings were achieved and the consumption rate was reduced. As a result, the advantages that this study will bring to national development, such as water saving and energy efficiency, will have a positive impact not only on the profitability of enterprises, but also on environmental sustainability.

Acknowledgments

We would like to thank Polgün Waterparks & Attractions company for their support to this study.

Research Ethics

Ethical approval not required.

Author Contributions

The author(s) accept full responsibility for the content of this article and have approved its submission.

Competing Interests

The author(s) declare that there are no competing interests.

Research Funding

Not reported.

Data Availability

Not applicable.

References

[1] Jain, A., Varshney, A. K., & Joshi, U. C. (2001). Short-term water demand forecast modeling at IIT Kanpur using artificial neural networks. *Water Resources Management*, *15*(5), 299–321. https://doi.org/10.1023/A:1014415503473

[2] Banihabib, E. M., & Pezhman, M. M. (2019). Extended linear and non-linear auto-regressive models for forecasting the urban water consumption of a fast-growing city in an arid region. *Sustainable Cities and Society*, *48*, 101585. https://doi.org/10.1016/j.scs.2019.101585

[3] United Nations. (2015). Transforming our world: The 2030 agenda for sustainable development. Resolution adopted by the General Assembly on 25 September 2015.

[4] Arı, A. (2021). Yenilenebilir enerji, turizm, CO2 ve GSYH ilişkisinin Türkiye için analizi. *Journal of Academic Approaches*, *12*(2). https://doi.org/10.54688/ayd.880406

[5] Chu, N., Wang, D., Wang, H., Liang, Q., Chang, J., Gao, Y., Jiang, Y., & Zeng, R. J. (2023). Flow-electrode microbial electrosynthesis for increasing production rates and lowering energy consumption. *Engineering*, *25*, 157–167. https://doi.org/10.1016/j.eng.2022.10.016

[6] Ozturk, H. K., Ozturk, H. M., & Dombaycı, A. (2018). Energy consumption and energy saving opportunities in tourism sector. *Güncel Turizm Araştırmaları Dergisi*, 2(1), 17-28. https://doi.org/10.22392/guntad.419604

[7] Brezet, H. (1997). Dynamics in ecodesign practice. *Industrial Environment*, *20*, 21-24.

[8] UNEP. (2006).

[9] Bhamra, T., & Lofthouse, V. (2007). Design of sustainability: A practical approach. Gower Publishing, Ltd.

[10] Kloepffer, W. (2008). Life cycle sustainability assessment of products. *International Journal of Life Cycle Assessment*, *13*(1), 89-95. https://doi.org/10.1065/lca2008.02.376

[11] Mudavanhu, S., Blignaut, J., Stegmann, N., Barnes, G., & Prinsloo Tuckett, A. (2017). The economic value of ecosystem goods and services: The case of Mogale's Gate Biodiversity Centre, South Africa. *Ecosystem Services*, *26*, 127–136. https://doi.org/10.1016/j.ecoser.2017.06.005

[12] Yin, R., Liu, T., Yao, S., & Zhao, M. (2013). Designing and implementing payments for ecosystem services programs: Lessons learned from China's cropland restoration experience. *Forest Policy and Economics*, *35*(1), 66–72.

[13] Doğan, M. (2023). Sürdürülebilirlik: Su ve suyun önemi. *Eurasian Journal of Research in Social and Economics (EJRSE)*, *10*(1), 176-192.

[14] Yalcınkaya, P., Atay, L., & Karakas, E. (2018). Smart tourism applications Gastroia. *Journal of Gastronomy and Travel Research*, 2(2), 34-52.

[15] Andrew, M. B. (2023). Development of an open-source soil

water potential management system for horticultural applications. *HardwareX*, *15*, e00458. https://doi.org/10.1016/j.ohx.2022.e00458

[16] Irfan, M., Ullah, S., Razzaq, A., Cai, J., & Adebayo, T. S. (2023). Unleashing the dynamic impact of tourism industry on energy consumption, economic output, and environmental quality in China: A way forward towards environmental sustainability. *Journal of Cleaner Production*, *387*, 135778. https://doi.org/10.1016/j.jclepro.2023.135778

[17] Özgür, D., & Meltem, C. (2019). Analysis of hotel services by their symmetric and asymmetric effects on overall customer satisfaction: A comparison of market segments. *International Journal of Hospitality Management*, *81*, 83-93. https://doi.org/10.1016/j.ijhm.2019.03.006

[18] Yitong, C., Chang, Q., Yanan, Y., Xiaoxin, C., Xiang, Z., & Rong, C. (2023). Evolution and health risk of indicator microorganisms in landscape water replenished by reclaimed water. *Journal of Environmental Sciences*. https://doi.org/10.1016/j.jes.2023.06.039

[19] Milman, A., Okumus, F., & Dickson, D. (2010). The contribution of theme parks and attractions to the social and economic sustainability of destinations. *Worldwide Hospitality and Tourism Themes*, 2, 338-345. https://doi.org/10.1108/17554211011052245

[20] RTM process [Internet]; [cited 2023 Dec 25]. Available from: http://www.kossecomposite.com/muhendislik.html

EUROPEAN MECHANICAL SCIENCE

Research Article

e-ISSN: 2587-1110

Modeling and simulation of earth coverage of a low earth orbit (LEO) satellite

Murat Bakirci[1*]

[1]Faculty of Aeronautics and Astronautics, Tarsus University, Mersin 33400, Turkiye

Orcid: M. Bakirci (0000-0003-2092-1168)

Abstract: Efficient management of operations in near space, just beyond the Earth's atmosphere, relies on the precise control of satellites positioned relatively close to our planet. Satellite systems, serving critical functions in telecommunications, observation, exploration, and more, have demonstrated their prowess as a transformative technology, consistently delivering high-precision data over numerous years. Among satellite systems, Low Earth Orbit (LEO) technology is gaining prominence due to its advantages, including lower power requirements for transmission, reduced propagation delays, and heightened coverage for polar regions. Achieving optimal efficiency from LEO satellites necessitates a thorough understanding of their fundamental orbital parameters and precise control over them. This study explores the orbital analysis and Earth coverage considerations of LEO satellites, scrutinizing orbital parameters in detail to compute coverage areas across various scenarios. Through this investigation, the potential benefits of data exchange with ground stations facilitated by LEO satellites are explored. In addition, the implications are discussed regarding the adjustment of data exchange topologies according to geographical locations and country borders.

Keywords: LEO satellite, earth coverage, orbital parameters, ground track.

1. Intorduction

Satellite systems are one of the key components of space research and communication technologies due to the many advantages they provide. The most common usage areas of this technology can be listed as communication [1-4], observation [5], warfare applications [6], and positioning applications at various scales [7]. The importance of low-altitude satellites, which are used for purposes such as observation and exploration on Earth, is increasing over time. Satellites known as Low-Earth orbit (LEO) are reliable systems capable of meeting such requirements with sufficient accuracy [8-13]. In addition to all the other benefits, they have all the necessary features for positioning when GNSS satellites cannot be used effectively [9]. Since they are much closer to the Earth than GNSS satellites, the signals received from these satellites are much stronger [8]. Moreover, the orbital information of these satellites was made available to the public by the North American Aerospace Defense Command (NORAD), which greatly facilitated the work of the relevant researchers [14].

LEO satellites have found a myriad of applications across various domains, owing to their proximity to Earth and the advantages they offer in terms of data transmission, coverage, and responsiveness. One prominent application lies in telecommunications, where LEO satellites serve as vital components in global communication networks [15, 16]. These satellites facilitate voice and data communication services, including mobile phone calls, internet connectivity, and multimedia streaming. Due to their relatively low altitude, LEO satellites enable low-latency communication, making them particularly suitable for real-time applications such as voice calls and video conferencing [17]. Moreover, LEO satellite constellations, characterized by multiple satellites orbiting the Earth in close proximity, enhance network reliability and coverage, ensuring seamless connectivity even in remote or underserved regions [18]. Beyond traditional telecommunications, LEO satellites also play crucial roles in emergency communication systems, providing essential communication links during natural disasters, humanitarian crises, and remote rescue operations [19, 20]. Their rapid deployment capabilities and wide coverage areas make LEO satellites indispensable tools for emergency response and disaster management efforts worldwide.

*Corresponding author:
Email: muratbakirci@tarsus.edu.tr

Cite this article as:
Bakirci, M. (2024). Modeling and simulation of earth coverage of a low earth orbit (LEO) satellite. *European Mechanical Science*, *8*(2): 85-92. https://doi.org/10.26701/ems.1466031

History dates:
Received: 06.04.2024, *Revision Request*: 06.05.2024, *Last Revision Received*: 09.05.2024, *Accepted*: 23.05.2024

Another significant application of LEO satellites is in Earth observation and environmental monitoring [21]. Equipped with advanced sensors and imaging technologies, LEO satellites capture high-resolution imagery of the Earth's surface, atmosphere, and oceans [22, 23]. These satellites facilitate a wide range of applications, including weather forecasting, climate monitoring, disaster management, agriculture, and urban planning [24, 25]. By continuously monitoring environmental parameters such as weather patterns, sea surface temperatures, vegetation health, and land use changes, LEO satellites provide valuable data for scientific research, resource management, and policy-making. Furthermore, LEO satellite imagery aids in the assessment and mitigation of natural disasters such as hurricanes, floods, wildfires, and earthquakes by enabling early detection, rapid response, and post-event damage assessment [26]. The real-time monitoring capabilities of LEO satellites also contribute to environmental conservation efforts by tracking deforestation, pollution, and biodiversity loss, facilitating informed decision-making to address pressing environmental challenges [27].

Satellite systems, along with other unmanned systems, maintain continuous communication with ground stations, ensuring they are under constant supervision, regardless of whether they fulfill their duties proficiently or encounter issues. In this context, while updates are transmitted by ground stations at certain times, the received telemetry information is also subject to control [28-30]. For this to happen, the satellite must enter the line of sight of the ground station. However, even this alone is not enough for data exchange to be efficient. The quality of data exchange may also depend on antenna gain, network relay speed, and even geographical conditions [31-33]. LEO satellites, which are closer to the Earth than other satellite systems, move relatively faster in their orbits and therefore communication can be established from the ground stations for limited times. On the other hand, the duration of data exchange is primarily dependent on the orbital parameters and the geographical location of the ground control stations on Earth [34, 35]. Especially in critical Earth-observation missions, it is necessary to know the orbit information and coverage area of the satellite with high accuracy [36, 37]. This is an essential requirement for many important applications. In this study, the orbital characteristics of LEO satellites were investigated by considering the basic Kepler parameters and focused on the coverage areas throughout their orbits. Thus, a framework has been tried to be drawn about how and to what extent they can communicate with ground stations.

2. Methodology

In the numerical study, the two-line element set provided by the NORAD system are used as initial values. After the first computations are made with these initial values, the iterative process starts, and the necessary computations for each time step of the satellite are made as follows: First, using NORAD's data, the period of the satellite orbit, T, is computed as mean motion $T = 86400/\text{mean motion}$. Then, using this period value, the semi-major axis is computed as follows.

$$a = \sqrt[3]{\left(\frac{T}{2\pi}\right)^2 \Upsilon} \tag{1}$$

where Υ is the standard gravitational parameter and has an approximate value of $3.986004418 \times 10^{14} m^3 s^{-2}$ for Earth. With the eccentricity, e, and mean anomaly, M, values from NORAD, the eccentric anomaly, E, is computed as follows:

$$M = E - e \sin E \tag{2}$$

Using the same eccentricity and mean anomaly values, the true anomaly value, θ, can also be computed as follows:

$$\theta = 2 \tan^{-1}\left(\sqrt{\frac{1+e}{1-e}} \tan\frac{E}{2}\right) \tag{3}$$

The position vector, $\hat{\mathbf{p}}$, relative to the center of Earth is then computed as follows:

$$\hat{\mathbf{p}} = [p\cos\theta \quad p\sin\theta \quad 0]^T \tag{4}$$

In the computation of $\hat{\mathbf{p}}$, inclination, i, right ascension, Ω, and argument of periapsis, ω, values provided by NORAD are also used. The magnitude of the position vector given above can be expressed as follows:

$$p = \frac{a(1-e^2)}{1+e\cos\theta} \tag{5}$$

The following set of transformation equations is used to transform the position vector from the perifocal coordinate system to the equatorial coordinate system.

$$\xi_i = \cos\Omega\cos\omega - \sin\Omega\cos i\sin\omega \tag{6a}$$

$$\xi_j = \sin\Omega\cos\omega + \cos\Omega\cos i\sin\omega \tag{6b}$$

$$\xi_k = \sin i\sin\omega \tag{6c}$$

$$\zeta_i = -\cos\Omega\sin\omega - \sin\Omega\cos i\cos\omega \tag{7a}$$

$$\zeta_j = -\sin\Omega\sin\omega + \cos\Omega\cos i\cos\omega \tag{7b}$$

$$\zeta_k = \sin i\cos\omega \tag{7c}$$

$$\eta_i = \sin i\sin\Omega \tag{8a}$$

$$\eta_j = -\sin i\cos\Omega \tag{8b}$$

$$\eta_k = \cos i \tag{8c}$$

Each satellite will have different Keplerian element values and thus different altitudes and orbital trajectories. Altitude is a critical parameter that directly determines the orbital speed and coverage area. As the altitude increases, the width of the swath, which is a circular area, increases. However, considering the two-dimensional model, this coverage area, which is almost a full circle around the equator, will deviate from a circle and take on

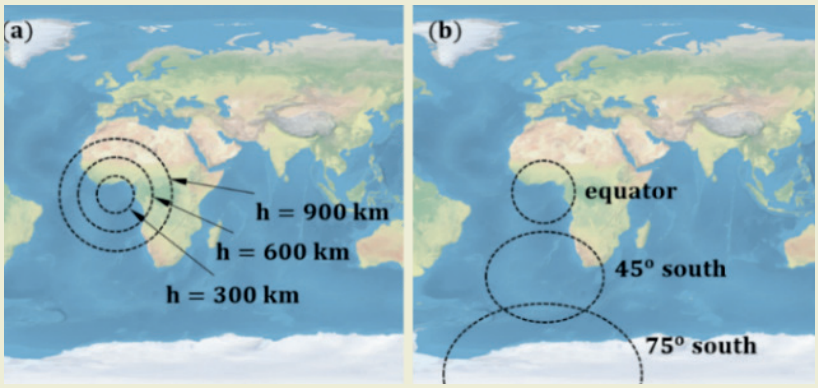

Figure 1. Variation of satellite coverage area with altitude (a) and latitude (b).

a different shape near the poles. Fig. 1a shows the variation of coverage area with satellite altitude. As shown in the figure, an increase of about 800% in the coverage area occurs when the altitude increases from 300 km to 900 km. Fig. 1b shows the different coverage areas of a 500 km altitude LEO satellite at different points on the Earth.

Some of the key orbital parameters of a LEO satellite in Earth orbit are given in Fig. 2. In the figure, r is the radius of the Earth, h is the altitude of the satellite, GS is the location of the ground station, s is the subsatellite point, σ is the satellite's coverage radius, τ is the projection of the satellite coverage angle relative to the Earth's center (C), δ is the angular distance between the ground station and the subsatellite point, ε is the elevation angle, and γ is the azimuth angle.

Based on the figure, the coverage radius of the satellite is determined as follows:

$$\sin\sigma = r/r + h \tag{9}$$

It must be noted that the angular relationship between σ and τ is $\sigma + \tau = 90^o$ as can be deduced from the figure. When the latitude, λ_s, longitude, φ_s, of the subsatellite point and the latitude, λ_{GS}, of the GS are known, the azimuth angle, γ, and the angular distance, δ, between these points are calculated as follows:

$$\cos\delta = \sin\lambda_s \sin\lambda_{GS} + \cos\lambda_s \cos\lambda_{GS} \cos\Delta\lambda \tag{10}$$

$$\cos\gamma = \frac{\sin\lambda_{GS} - \cos\delta\sin\lambda_s}{\sin\delta\cos\lambda_s} \tag{11}$$

where $\Delta\lambda$ is the angular distance between the subsatellite point and the ground station. Depending on whether the GS is east or west from the s, the azimuth angle will take values greater or less than 180 degrees.

Specifying Fig. 2 in more detail, additional parameters can be determined for the orbiting satellite. Fig. 3 shows the angular relationship between the satellite, GS, and subsatellite point s. Using the geometric figure, the angle of inclination of the satellite and the distance between the satellite and the GS can be computed as follows:

$$\tan\nu = \frac{\sin\sigma\sin\delta}{1 - \sin\sigma\cos\delta} \tag{12}$$

and the distance between the satellite and GS is

$$d = r(\sin\delta/\sin\nu) \tag{13}$$

where ν is the nadir angle, the angle between the subsatellite point and the GS, measured from the satellite to the GS. Using the obtained nadir angle, the elevation angle, ε, of the satellite is calculated as follows:

$$\cos\varepsilon = \sin\nu/\sin\sigma \tag{14}$$

When an LEO satellite is within the detection area of the GS, the primary factor that determines the data transfer time between the satellite and the GS is the satellite's inclination. While this time increases at high elevation angles, it decreases dramatically as the elevation decreases;

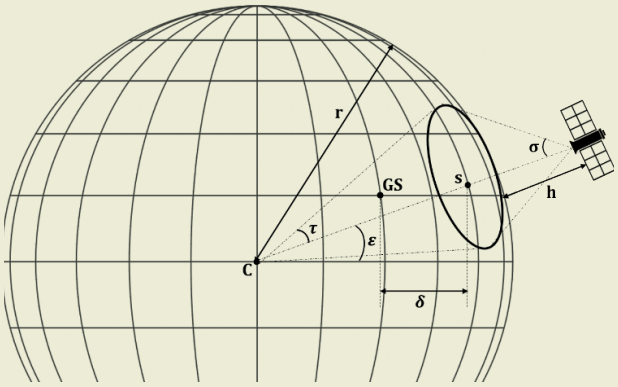

Figure 2. Orbital parameters of the LEO satellite.

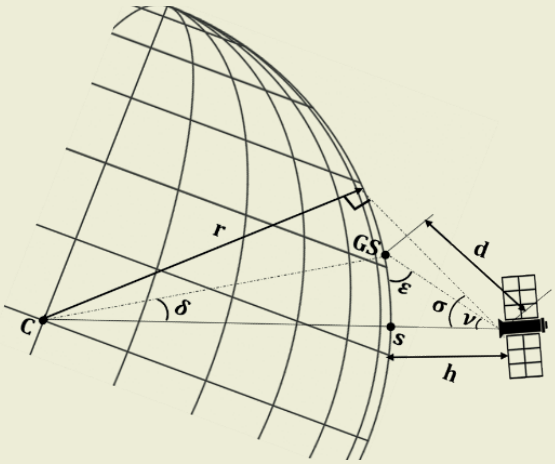

Figure 3. Different perspective of orbital parameters of the LEO satellite.

that is, the data transfer time is a function of the elevation angle. When the satellite is at high elevation angles, the transfer time will be longer, as it will be in view of the GS for a longer period of time. At elevation angles below approximately 5 degrees, communication with the satellite cannot be established due to geographical constraints. The relationship between the elevation angle and the angular distance between the subsatellite point and GS can be expressed as follows.

$$\delta = \cos^{-1}\left(\frac{r}{r+h}\cos\varepsilon\right) - \varepsilon \tag{15}$$

Fig. 4 shows the variation of elevation angle, ε, with angular distance, δ, between the subsatellite point and GS for LEO satellites with different altitudes. As can be seen from the graph, the elevation angle affects the communication time significantly due to the change in the angular distance between the subsatellite point and GS.

3. Results

Simulations were performed using the set of operations described in the previous section, utilizing the NORAD dataset as initial values. Considering that the true anomaly value is a function of time, eccentric anomaly values are computed for each time stamp with true anomaly values calculated using the initial value. This approach allows for obtaining the position of the LEO satellite in time in the equatorial coordinate system.

However, another critical point to consider is the Earth's rotation. So far, computations for the satellite have taken into account only the motion of the satellite. However, since the Earth's rotation will affect all computations, they must be adjusted accordingly. Only through this adjustment can the trajectory of the satellite over the rotating Earth be accurately determined. To achieve this, the position vector obtained in (4) must be corrected, taking into account the angular velocity of the Earth, as follows:

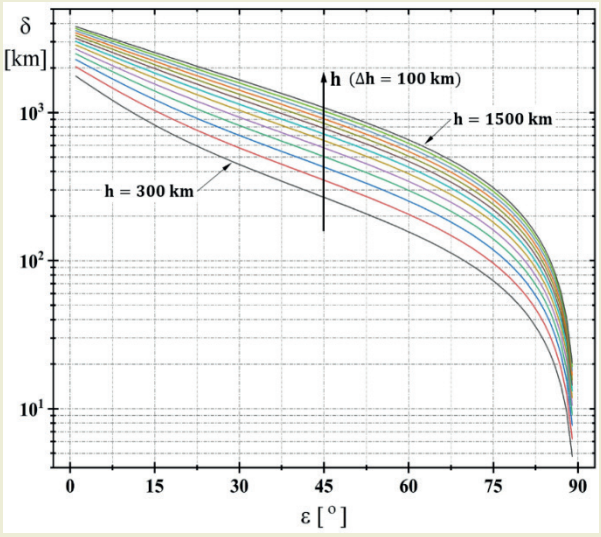

Figure 4. Variation of elevation angle with angular distance between subsatellite point and GS for different altitudes.

$$\hat{\mathbf{p}}_{cor} = R_{e,t} \times [p\cos\theta \quad p\sin\theta \quad 0]^T \tag{16}$$

where $\hat{\mathbf{p}}_{cor}$ indicates corrected position matrix and $R_{e,t}$ is the angular velocity matrix of the Earth and is expressed as

$$R_{e,t} = \begin{bmatrix} \cos(\omega_e t) & \sin(\omega_e t) & 0 \\ -\sin(\omega_e t) & \cos(\omega_e t) & 0 \\ 0 & 0 & 1 \end{bmatrix} \tag{17}$$

where ω_e is the angular velocity of the Earth. The subsatellite point of the LEO satellite can be easily found by subtracting the Earth radius from the altitude of the satellite.

Thus, the correct position vector, $\hat{\mathbf{p}}_{cor}$, of the considered satellite is obtained. From here, the actual coordinates of the subsatellite point on Earth are computed as follows

$$\lambda_s = \sin^{-1}(p_z/r) \tag{18}$$

$$\varphi_s = \cos^{-1}\left(\frac{p_x}{r\cos\lambda_s}\right) \tag{19}$$

where p_x and are the x and z components of the corrected position vector, $\hat{\mathbf{p}}_{cor}$, respectively. Now that the correct coordinates of the satellite have been obtained, it remains to compute whether or not the GS is within the satellite's coverage area. Since the coordinates of both the subsatellite point and GS are known, and the distance between inter-latitude is also known, using (10), the distance between the subsatellite point and GS is determined, and by normalizing the coverage area with the distance between inter-latitudes, the maximum distance to be covered by the satellite is computed as follows.

$$\vartheta = 2\tau r \tag{20}$$

Fig. 5 shows the ground track map illustrating a full orbit of an LEO satellite around the Earth. The parameters used in this orbital simulation are as follows: eccentricity is 0.2, semimajor axis is 8000 km, true anomaly is 70 degrees, inclination is 70 degrees, argument of perigee is also 70 degrees, and right ascension is 120 degrees. Using these parameters, the orbital characteristics were computed as follows: the initial radius is 7188 km, initial velocity is 7.815 km s^{-1}, angular momentum is 55329 km^2 s^{-1}, mean anomaly is 0.866 rad, eccentric anomaly is 1.039 rad, perigee radius is 6400 km, flight path angle is 0.174 rad, and energy is -24.913 km^2 s^{-2}.

In Fig. 6, the velocity and position vector components corresponding to this orbital motion are provided. In both graphs, the variations of the velocity vector and position vector with respect to true anomaly are given. Based on the velocity-true anomaly graph, the average velocity of the satellite during its orbital motion is 7.326 km s^{-1}, and their minimum and maximum velocities are 5.777 km s^{-1} and 8.714 km s^{-1}, respectively. Fig. 7 shows the variation of the same velocity and position vector components with respect to time.

In Fig. 8a, the orbital motion of the satellite around the

Earth is expressed in 3D. Similarly, the velocity variation along the orbital motion is given in Fig. 8b. Note that in this graph, different vector lengths correspond to different magnitudes of velocity.

Fig. 9a and Fig. 9b show a ground track map illustrating 5 and 43 orbits of an LEO satellite around the Earth, respectively. For both simulations, all orbital parameters are the same except their periods. The orbital motion period in Fig. 9b is five times shorter, which provides a general framework for most LEO satellites, considering their high-speed orbital motion.

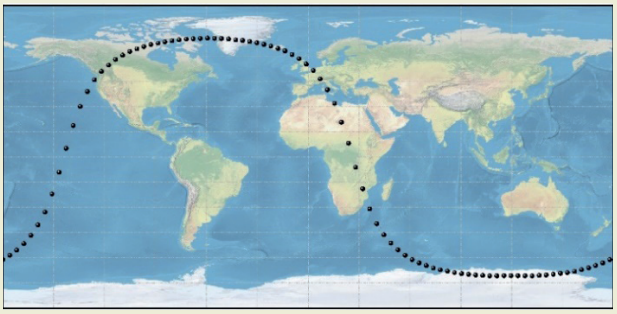

Figure 5. Ground track for the LEO satellite.

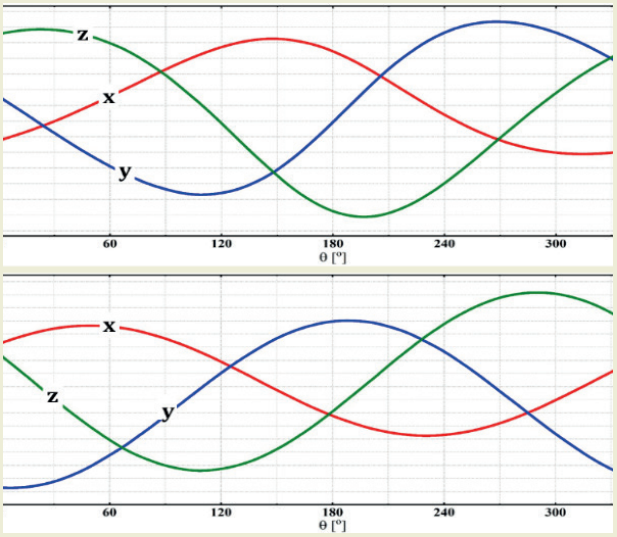

Figure 6. Variation of position and velocity vector components with respect to true anomaly.

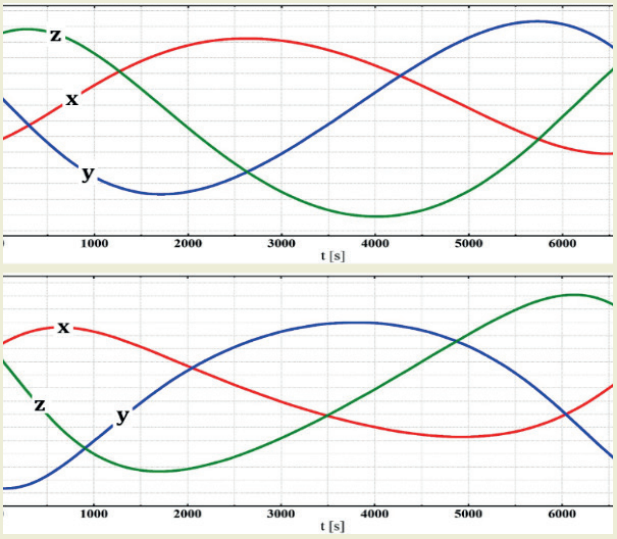

Figure 7. Variation of position and velocity vector components with respect to time.

Table 1 shows the numerical values corresponding to the azimuth and elevation angle diagram obtained from the numerical study. In this simulation, the GS was assumed to be located at the point on the Earth corresponding to 0 latitude and longitude. On the other hand, the LEO satellite corresponding to Fig. 9b, was assumed to have a 70-degree inclination, at an altitude of 750 km, and to make 43 complete orbits around the Earth each day.

In the table, the position of the GS is expressed as the center, that is, the point where the zero values intersect. At this point, the elevation angle is maximum, that is, 90 degrees. As you go from the center of the table, the elevation angle decreases. When horizontal angle values are considered as x components and vertical angle values as y components, the azimuth value is 0 at the intersection of 0 and [90,80), and is 90 at the intersection of (80,90] and 0, and is 180 at the intersection of 0 and (-80,90], and is 270, at the intersection of [-90,80) and 0. All cells

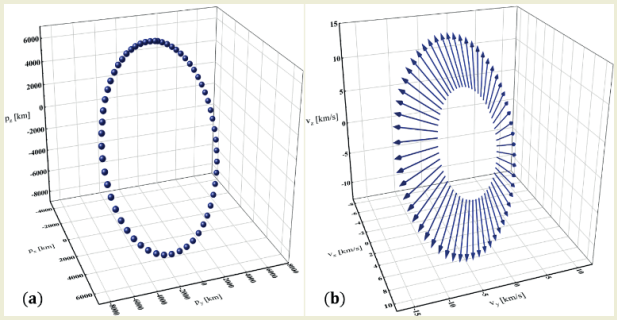

Figure 8. Three dimensional illustration of the LEO satellite's orbital motion around the Earth (a), and velocity variation along the orbital motion (b).

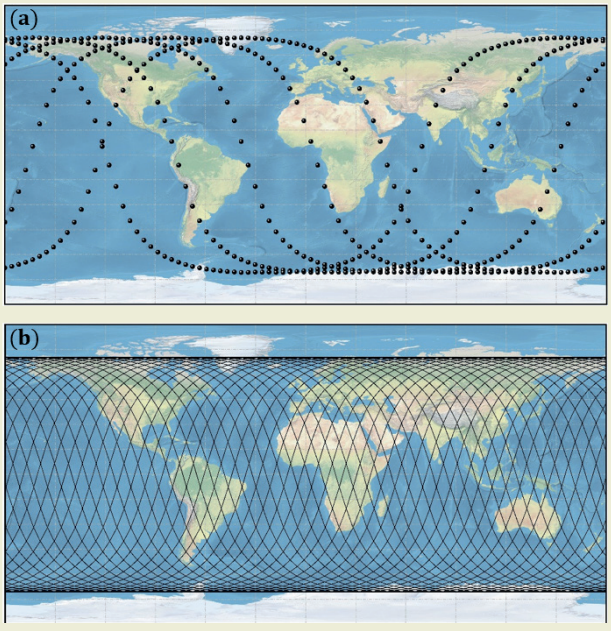

Figure 9. Ground track of 5 (a) and 43 (b) orbits of the LEO satellite.

https://doi.org/10.26701/ems.1460031

Table 1. Satellite and GS communication instants.

	[°]																		
[°]	[-90, -80)	[-80, -70)	[-70, -60)	[-60, -50)	[-50, -40)	[-40, -30)	[-30, -20)	[-20, -10)	[-10, 0)	0	(0, 10]	(10, 20]	(20, 30]	(30, 40]	(40, 50]	(50, 60]	(60, 70]	(70, 80]	(80, 90]
[90, 80)	-	-	-	-	-	-	1,2,6	2	4,11		9	5,9	-	8,12	-	-	-	-	-
[80, 70)	-	-	-	3	1,5	1,2,6	2,4	4	11		11	5,9	9	12	8,10	-	-	-	-
[70, 60)	-	-	3	1,3,5	1,2,5	2,4,6	4	-	-		11	11,13	9	9,12	12	8,10	-	-	-
[60, 50)	-	-	1,3	1,2,5	2	4,6	-	-	-		-	11,13	-	9	9,12	8,10	10	7	-
[50, 40)	-	1,3	1,2,3	2,5	4	4,6	-	-	-		-	11,13	11	-	9,12	8,9	8,10	7	-
[40, 30)	-	1,3	2,5	-	4,6	-	-	-	-		-	13	11	-	12	9,12	8,10	7	-
[30, 20)	1	1,2,3	2,5	4	6	-	-	-	-		-	13	11	11	-	9,12	10	8	7
[20, 10)	1	2,3	5	4	6	-	-	-	-		13	-	-	11	-	12	9,10	8	7
[10, 0)	1	2,3	5	4	6	-	-	-	-		13	-	-	11	-	12	9	8,10	7
0																			
(0, -10]	1	2,3	4,5	4	-	6	-	-	-		13	-	-	11	11	12	9	8,10	7
(-10, -20]	1	2,3	4,5	-	-	6	-	-	-		13	-	-	-	11,12	12	9,10	-	7,8
(-20, -30]	1	2,3	4,5	-	-	6	-	-	13		13	-	-	-	11,12	-	9,10	-	7,8
(-30, -40]	-	2,3	3,4	4,5	-	6	-	-	13		-	-	-	-	11,12	-	9,10	7,8	7
(-40, -50]	-	2	3	4,5	-	-	6	-	13		-	-	-	12	11,12	10	9,10	7,8	-
(-50, -60]	-	2	3	4,5	5	-	6	-	13		-	-	-	12	11	10	9	-	-
(-60, -70]	-	-	3	3,4	5	5	-	6,13	13		-	-	12	12	10,11	9,10	9	-	-
(-70, -80]	-	-	-	3	-	5	-	6,13	6		-	12	12	10,11	10	-	-	-	-
(-80, -90]	-	-	-	-	-	-	5	13	6		6,12	12	-	10,11	-	-	-	-	-

with numerical values indicate communication times. In only 15 of the 43 full orbits made by the LEO satellite, the GS has entered the satellite's coverage area. As only 13 of them have the minimum elevation angle possible to communicate, they are listed in the table. In the other two cases, it will not be possible to establish a connection due to geographical constraints.

4. Conclusion

Despite having all the advantages, it is quite critical to know basic orbital parameters with high accuracy and to control them precisely in order to get the maximum efficiency from LEO satellites. For that reason, their ground tracks must be obtained with high accuracy, and communication instants with ground stations must be accurately calculated. The orbital analysis of a LEO satellite and the Earth coverage problem was investigated in this study. By computing the Keplerian parameters of the satellite, detailed orbital analysis was performed, and the orbital motion was determined for different inputs. By computing the position and velocity vectors, the changes in all phases of the trajectory were examined. Moreover, the coverage area, which indirectly depends on time, was obtained during its entire orbital motion, and it was computed when it exchanged data with the ground station. It was determined that a LEO satellite with specific orbital parameters is able to communicate in only 13 of the 43 orbits made in total. Satellite ground tracks have been analyzed in detail, and insight was gained about what topology should be planned for maximizing the communication time. It was concluded that a single LEO satellite can be used quite efficiently by establishing the optimum number of ground station networks at the proper locations of the Earth. Since Turkey, the area of interest in this study, has an approximately rectangular geographical shape, it will be sufficient to establish two ground stations, one in the east and another in the west, along the central axis of the territory.

Research Ethics

Ethical approval not required.

Author Contributions

The author(s) accept full responsibility for the content of this article and have approved its submission.

Competing Interests

The author(s) declare that there are no competing interests.

Research Funding

Not reported.

Data Availability

Not applicable.

Rererences

[1] Khalife, J.J., Kassas, Z.M. (2019). Receiver design for Doppler positioning with LEO satellites. *ICASSP 2019 - 2019 IEEE International Conference on Acoustics, Speech and Signal Processing*, 5506-5510. https://doi.org/10.1109/ICASSP.2019.8682554

[2] Bakirci, M., Cetin, M. (2022). Utilization of a vehicle's on-board diagnostics to reduce GPS-sourced positioning error. *2022 Innovations in Intelligent Systems and Applications Conference (ASYU)*, Antalya, Turkey, 1-4. https://doi.org/10.1109/ASYU52992.2022.9833873

[3] Cluzel, S., Franck, L., Radzik, J., Cazalens, S., Dervin, M., Baudoin, C. (2018). 3GPP NB-IOT coverage extension using LEO satellites. *2018 IEEE 87th Vehicular Technology Conference (VTC Spring)*, 1-5. https://doi.org/10.1109/VTCSpring.2018.8417874

[4] Su, Y., Liu, Y., Zhou, Y., Yuan, J., Cao, H., Shi, J. (2019). Broadband LEO satellite communications: architectures and key technologies. *IEEE Wireless Communications*, 26(2), 55-61. https://doi.org/10.1109/MWC.2019.8684206

[5] Crisp, N.H., Roberts, P.C.E., Livadiotti, S., Oiko, V.T.A., Edmondson, S., Haigh, S.J. (2020). The benefits of very low earth orbit for earth observation missions. *Progress in Aerospace Sciences*, 117, 1-18. https://doi.org/10.1016/j.paerosci.2020.100619

[6] Routray, S.K., Javali, A., Sahoo, A., Sharmila, K.P., Anand, S. (2020). Military applications of satellite based IoT. *2020 Third International Conference on Smart Systems and Inventive Technology (ICSSIT)*, 122-127. https://doi.org/10.1109/ICSSIT48917.2020.9214165

[7] Li, B., Ge, H., Ge, M., Nie, L., Shen, Y., Schuh, H. (2019). LEO enhanced global navigation satellite system (LeGNSS) for real-time precise positioning services. *Advances in Space Research*, 63(1), 73-93. https://doi.org/10.1016/j.asr.2018.08.026

[8] Khalife, J., Neinavaie, M., Kassas, Z.M. (2020). Navigation with differential carrier phase measurements from megaconstellation LEO satellites. *2020 IEEE/ION Position, Location and Navigation Symposium (PLANS)*, Portland, Oregon, 1393-1404. https://doi.org/10.1109/PLANS46316.2020.9110165

[9] Morales, J., Khalife, J., Kassas, Z.M. (2019). Simultaneous tracking of Orbcomm LEO satellites and inertial navigation system aiding using Doppler measurements. *2019 IEEE 89th Vehicular Technology Conference (VTC2019-Spring)*, 1-6. https://doi.org/10.1109/VTCSpring.2019.8746340

[10] Reid, T., Neish, A., Walter, T., Enge, P. (2018). Broadband LEO constellations for navigation. *NAVIGATION, Journal of the Institute of Navigation*, 65(2), 205-220. https://doi.org/10.1002/navi.249

[11] Lawrence, D., Cobb, H., Gutt, G., O'Connor, M., Reid, T., Walter, T. (2017). Navigation from LEO: current capability and future promise. *GPS World Magazine*, 28(7), 42-48.

[12] Chen, X., Wang, M., Zhang, L. (2016). Analysis on the performance bound of Doppler positioning using one LEO satellite. *IEEE Vehicular Technology Conference (VTC-Fall)*, 1-5. https://doi.org/10.1109/VTCFall.2016.7881273

[13] Kozhaya, S.E., Haidar-Ahmad, J.A., Abdallah, A.A., Kassas, Z.M., Saab, S.M. (2021). Comparison of neural network architectures for simultaneous tracking and navigation with LEO satellites. *34th International Technical Meeting of the Satellite Division of the Institute of Navigation (ION GNSS+ 2021)*, St. Louis, Missouri, 2507-2520. https://doi.org/10.33012/2021.17811

[14] North American Aerospace Defense Command (NORAD). "Two-line element sets." celestrak.com. https://www.celestrak.com/NORAD/elements/ (accessed Jan. 3, 2024).

[15] Geng, S., Liu, S., Fang, Z., Gao, S. (2020). An optimal delay routing algorithm considering delay variation in the LEO satellite communication network. *Computer Networks*, 173, 107166. https://doi.org/10.1016/j.comnet.2020.107166

[16] Ge, H., Li, B., Nie, L., Ge, M., Schuh, H. (2020). LEO constellation optimization for LEO enhanced global navigation satellite system (LeGNSS). *Advances in Space Research*, 66(3), 520-532. https://doi.org/10.1016/j.asr.2019.04.008

[17] Sun, X., Han, C., Chen, P. (2017). Precise real-time navigation of LEO satellites using a single-frequency GPS receiver and ultra-rapid ephemerides. *Aerospace Science and Technology*, 67, 228-236. https://doi.org/10.1016/j.ast.2017.03.008

[18] Lin, X., Chen, Y., Xue, J., Zhang, B., He, L., Chen, Y. (2024). Large-volume LEO satellite imaging data networked transmission scheduling problem: Model and algorithm. *Expert Systems with Applications*, 249(B), 123649. https://doi.org/10.1016/j.eswa.2023.123649

[19] Denis, G., de Boissezon, H., Hosford, S., Pasco, X., Montfort, B., Ranera, F. (2016). The evolution of Earth Observation satellites in Europe and its impact on the performance of emergency response services. *Acta Astronautica*, 127, 619-633. https://doi.org/10.1016/j.actaastro.2016.06.019

[20] Lourenço, R.B.R., Figueiredo, G.B., Tornatore, M., Mukherjee, B. (2019). Data evacuation from data centers in disaster-affected regions through software-defined satellite networks. *Computer Networks*, 148, 88-100. https://doi.org/10.1016/j.comnet.2018.11.022

[21] Pardini, C., Anselmo, L. (2020). Environmental sustainability of large satellite constellations in low earth orbit. *Acta Astronautica*, 170, 27-36. https://doi.org/10.1016/j.actaastro.2020.01.014

[22] Bakirci, M., Bayraktar, I. (2024). Transforming aircraft detection through LEO satellite imagery and YOLOv9 for improved aviation safety. *2024 26th International Conference on Digital Signal Processing and its Applications (DSPA)*, Moscow, Russian Federation, 1-6. https://doi.org/10.1109/DSPA.2024.9832371

[23] Bakirci, M., Bayraktar, I. (2024). Boosting aircraft monitoring and security through ground surveillance optimization with YOLOv9. *2024 12th International Symposium on Digital Forensics and Security (ISDFS)*, San Antonio, TX, USA, 1-6. https://doi.org/10.1109/ISDFS.2024.9832372

[24] Nwankwo, V.U.J., Chakrabarti, S.K. (2018). Effects of space weather on the ionosphere and LEO satellites' orbital trajectory in equatorial, low and middle latitude. *Advances in Space Research*, 61(7), 1880-1889. https://doi.org/10.1016/j.asr.2017.10.022

[25] Lele, N., Nigam, R., Bhattacharya, B.K. (2021). New findings on impact of COVID lockdown over terrestrial ecosystems from LEO-GEO satellites. *Remote Sensing Applications: Society and Environment*, 22, 100476. https://doi.org/10.1016/j.rsase.2021.100476

[26] Maiti, M., & Kayal, P. (2024). Exploring innovative techniques for damage control during natural disasters. *Journal of Safety Science and Resilience*, 5(2), 147-155. https://doi.org/10.1016/j.jssr.2024.02.005

[27] Numbere, A. O. (2022). Application of GIS and remote sensing towards forest resource management in mangrove forest of Niger Delta. *Natural Resources Conservation and Advances for Sustainability*, 433-459. https://doi.org/10.1016/j.nrsca.2022.05.015

[28] Salcedo, D. A., Ciafardini, J. P., & Bava, J. A. (2020). Antenna for telemetry data relay communications in LEO satellites and inmarsat-F4 constellation. In *2020 IEEE Congreso Bienal de Argentina (ARGENCON)* (pp. 1-6). IEEE. https://doi.org/10.1109/ARGENCON49523.2020.9505352

[29] Zhan, Y., Wan, P., Jiang, C., Pan, X., Chen, X., & Guo, S. (2020). Challenges and solutions for the satellite tracking, telemetry, and command system. *IEEE Wireless Communications*, *27*(6), 12-18. https://doi.org/10.1109/MWC.2020.9265056

[30] Stock, G., Fraire, J. A., Mömke, T., Hermanns, H., Babayev, F., & Cruz, E. (2020). Managing fleets of LEO satellites: Nonlinear, optimal, efficient, scalable, usable, and robust. *IEEE Transactions on Computer-Aided Design of Integrated Circuits and Systems*, *39*(11), 3762-3773. https://doi.org/10.1109/TCAD.2020.3021567

[31] Done, A., Lesanu, C., Căilean, A., Graur, A., & Dimian, M. (2017). Implementation of an on-line remote control ground station for LEO satellites. In *2017 21st International Conference on System Theory, Control and Computing (ICSTCC)* (pp. 855-859). IEEE. https://doi.org/10.1109/ICSTCC.2017.8107123

[32] Xia, D., Zheng, X., Duan, P., Wang, C., Liu, L., & Ma, H. (2019). Ground-station based software-defined LEO satellite networks. In *2019 IEEE 25th International Conference on Parallel and Distributed Systems (ICPADS)* (pp. 687-694). IEEE. https://doi.org/10.1109/ICPADS47876.2019.00099

[33] Done, A., Căilean, A., Leşanu, C., Dimian, M., & Graur, A. (2017). Considerations on ground station antennas used for communication with LEO satellites. In *2017 International Symposium on Signals, Circuits and Systems (ISSCS)* (pp. 1-4). IEEE. https://doi.org/10.1109/ISSCS.2017.8034928

[34] Done, A., Căilean, A., Leşanu, C., Dimian, M., & Graur, A. (2017). Design and implementation of a satellite communication ground station. In *2017 International Symposium on Signals, Circuits and Systems (ISSCS)* (pp. 71-75). IEEE. https://doi.org/10.1109/ISSCS.2017.8034929

[35] Zeng, T., Sui, L., Jia, X., Lv, Z., Ji, G., & Dai, Q. (2019). Validation of enhanced orbit determination for GPS satellites with LEO GPS data considering multi ground station networks. *Advances in Space Research*, *63*(9), 2938-2951. https://doi.org/10.1016/j.asr.2019.01.020

[36] Talgat, A., Kishk, M. A., & Alouini, M. S. (2021). Stochastic geometry-based analysis of LEO satellite communication systems. *IEEE Communications Letters*, *25*(8), 2458-2462. https://doi.org/10.1109/LCOMM.2021.3064457

[37] Meng, Y., Bian, L., Han, L., Lei, W., Yan, T., & He, M. (2018). A global navigation augmentation system based on LEO communication constellation. In *2018 European Navigation Conference (ENC)* (pp. 65-71). IEEE. https://doi.org/10.1109/EURONAV.2018.8443173

EUROPEAN MECHANICAL SCIENCE

Research Article

e-ISSN: 2587-1110

Enhanced after-treatment warm up in diesel vehicles through modulating fuel injection and exhaust valve closure timing

Hasan Üstün Başaran[1*]

[1]Izmir Katip Celebi University, Naval Architecture and Marine Engineering Department, Türkiye

Orcid: H.Ü. Başaran (0000-0002-1491-0465)

Abstract: Exhaust after-treatment (EAT) units in diesel engine systems necessitate high exhaust temperature (above 250°C) to perform effectively and reduce the emission rates sufficiently during operation. Several methods such as exhaust throttling, early exhaust valve opening and late post fuel injection require high fuel penalty (mostly above % 10) to sustain EAT systems above 250°C. The aim of this numerical work is to combine delayed fuel injection and advanced exhaust valve closure in a diesel engine model to reduce the fuel penalty below % 10 as exhaust temperature is improved over 250°C. Fuel injection timing (FIT) is delayed up to 13°CA degrees from the nominal position. Exhaust valve closure is simultaneously advanced up to 30°CA degrees from the baseline as fuel injection is delayed in the system. Numerical results demonstrated that retarded fuel injection improved exhaust temperature moderately and needed relatively high fuel penalty. Unlike FIT modulation, early exhaust valve closure (EEVC) enhanced engine-out temperature effectively and required lower fuel penalty. However, EEVC caused a significant exhaust flow reduction, affecting EAT warm up negatively. Simultaneous application of EEVC and delayed FIT decreased the exhaust flow rate less than that in EEVC alone mode. Moreover, it kept fuel penalty below % 10, which was not found possible with RFI method alone in the system. EEVC + RFI combined method was also seen to heat up the EAT unit above 250°C in a fuel saving manner compared to RFI alone mode.

Keywords: diesel engines, late fuel injection, early exhaust valve closure, exhaust temperature, after-treatment warm up.

1. Introduction

Nowadays, many engine producers utilize EAT systems for diesel engines to decrease the harmful emission rates and meet the strict regulations issued by environmental agencies [1, 2]. EAT units are highly helpful in curbing emission rates. However, post-treatment units such as SCR, LNT and DOC are highly temperature-dependent and they tend to work effectively when they are adequately heated up to a certain temperature (~ 250°C) [3, 4]. The SCR unit, in particular, enables the desirable, effective NOx conversion between temperatures of 250°C and 450°C [5]. That high temperature requirement is problematic for diesel engines since exhaust temperature cannot be kept over 250°C particularly at low loads and thus, EAT units operate ineffectively [6]. There is a significant need for those loads to elevate exhaust temperature and enable improved EAT systems [7].

One effective approach to obtain high exhaust temperature is to implement variable valve timing (VVT) in compression-ignition engine systems [8–10]. Control of intake valve closure and exhaust valve opening is particularly useful for boosting exhaust-out temperature at low engine loads [11–13]. Negative valve overlap (NVO) via modulation of intake opening and exhaust closure is also found to be beneficial to elevate EAT inlet temperature in diesel engines [14, 15] as it partially traps the exhaust gas inside the cylinders [16]. Joshi et al. experimentally implemented NVO in a 6-cylinder diesel engine and achieved an exhaust temperature rise of 40°C with reduction in NOx rates by % 60 through internal exhaust gas recirculation [17].

In addition to engine valve timing actuation, some different fuel injection techniques can be investigated to achieve superior EAT thermal management [18]. One common method in this category is retarded fuel injection (RFI) [19]. Cavina et al. elevated exhaust temperature by 48°C through delayed SOI (15°C A from the baseline) in a 4-cylinder diesel engine system. However, it required % 15 rise in fuel consumption, which is considerable, to

*Corresponding author:
Email: hustun.basaran@ikcu.edu.tr

Cite this article as:
Başaran, H. (2024). Enhanced after-treatment warm up in diesel vehicles through modulating fuel injection and exhaust valve closure timing. *European Mechanical Science*, *8*(2): 93-103. https://doi.org/10.26701/ems.1441861

History dates:
Received: 23.02.2024, *Revision Request*: 24.04.2024, *Last Revision Received*: 09.05.2024, *Accepted*: 24.05.2024

achieve such an exhaust temperature improvement [20]. RFI deteriorates combustion effectiveness due to delayed injection timing, but it has the advantage of moderately improved exhaust temperature at low loads [21]. Close and late post-injection are other fuel injection-based techniques to enhance the outlet temperature. Post-injection rate and timing are generally seen to be directly related to the exhaust temperature [22].

Some engine-independent methods are continuously explored by researchers to improve exhaust temperature as well [23]. Electrical heating is one of the most promising of those outer-engine techniques [24]. After-burners and heat storage units are seen to enhance EAT thermal management too [25, 26]. Those methods necessitate additional energy supply and extra equipment to be positioned on the engine system [27] and therefore, mostly increase the manufacturing costs. However, those techniques also enable flexible and quick EAT heat up in diesel engine systems, which is a significant advantage in maintaining low emission rates.

In this work, delayed fuel injection is combined with advanced exhaust valve closure in a 1-D engine simulation model to achieve effective exhaust thermal management. Although those two techniques are separately beneficial to improve EAT thermal management, simultaneous implementation of them reduces the fuel penalty the system suffers to reach efficient EAT and thus, reduces emission rates.

2. Material and Methods

In this work, thermal management of exhaust unit of a diesel engine system is improved via proper adjustment of engine parameters. A previously validated simulation model is used in the analysis [11, 28]. The engine model and the technique applied in the model are explained in the following subsections.

2.1. Engine Model

The engine model created via using the Lotus Engine Simulation program [29] is demonstrated in Figure 1. It is operated with active six cylinders and each cylinder has double inlet and double exhaust valves. Those types of diesel engines are commonly utilized in commercial lorries and public buses, which require the exhaust unit warm up to keep emission rates at low levels. The focus in this study is to modulate the engine valve timing (mainly exhaust valve closure timing) and fuel injection timing to achieve that exhaust warm up in a fast and engine-dependent manner. It is desired to demonstrate that reasonable modulation of engine-specific components can be an alternative approach for rapid exhaust and thus, EAT unit warm up.

Properties of the diesel engine are given in Table 1. The valve timings in Table 1 are valid for nominal condition. The engine has single fuel injection and injection timing is also applied for base condition (1°CA BTDC), in which the system is operated at 1200 RPM engine speed and at

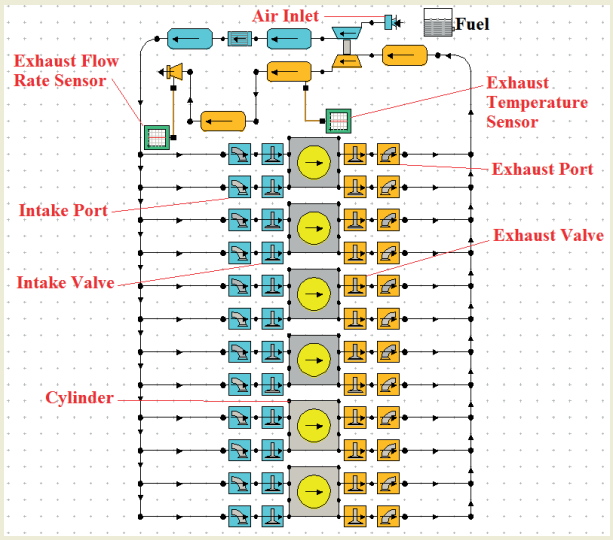

Figure 1. Engine model.

2.5 bar BMEP engine load. Compression ratio is maintained constant at 17.3 in all modes.

Table 1. Specifications of the diesel engine.

Bore (mm)	107
Stroke (mm)	124
Connecting rod length (mm)	192
Compression ratio	17.3:1
Exhaust Valve Opening	20°CA BBDC
Exhaust Valve Closure	20°CA ATDC
Intake Valve Opening	20°CA BTDC
Intake Valve Closure	25°CA ABDC
Start of Injection (SOI)	1°CA BTDC

2.2. Application of EEVC + RFI Technique

This work attempts to combine two different engine-based techniques to enhance the thermal management of the EAT unit in a diesel engine model. Fuel injection timing (shown as SOI timing in Table 1) and exhaust valve closure timings are the selected engine parameters to be modulated with the objective of improved ETM.

The change in EVC and SOI timing is demonstrated in Table 2. Those modulations are valid for EEVC_alone and RFI_alone modes. For those cases, only EVC or SOI timing is altered in the system. As seen in Table 2, exhaust unit is shut off earlier in the system as valve closure timings are steadily advanced and moved far from the starting EVC timing, 20°CA after top dead center (ATDC). For the last step, EVC timing is advanced to 20°CA BTDC, which is 40°CA earlier than the nominal (starting) timing. In addition to EEVC_alone mode, RFI_alone mode is also considered in Table 2. In that mode, SOI timing is retarded up to 12°CA ATDC with 2°CA increments.

For combined EEVC + RFI modes, change of EVC and SOI timing is shown in Table 3. SOI timing is modulated

for 3 different EEVC cases in Table 3: EEVC (0), EEVC (5) and EEVC (10) in which EVC timing is advanced 20°CA, 25°CA and 30°CA from the nominal EVC timing (20°CA ATDC), respectively. SOI timing is altered differently for each of those modes to achieve 250°C exhaust temperature in the system. Since exhaust temperature is predicted to increase more at EEVC (5) and EEVC (10) cases, the delay in SOI timing is relatively lower at those modes compared to EEVC (0) mode. While SOI timing is retarded up to 13°CA ATDC in EEVC (0) mode, it only needs to be delayed up to 10°CA or 7°CA ATDC in other EEVC modes in Table 3. Overall, those different combinations are examined with the aim of further improving the EAT thermal management in comparison to EEVC_alone and RFI_alone modes.

3. Results and Discussion

Firstly, impact of RFI and EEVC methods is examined separately on the model. The improvement in exhaust temperature and the rise in fuel penalty in each method are analyzed. Then, effect of combined EEVC + RFI method on exhaust temperature, mass flow rate and fuel penalty is explicitly examined.

Effect of RFI on in-cylinder temperature is seen in Figure 2 below. Different RFI modes – RFI (3), RFI (7) and RFI (11) with SOI timing of 3°CA, 7°CA and 11°CA ATDC, respectively – are compared with nominal mode in this plot. It is seen that delayed fuel injection tends to increase the in-cylinder temperature far from the TDC due to the retarded combustion of the fuel. In-cylinder pressure is relatively low at those piston positions and thus, maximum in-cylinder temperature is not as high as the one achieved in nominal condition. However, the expansion of in-cylinder gas in RFI modes, particularly in RFI (7) and RFI (11), begins in a rather delayed position compared to nominal case in Figure 2. Therefore, it is observed that in-cylinder temperature can be maintained at relatively higher levels in expansion process via proper use of RFI technique.

As demonstrated in Figure 2 above, delaying combustion highly affects the behavior of the in-cylinder gas. The improved in-cylinder temperature due to RFI positively affects the average exhaust temperature at turbine exit,

Table 2. Change of SOI and EVC timing in EEVC_alone and RFI_alone modes.

Method	Engine parameter	Nominal value	Change in every step	Total number of steps	Parameter value in furthest step
EEVC_alone	EVC Timing	20°CA ATDC	5°CA advanced	8	20°CA BTDC
RFI_alone	SOI Timing	1°CA BTDC	2°CA delayed	7	12°CA ATDC

Table 3. Change of SOI and EVC Timing in different EEVC + RFI combinations.

Method	EVC Timing (Constant)	SOI Timing Interval	Change in SOI Timing	Total number of steps
EEVC (0) + RFI	0°CA BTDC	Between 1°CA ATDC and 13°CA ATDC	3°CA delayed	5
EEVC (5) + RFI	5°CA BTDC	Between 1°CA ATDC and 10°CA ATDC	3°CA delayed	4
EEVC (10) + RFI	10°CA BTDC	Between 1°CA ATDC and 7°CA ATDC	2°CA delayed	4

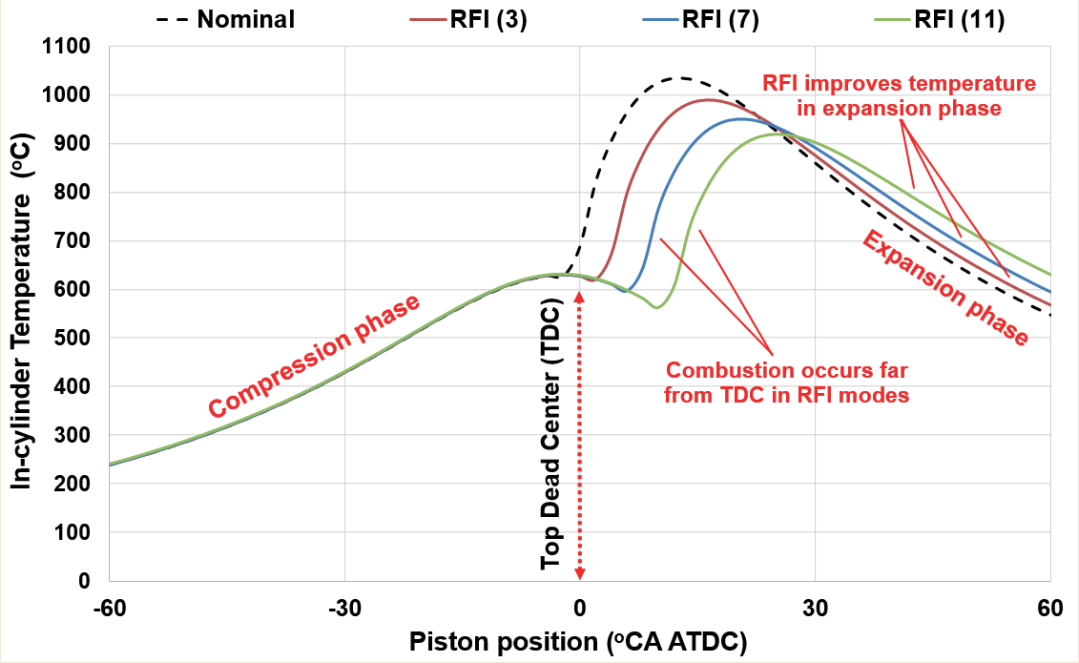

Figure 2. Effect of different RFI modes on engine in-cylinder temperature.

as shown in Figure 3 below. While the exhaust temperature is so close to 190°C at baseline, it approaches 225°C as RFI is aggressively applied in the system. As seen, exhaust temperature is increased steadily through retarded combustion. However, exhaust temperature cannot exceed 250°C, which is unable to keep EAT effectiveness at desirable levels. It is seen that fuel consumption is inevitably climbed as RFI is implemented in the system. The fuel consumption penalty in RFI modes in Figure 3 is calculated as the fuel increase percentage based on fuel consumption in nominal mode. It is obviously zero at nominal injection timing (1°CA BTDC), as this is the starting point in the analysis. It moves constantly upward as FIT is either moderately or extremely retarded from the nominal timing. The main reason for the undesirable fuel penalty in RFI mode in Figure 3 can be attributed to the ineffective combustion of the fuel due to low in-cylinder pressure. The more delayed the fuel injection timing is, the more additional fuel feeding is required for constant engine load. Even though the fuel penalty surpasses % 10, exhaust temperature still remains below 250°C. It can be derived that RFI is moderately effective in improving exhaust gas thermal management.

The rise in exhaust temperature via RFI technique is directly proportional with the fuel consumption penalty, as indicated in Figure 3. Therefore, when applied alone, use of extreme RFI is not desired to keep fuel penalty and emission rates below a certain level. Reasonable use of RFI seems to be more appropriate for EAT thermal management. The change of $IMEP_{gross}$ – gross power generating potential of the engine concerning mainly the closed cycle – and BMEP – net power generating potential of the engine concerning both closed and open cycles – in RFI mode in Figure 4 can be examined to understand the additional fuel need in the system.

Unlike previous plots, fuel injection rate is held constant

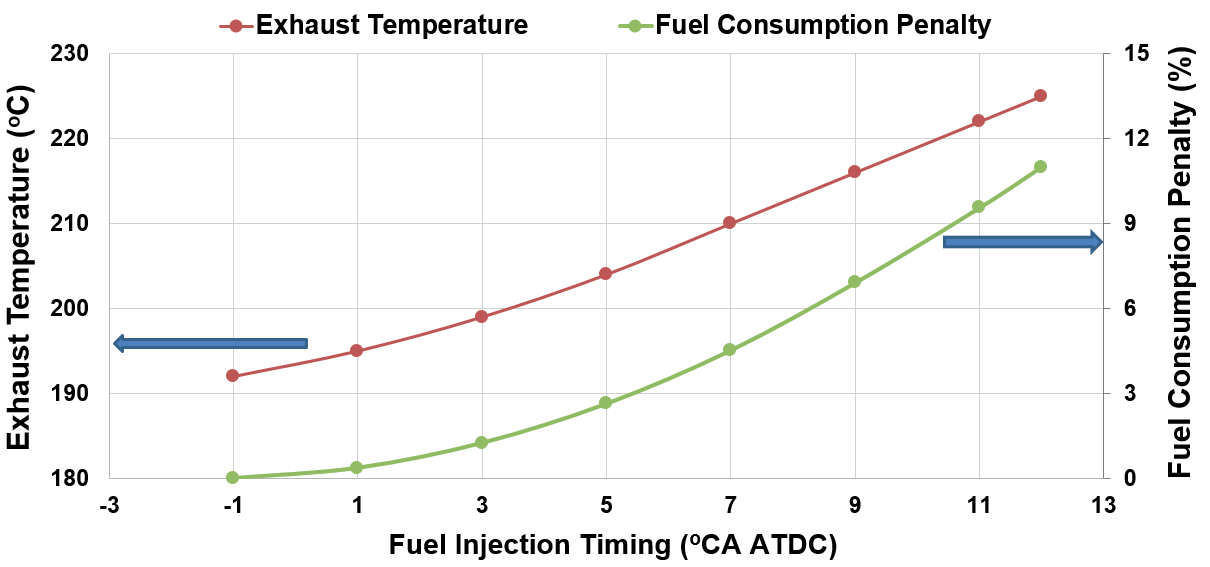

Figure 3. Effect of late fuel injection timing on exhaust temperature and fuel consumption penalty.

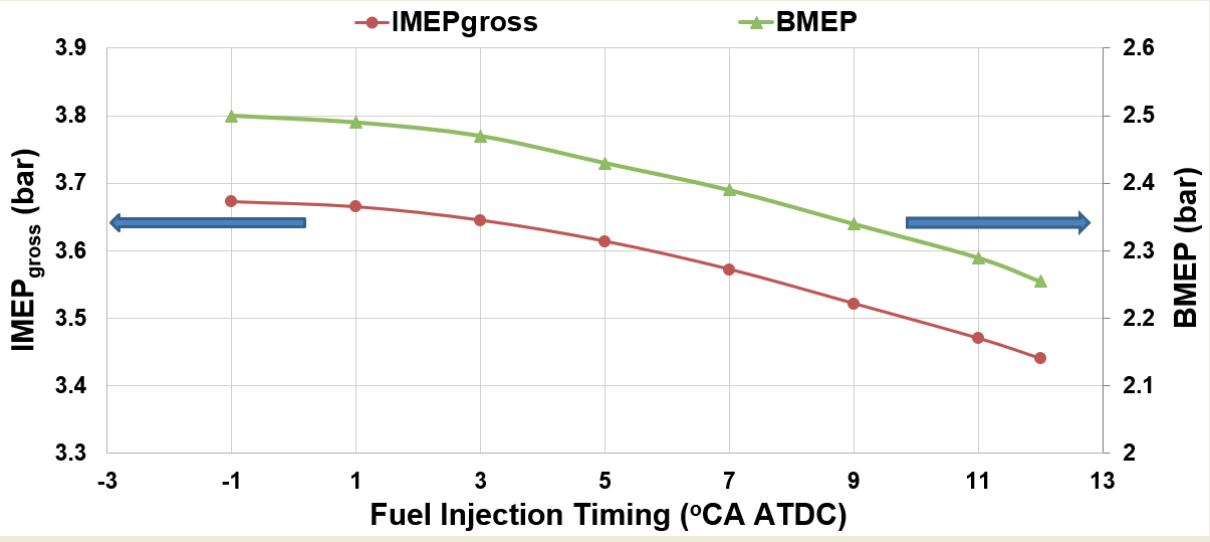

Figure 4. Effect of late fuel injection timing on $IMEP_{gross}$ and BMEP.

in Figure 4. It is explicit that BMEP is inevitably reduced as fuel injection is controlled in delayed timings. Constant fuel injection is inadequate to produce the same $IMEP_{gross}$ due to ineffective combustion. Lower $IMEP_{gross}$ results in reduced BMEP at RFI mode as the amount of fuel injection is kept constant. More energy needs to be utilized to maintain engine BMEP constant at 2.5 bar, which requires extra fuel injection, as seen earlier in Figure 3.

After demonstrating the effect of RFI, impact of EEVC on engine performance is examined in the following plots. At first, similar to RFI mode, the effect of EEVC on exhaust temperature and fuel penalty is observed in Figure 5 below. Advancing EVC timing in a slight manner does not noticeably affect exhaust temperature. However, after a certain EVC timing (particularly after 0°CA ATDC), exhaust temperature begins to rise sharply. Moderate use of EEVC can boost exhaust temperature as high as 230°C. Moreover, as EVC timing is advanced further than 15°CA BTDC, it is possible to sustain exhaust temperature above 250°C, which enables effective ETM and thus, effective EAT operation. Unlike RFI, EEVC technique in Figure 5 is able to keep the system in the effective ETM zone.

Similar to RFI technique, EEVC leads to fuel consumption penalty as shown in Figure 5. Slightly advanced EVC is not that problematic in terms of fuel penalty. However, as EVC timing is controlled significantly earlier than nominal

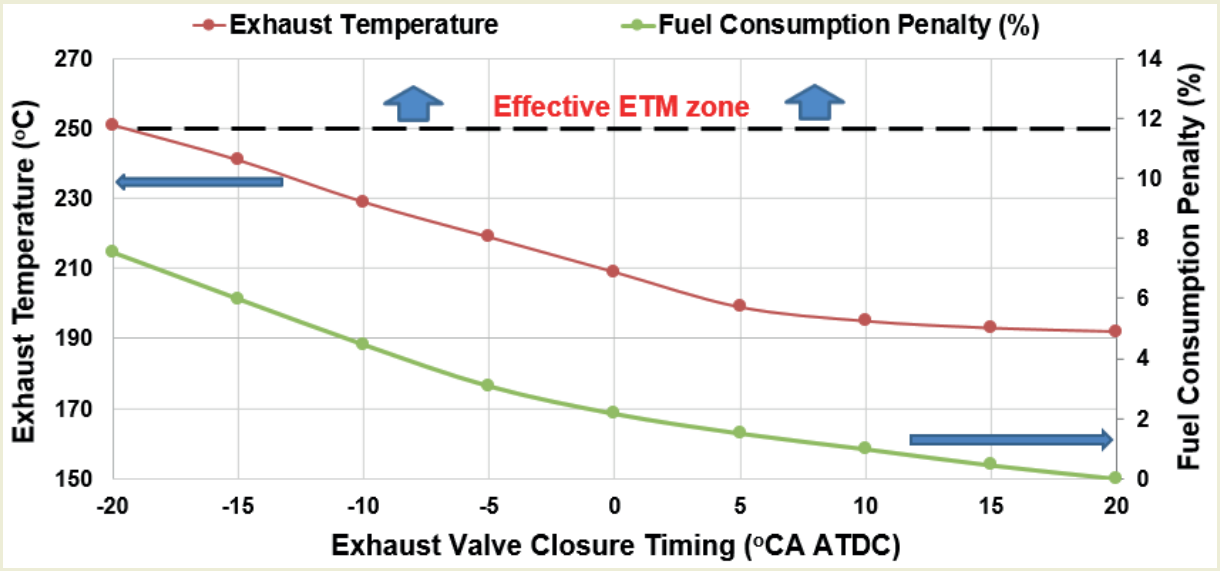

Figure 5. Effect of advanced EVC timing on exhaust temperature and fuel penalty.

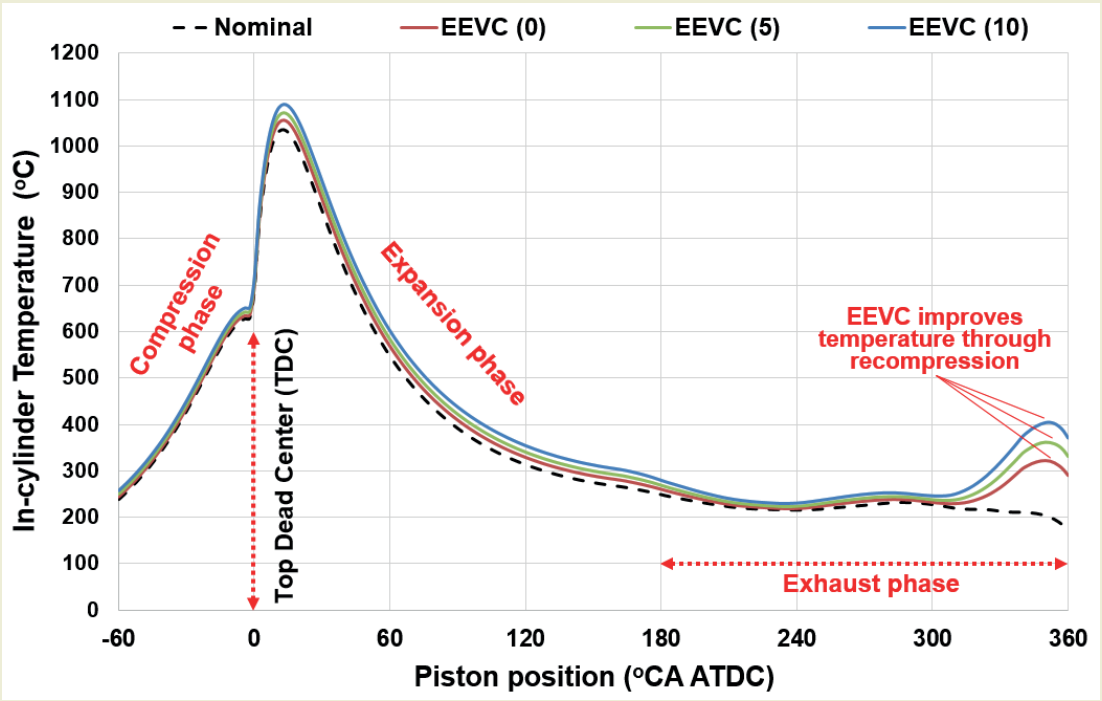

Figure 6. Effect of different EVC timings on in-cylinder temperature.

EVC timing, fuel penalty exceeds % 5 and can approach as high as % 8 in the system. Although there is an unavoidable increase in total fuel consumption in EEVC mode, the benefit of the method, namely the increase in exhaust unit temperature, is clearly visible in Figure 5. The potential of ETM improvement per fuel penalty rise in EEVC mode seems to be superior to the one achieved in RFI mode. In order to understand how EEVC is so effective at elevating exhaust temperature, the impact of EEVC on in-cylinder temperature is examined in Figure 6.

In-cylinder temperature behaves very differently for distinct EEVC modes – EEVC (0), EEVC (5) and EEVC (10) with EVC timing of 0°CA, 5°CA and 10°CA BTDC, respectively – in Figure 6. There is a particular variation in exhaust phase between nominal and EEVC modes. There is a noticeable recompression of exhaust gas in that period for EEVC cases, which is certainly not valid for nominal cases. As seen in Figure 6, there is a sudden rise in in-cylinder temperature in EEVC modes, which occurs due to early exhaust closure and compression of the in-cylinder gas. That recompression process mainly increases the pumping loss in the system and thus, leads to fuel penalty in Figure 5. In fact, fuel penalty is not the only negative effect of EEVC technique. Exhaust flow rate is reduced to low levels due to early shutoff of exhaust valves, as illustrated in Figure 7. Despite that considerable decrease in exhaust flow rate, rise in exhaust temperature is steadily improved through lowered air to fuel ratio (AFR), as seen in Figure 8.

Nominal exhaust flow rate (EVC at 20°CA ATDC) is maintained above 4.5 kg/min in Figure 7. However, particularly for moderate and extreme use of EEVC, exhaust flow rate drops down close to 3.5 kg/min, which is relatively low compared to nominal condition. As EVC is aggressively advanced, volumetric efficiency decreases close to % 70, which is considerable as it is almost % 25 lower than that obtained in nominal mode. That dramatic reduction in volumetric efficiency causes AFR to decrease

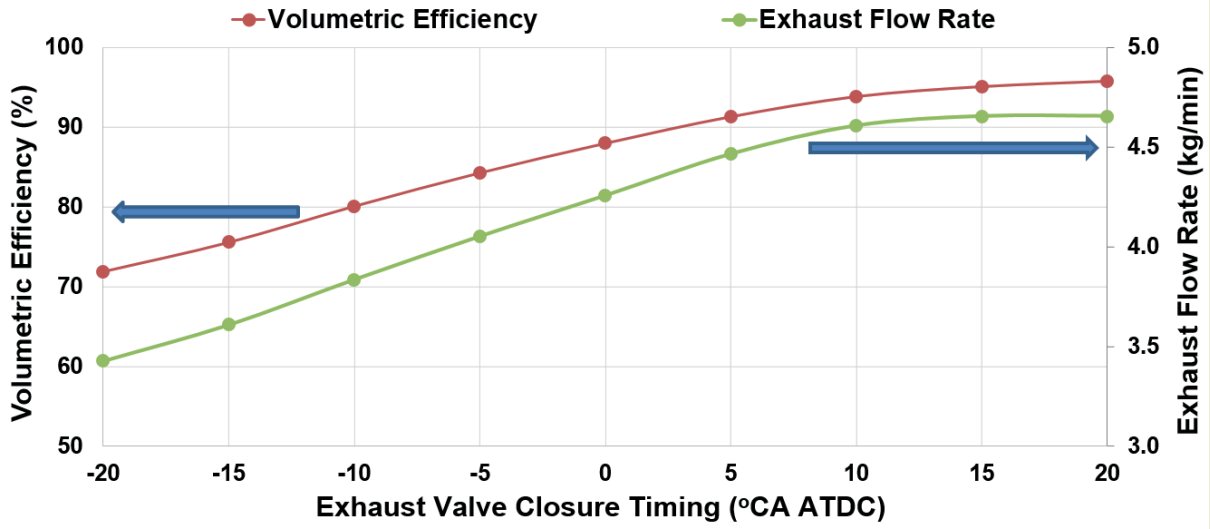

Figure 7. Effect of different EVC timings on volumetric efficiency and exhaust flow rate.

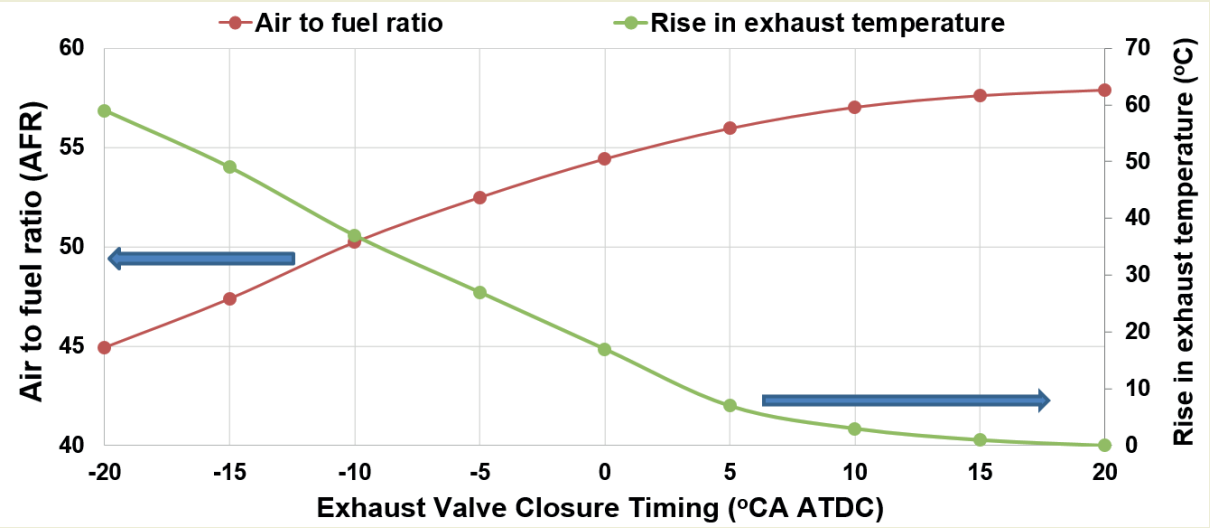

Figure 8. Effect of different EVC timings on AFR and rise in exhaust temperature.

as low as 45 and exhaust temperature improvement to be as high as 60°C in Figure 8. However, it is not that helpful to improve EAT warm up since heat up process generally needs high exhaust flow rate and thus, high in-cylinder airflow, which is not available in EEVC mode.

As seen earlier, RFI causes an undesirable fuel penalty with moderate rise in exhaust temperature in Figure 3. Moreover, EEVC elevates engine-out temperature with a notable decrease in exhaust flow rate in Figure 7. In order to elevate exhaust temperature with high exhaust flow rate, RFI and EEVC are combined as EEVC+RFI in the system, as presented previously in Table 3. The effect of different combinations of EEVC+RFI modes on exhaust temperature and BSFC are shown in Figure 9.

RFI alone and EEVC alone modes are placed in Figure 9 to compare them with the EEVC+RFI combined modes. As exhaust temperature is not the only parameter to assess the heat transfer rates to the EAT unit, the effect of those different combinations on exhaust flow rate is examined in Figure 10 as well. Considering the evident reduction in

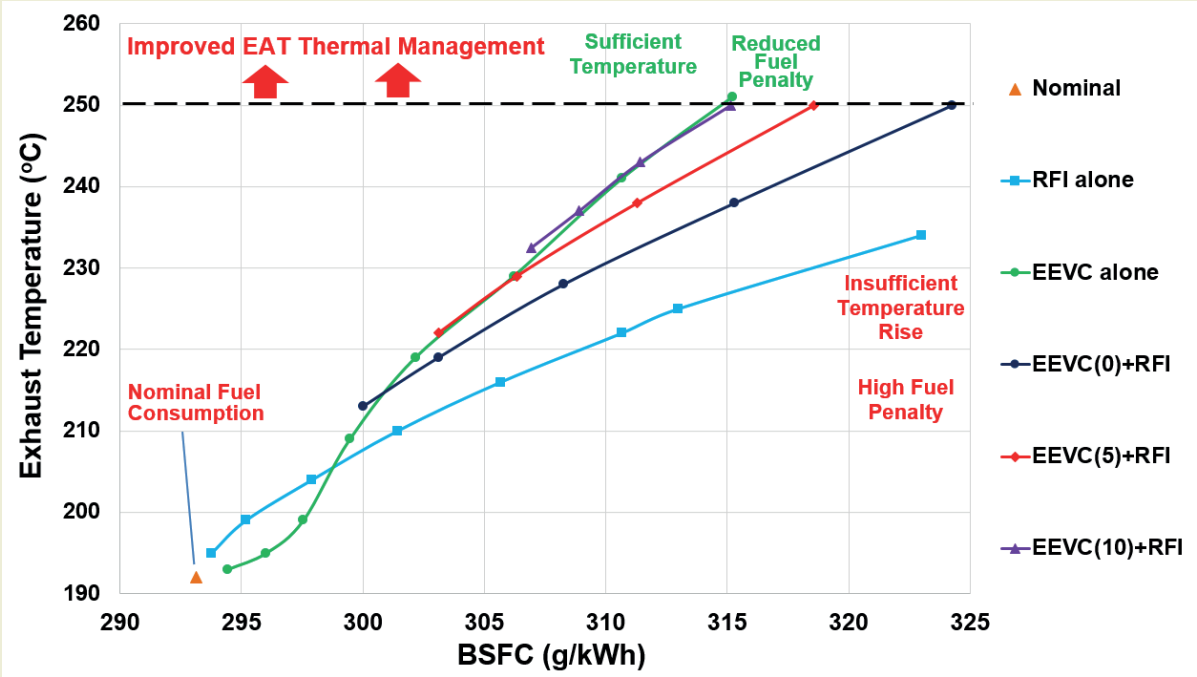

Figure 9. Effect of EEVC, RFI and EEVC+RFI modes on exhaust temperature and BSFC.

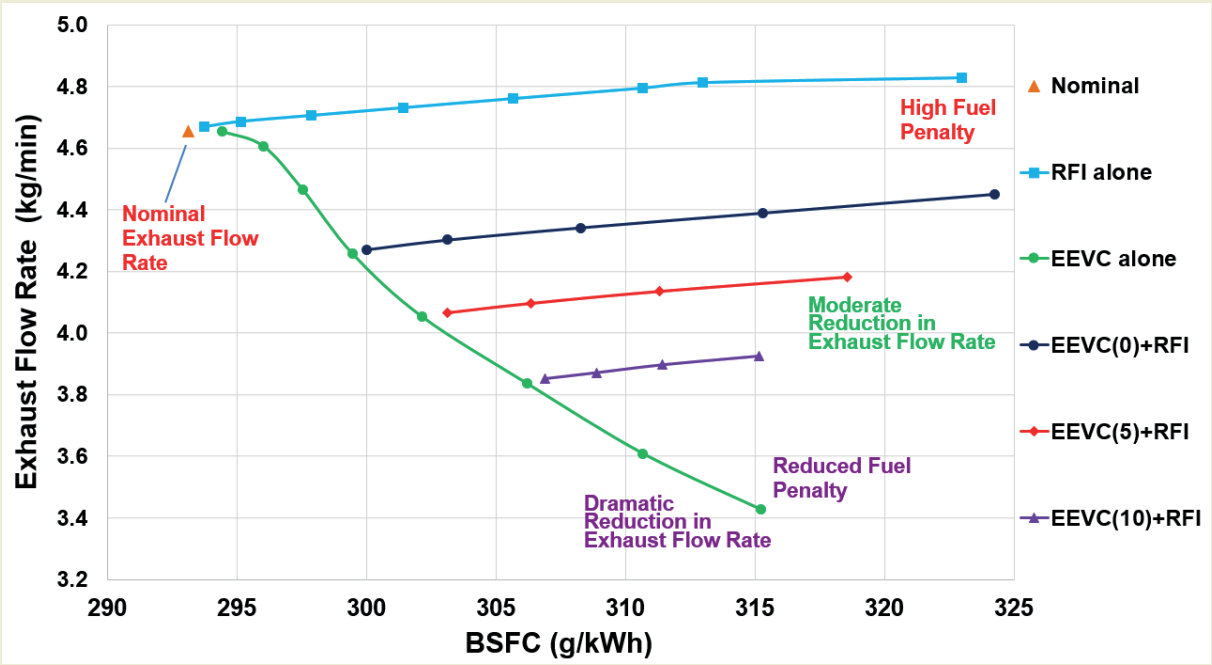

Figure 10. Effect of EEVC, RFI and EEVC+RFI modes on exhaust flow rate and BSFC.

exhaust flow rate in EEVC mode in Figure 7, evaluating only the exhaust temperature rise in a system is mostly insufficient to estimate its EAT improvement potential.

The most dramatic reduction in engine-out exhaust flow rate is observed in EEVC alone mode in Figure 10. This is because it has the most advanced EVC timing (20°CA BTDC) among all techniques. At this extreme position, exhaust port is sealed so early that exhaust flow rate is limited to close to 3.4 kg/min, which is dramatically below the nominal exhaust flow rate of close to 4.7 kg/min. As the closure timing is controlled at moderate levels, similar to EEVC (10) and EEVC (5) modes, exhaust flow rate begins to approach the level achieved in nominal mode. In RFI mode, exhaust flow rate increases compared to nominal mode since RFI, unlike EEVC-based methods, has a negligible effect on volumetric efficiency. It also causes the system to consume higher amount of fuel, resulting in the highest exhaust rate among all techniques.

The warm up process of the EAT unit can be best analyzed through considering the effect of both exhaust temperature ($T_{exhaust}$) and exhaust mass flow rate ($\dot{m}_{exhaust}$). Therefore, heat transfer rates $(\dot{Q})$ to the EAT unit are calculated using the equation (1) below [30]:

$$\dot{Q} = C(\dot{m}_{exhaust})^{\frac{4}{5}} (T_{exhaust} - T_{EAT\ catalyst\ bed}) \quad (1)$$

The $\dot{Q}$ rates are calculated at 1200 RPM and 2.5 bar BMEP for all methods. Then they are normalized by dividing all the values by the one achieved in nominal mode at 0°C EAT temperature. Those normalized heat transfer rates at different modes are indicated in Figure 11.

Nominal mode is seen to be the least effective method in Figure 11. The fact that exhaust temperature is too low to maintain EAT unit over 250°C is considered to be the main reason for this ineffectiveness. Since the magnitude of heat transfer (the temperature to which the EAT unit to be heated up) is mostly determined by exhaust temperature, nominal mode is predicted to be the worst case among all techniques as it has the lowest exhaust temperature (195°C). High exhaust flow rate in this mode affects EAT cool off process negatively as well.

RFI technique rises both exhaust temperature & exhaust flow rate and thus, it is the most effective method, particularly between -50°C and 50°C EAT temperature. However, exhaust temperature is limited to 225°C in that mode, and as EAT remains above 50°C, its effectiveness deteriorates. It is more advantageous to use EEVC+RFI techniques in Figure 11 when $T_{EAT\ unit}$ exceeds 50°C. This is because not only is it possible to sustain EAT unit temperature at 250°C in those techniques, but also the required fuel penalty can be reduced to as low as % 7.5, which is a significant benefit compared to RFI alone mode. The highest $\dot{Q}$ improvement (% 111) is achieved in EEVC(5) + RFI combined mode with % 8.6 fuel penalty, which demonstrates the benefit of combination and reasonable use of each method when the only objective is to maintain effective, fuel efficient after-treatment in the system. However, using only EEVC (5) + RFI may not be the fastest way to achieve active EAT operation in Figure 11. Considering the potential of RFI at cold EAT temperatures (particularly below 50°C), a better option for rapid EAT warm up may be to start with RFI alone and then continue the warm up process with EEVC (5) + RFI technique as $T_{EAT\ unit}$ exceeds 50°C in the system. Instead of a single strategy, it seems more attractive to apply different strategies during EAT get-hot process in Figure 11.

EEVC alone mode is found to be not that effective to accelerate the EAT get-warm process in Figure 11 although it can noticeably rise exhaust temperature above 250°C.

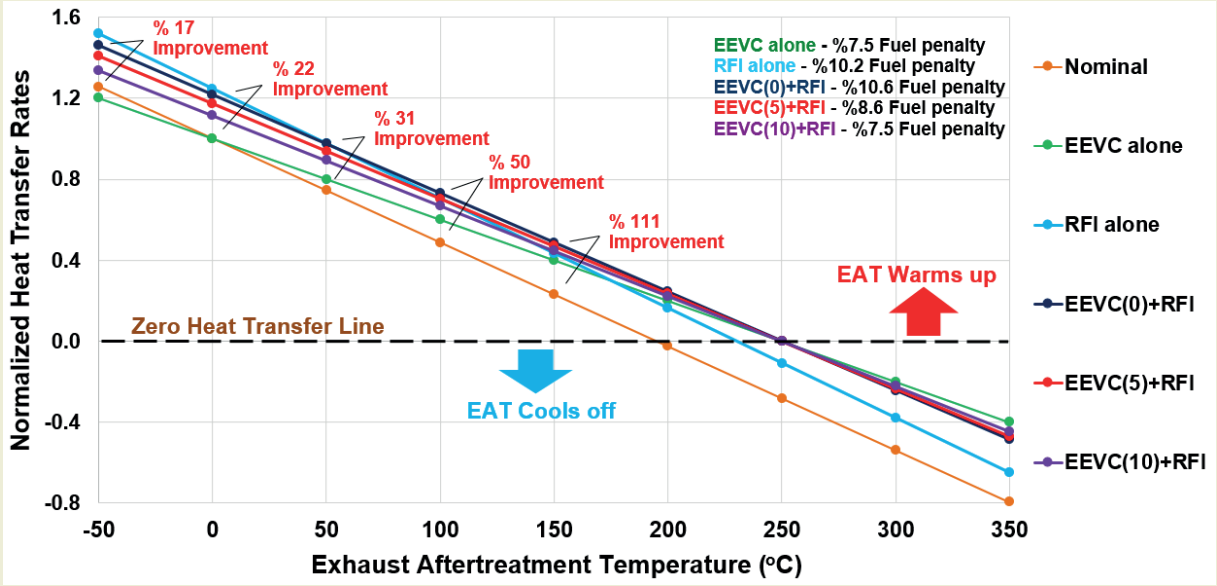

Figure 11. Change of heat transfer rates in EEVC, RFI and EEVC+RFI modes at 1200 RPM and 2.5 bar BMEP.

This is because EEVC brings down exhaust flow rate considerably (more than % 25) when it is aggressively used, as shown earlier in Figure 7. However, when $T_{EAT\ unit}$ is above 250°C, EEVC alone mode is found to be highly helpful to improve negative heat transfer rates due to low exhaust flow rates. Unlike RFI alone and nominal modes, those enhanced negative heat transfer rates in EEVC mode can slow down the EAT cool off process and can keep EAT unit above 250°C for longer periods of time. The requirement of only % 7.5 fuel penalty, which is relatively lower compared to other modes, is another important advantage of this technique during EAT stay-warm period in Figure 11.

4. Conclusion

This work concentrates on the improvement of EAT thermal management via use of RFI and EEVC. Firstly, the impact of those techniques is examined individually. It is seen that RFI can boost exhaust temperature in a moderate manner (from 195°C to 225°C) with a high fuel penalty (above % 10). Exhaust flow rate is not affected negatively in RFI mode. Unlike RFI, EEVC can rise exhaust temperature above 250°C with a relatively low fuel penalty (below % 8), which is advantageous. However, EEVC alone leads to a significant decrease (close to % 25) in exhaust flow rate, which affects EAT warm up negatively.

Considering the benefits of each mode, RFI and EEVC are simultaneously applied in the system as EEVC + RFI combined mode. The potential of different EEVC + RFI combined modes on the improvement of exhaust temperature, exhaust flow rate and EAT warm up is explicitly examined. It is observed that EEVC + RFI combined mode can increase exhaust temperature above 250°C with improved fuel penalty compared to RFI alone mode and can keep exhaust flow rate at higher levels compared to EEVC alone mode. Proper combination of RFI and EEVC has the capacity to achieve % 111 heat transfer rate improvement in comparison to nominal mode with a fuel penalty of % 8.6, which neither EEVC alone nor RFI alone method can achieve even with higher fuel penalty (above % 10). EEVC + RFI combined mode is also superior to RFI alone mode since it can improve EAT cool off process through reduced negative heat transfer rates to the EAT unit.

EEVC + RFI combined mode still causes undesirable fuel penalty in the system. Therefore, for fuel-efficient EAT warm up in diesel engine systems, other thermal management methods such as late intake valve closure or post-fuel injection can also be implemented in future studies to keep fuel penalty at feasible levels.

5. Nomenclature

ABDC	After bottom dead center
AFR	Air to fuel ratio
ATDC	After top dead center
BBDC	Before bottom dead center
BMEP	Brake mean effective pressure, bar
BSFC	Brake specific fuel consumption, g/kWh
BTDC	Before top dead center
CA	Crank angle, degree
DOC	Diesel oxidation catalyst
EAT	Exhaust after-treatment
EEVC	Early exhaust valve closure
ETM	Exhaust thermal management
EVC	Exhaust valve closure
FIT	Fuel injection timing
$IMEP_{gross}$	Gross indicated mean effective pressure, bar
LNT	Lean NOx Trap
NOx	Nitrogen oxide
RFI	Retarded fuel injection
RPM	Revolution per minute
SCR	Selective catalytic reduction
SOI	Start of injection timing, degree
TDC	Top dead center
VVT	Variable valve timing

Acknowledgement

I would like to sincerely thank Lotus Engineering Company for letting me use Lotus Engine Simulation software in this work.

Research Ethics

Ethical approval not required.

Author Contributions

The author accept full responsibility for the content of this article and have approved its submission.

Competing Interests

The author declare that there are no competing interests.

Research Funding

Not reported.

Data Availability

Not applicable.

References

[1] Dieselnet. (2024, May 7). Emission standards, European Union, passenger cars. Retrieved from https://www.dieselnet.com/standards/eu/ld.php#stds

[2] Dieselnet. (2024, May 7). Emission standards, United States, heavy-duty CI engines. Retrieved from https://www.dieselnet.com/standards/us/hd.php#stds

[3] Feng, R., Hu, X., Li, G., Sun, Z., Ye, M., & Deng, B. (2023). Exploration on the emissions and catalytic reactors interactions of a non-road diesel engine through experiment and system level simulation. *Fuel*, *342*, 127746. https://doi.org/10.1016/j.

fuel.2023.127746

[4] Mera, Z., Fonseca, N., Casanova, J., Deng, H., & López, J. M. (2021). Influence of exhaust gas temperature and air-fuel ratio on NOx aftertreatment performance of five large passenger cars. *Atmospheric Environment*, *244*, 117878. https://doi.org/10.1016/j.atmosenv.2020.117878

[5] Girard, J., Cavataio, G., Snow, R., & Lambert, C. (2009). Combined Fe-Cu SCR systems with optimized ammonia to NOx ratio for diesel NOx control. *SAE International Journal of Fuels and Lubricants*, *1*(1), 603–610. https://doi.org/10.4271/2009-01-2848

[6] Gao, J., Tian, G., Sorniotti, A., Karci, A.E., & Di Palo, R. (2019). Review of thermal management of catalytic converters to decrease engine emissions during cold start and warm up. *Applied Thermal Engineering*, *147*, 177–187. https://doi.org/10.1016/j.applthermaleng.2018.09.036

[7] Hu, J., Wu, Y., Yu, Q., Liao, J., & Cai, Z. (2023). Heating and storage: A review on exhaust thermal management applications for a better trade-off between environment and economy in ICEs. *Applied Thermal Engineering*, *220*, 119782. https://doi.org/10.1016/j.applthermaleng.2022.119782

[8] Arnau, F. J., Martin, J., Pla, B., & Auñón, Á. (2021). Diesel engine optimization and exhaust thermal management by means of variable valve train strategies. *International Journal of Engine Research*, *22*(4), 1196-1213. https://doi.org/10.1177/1468087420935302

[9] Basaran, H. U. (2023). Enhanced exhaust after-treatment warmup in a heavy-duty diesel engine system via Miller cycle and delayed exhaust valve opening. *Energies*, *16*(12), 4542. https://doi.org/10.3390/en16124542

[10] Kim, J., Vallinmaki, M., Tuominen, T., & Mikulski, M. (2024). Variable valve actuation for efficient exhaust thermal management in an off-road diesel engine. *Applied Thermal Engineering*, *246*, 122940. https://doi.org/10.1016/j.applthermaleng.2021.122940

[11] Basaran, H. U., & Ozsoysal, O. A. (2017). Effects of application of variable valve timing on the exhaust gas temperature improvement in a low-loaded diesel engine. *Applied Thermal Engineering*, *122*, 758–767. https://doi.org/10.1016/j.applthermaleng.2017.04.087

[12] Roberts, L., Magee, M., Shaver, G., Garg, A., McCarthy, J., Koeberlein, E., Holloway, E., Shute, R., Koeberlein, D., & Nielsen, D. (2015). Modeling the impact of early exhaust valve opening on exhaust after-treatment thermal management and efficiency for compression ignition engines. *International Journal of Engine Research*, *16*, 773–794. https://doi.org/10.1177/1468087415585903

[13] Basaran, H. U. (2020). Utilizing exhaust valve opening modulation for fast warm-up of exhaust after-treatment systems on highway diesel vehicles. *International Journal Automotive Science and Technology*, *4*(1), 10–22. https://doi.org/10.30939/ijastech..733877

[14] Gosala, D. B., Ramesh, A. K., Allen, C. M., Joshi, M. C., Taylor, A. H., Van Voorhis, M., Shaver, G. M., Farrell, L., Koeberlein, E., & McCarthy, J. Jr. (2018). Diesel engine aftertreatment warm-up through early exhaust valve opening and internal exhaust gas recirculation during idle operation. *International Journal of Engine Research*, *19*, 758–773. https://doi.org/10.1177/1468087417745821

[15] Başaran, H. Ü. (2019). Improving exhaust temperature management at low-loaded diesel engine operations via internal exhaust gas recirculation. *Dokuz Eylül Üniversitesi Mühendislik Fakültesi Fen ve Mühendislik Dergisi*, *21*(61), 125-135. https://doi.org/10.21205/deufmd.2019216112

[16] Polat, S., Solmaz, H., Yılmaz, E., Calam, A., Uyumaz, A., & Yücesu, H. S. (2020). Mapping of an HCCI engine using negative valve overlap strategy. *Energy Sources, Part A: Recovery, Utilization, and Environmental Effects*, *42*(9), 1140-1154. https://doi.org/10.1080/15567036.2019.1608471

[17] Joshi, M. C., Shaver, G. M., Vos, K., McCarthy Jr, J., & Farrell, L. (2022). Internal exhaust gas recirculation via reinduction and negative valve overlap for fuel-efficient aftertreatment thermal management at curb idle in a diesel engine. *International Journal of Engine Research*, *23*(3), 369-379. https://doi.org/10.1177/14680874211057760

[18] Başaran, H. Ü. (2023). Fuel injection strategies to improve after-treatment thermal management in diesel engine systems: A review. In *Advancing Through Applied Science and Technology* (pp. 59-84). Iksad Publishing House. https://doi.org/10.5281/zenodo.8428506

[19] Stadlbauer, S., Waschl, H., Schilling, A., & del Re, L. (2013). DOC temperature control for low temperature operating ranges with post and main injection actuation. *SAE Technical Paper*, No. 2013-01-1580. SAE International. https://doi.org/10.4271/2013-01-1580

[20] Cavina, N., Mangini, G., Corti, E., Moro, D., De Cesare, M., & Stola, F. (2013). Thermal management strategies for SCR after treatment systems. *SAE Technical Paper*, No. 2013-24-0153. SAE International. https://doi.org/10.4271/2013-24-0153

[21] Bai, S., Chen, G., Sun, Q., Wang, G., & Li, G. X. (2017). Influence of active control strategies on exhaust thermal management for diesel particular filter active regeneration. *Applied Thermal Engineering*, *119*, 297-303. https://doi.org/10.1016/j.applthermaleng.2017.04.029

[22] Nie, X., Bi, Y., Liu, S., Shen, L., & Wan, M. (2022). Impacts of different exhaust thermal management methods on diesel engine and SCR performance at different altitude levels. *Fuel*, *324*, 124747. https://doi.org/10.1016/j.fuel.2022.124747

[23] Wu, G., Feng, G., Li, Y., Ling, T., Peng, X., Su, Z., & Zhao, X. (2024). A review of thermal energy management of diesel exhaust after-treatment systems technology and efficiency enhancement approaches. *Energies*, *17*(3), 584. https://doi.org/10.3390/en17030584

[24] Gao, J., Tian, G., & Sorniotti, A. (2019). On the emission reduction through the application of an electrically heated catalyst to a diesel vehicle. *Energy Science & Engineering*, *7*(6), 2383-2397. https://doi.org/10.1002/ese3.412

[25] McCarthy Jr, J., Matheaus, A., Zavala, B., Sharp, C., & Harris, T. (2022). Meeting future NOx emissions over various cycles using a fuel burner and conventional aftertreatment system. *SAE International Journal of Advances and Current Practices in Mobility*, *4*(2022-01-0539), 2220-2234. https://doi.org/10.4271/2022-01-0539

[26] Pise, G., & Nandgaonkar, M. (2023). Enhancement of catalytic converter performance to reduce cold start emissions with thermal energy storage – An experimental study. *Materials Today: Proceedings*, *72*, 1125-1131. https://doi.org/10.1016/j.matpr.2023.01.383

[27] Massaguer, A., Pujol, T., Comamala, M., & Massaguer, E. (2020). Feasibility study on a vehicular thermoelectric generator coup-

led to an exhaust gas heater to improve aftertreatment's efficiency in cold-starts. *Applied Thermal Engineering, 167*, 114702. https://doi.org/10.1016/j.applthermaleng.2019.114702

[28] Lotus Engineering. (2024, May 7). Getting started with Lotus engine simulation. Retrieved from https://lotusproactive.files.wordpress.com/2013/08/getting-started-with-lotus-engine-simulation.pdf

[29] Lotus Engineering Software. Lotus engine simulation (LES) version 6.01A. Norfolk, UK: Lotus Engineering.

[30] Ding, C., Roberts, L., Fain, D. J., Ramesh, A. K., Shaver, G. M., McCarthy, Jr. J., Ruth, M., Koeberlein, E., & Holloway, E. A. (2016). Fuel efficient exhaust thermal management for compression ignition engines during idle via cylinder deactivation and flexible valve actuation. *International Journal of Engine Research, 17*(6), 619-630. https://doi.org/10.1177/1468087416636244

EUROPEAN MECHANICAL SCIENCE

Review Article

e-ISSN: 2587-1110

Advancements in polylactic acid research: From material properties to sustainable applications

Arslan Kaptan[1*], **Fuat Kartal**[2]

[1]Sivas Cumhuriyet University, Sivas Technical Sciences Vocational School, Motor Vehicles and Transportation Technologies Department, Türkiye
[2]Kastamonu University, Engineering and Architecture Faculty, Mechanical Engineering Department, Türkiye

Orcid: A. Kaptan (0000-0002-2431-9329), F. Kartal (0000-0002-2567-9705)

Abstract: This review article provides a comprehensive examination of the latest advancements in the research and development of Polylactic Acid (PLA) and its composites, with a focus on enhancing material properties and exploring sustainable applications. As a biodegradable and bio-base polymer, PLA has emerged as a promising alternative to conventional petroleum-based plastics across various industries, including packaging, 3D printing, and biomedical fields. The review delves into studies investigating the effects of environmental conditions on PLA's hydrolytic stability and structural integrity, as well as the benefits of blending PLA with other biopolymers to improve its mechanical properties. It also covers research on optimizing three dimensional printing parameters for PLA, underscoring the importance of raster orientation and print layer thickness in achieving desired mechanical strength and object durability. Additionally, the incorporation of nanofillers and copolymers is discussed as a strategy for enhancing PLA's moisture resistance and overall performance. By summarizing key findings from a wide range of studies, this article aims to shed light on the significant progress made in PLA research, while pointing out future research directions to resolve existing limitations and fully capitalize on PLA's potential as a green material solution. To better cater to the needs of design engineers, this review highlights how advancements in PLA research can be directly applied to improve product design and functionality. Specifically, it discusses the enhanced mechanical properties, sustainability benefits, and versatility of PLA in various industrial applications, providing engineers with a deeper understanding of how to utilize PLA in eco-friendly design solutions.

Keywords: Additive manufacturing, three dimensional printing, polylactic acid, biodegradable polymers, mechanical properties, sustainable materials.

1. Introduction

Escalating environmental concerns associated with the accumulation of petroleum-based plastics have spurred the search for sustainable, biodegradable alternatives. Among these, Polylactic Acid (PLA) stands out as a frontrunner due to its bio-based origins and compostable nature. Derived primarily from renewable resources such as corn starch, or tapioca roots, PLA presents a reduced carbon footprint and an end-of-life biodegradability that positions it as an eco-friendly substitute for conventional plastics in numerous applications. This review article aims to explore the advancements in PLA research, focusing on its material properties, the enhancements achieved through blending and compounding, and its burgeoning applications in various domains of sustainability [1-12].

PLA's journey from a biopolymer primarily used in medical applications, due to its biocompatibility and biodegradability, to a broader utility in packaging, agriculture, textile, and notably, in three dimensional (3D) printing, underscores its versatility. However, despite its promising attributes, PLA's widespread adoption faces challenges, including its hydrolytic stability under humid conditions, mechanical strength, and thermal resistance, which can limit its performance in certain applications. Research efforts have been directed towards addressing these limitations, examining the effects of environmental conditions on PLA, and exploring the potential of PLA composites to enhance its property profile. Moreover, the role of 3D printing technology in expanding the applications of PLA has been significant. The ability to optimize printing parameters to tailor mechanical properties (MPs) of PLA objects offers a pathway to custom, on-demand manufacturing of biodegradable products. Concurrently, the environmental implications of PLA's life cycle, from production to degradation, warrant a comprehensive analysis to ensure its benefits are fully realized in the context of sustainability. This introduction

*Corresponding author:
Email: akaptan@cumhuriyet.edu.tr

Cite this article as:
Kaptan, A., Kartal, F. (2024). Advancements in polylactic acid research: From material properties to sustainable applications. *European Mechanical Science, 8*(2): 104-114. https://doi.org/10.26701/ems.1440630

History dates:
Received: 21.02.2024, *Revision Request*:17.04.2024, *Last Revision Received*: 30.04.2024, *Accepted*: 05.05.2024

sets the stage for a detailed review of the current state of PLA research, highlighting the innovative approaches being taken to overcome its inherent limitations and expand its utility. The following sections will discuss hydrolytic stability of PLA, the development of its mechanical properties, the optimization of 3D printing processes for PLA-based materials, and the environmental considerations that accompany the use of PLA. On the other hand, a holistic view of PLA's potential as a sustainable product will be presented [13-21].

1.1. Literatur surway

The burgeoning interest in sustainable materials has catalyzed a significant amount of research into biodegradable polymers, among which PLA has emerged as a particularly promising candidate. This literature survey aims to provide a comprehensive overview of the existing research on PLA, focusing on its synthesis, properties, modifications, applications, and environmental impact. As the demand for eco-friendly alternatives to petroleum-based plastics continues to rise, understanding the advancements and challenges associated with PLA becomes crucial for its successful integration into various industries. PLA, a biopolymer derived from renewable resources, offers a compelling combination of biodegradability, biocompatibility, and a relatively low carbon footprint [22-24]. These attributes make it an attractive material for applications ranging from packaging and disposable items to medical devices and 3D printing. However, the full potential of PLA is often hindered by certain limitations, including its MPs, thermal resistance, and hydrolytic stability, which can vary significantly depending on its crystalline structure and molecular weight. Recent studies have focused on overcoming these challenges through various strategies, including copolymerization, blending with other biopolymers or additives, and the development of PLA composites with enhanced properties. The literature also extensively explores optimization of processing techniques such as 3D printing, which has opened new avenues for customizing PLA's properties for specific applications. Moreover, environmental impact of PLA, from its production to post-use degradation, is a critical area of investigation. While PLA's biodegradability is a significant advantage over traditional plastics, the conditions under which it degrades and the by-products of this process require careful consideration to ensure its environmental benefits are maximized.

This literature survey will delve into these key areas of PLA research, highlighting the latest findings, identifying gaps in current knowledge, and suggesting directions for future studies. By synthesizing the wealth of research on PLA, this survey aims to contribute to the ongoing efforts to develop sustainable materials that can meet the needs of a variety of applications while minimizing environmental impact.

Literature review has been categorized under subheadings according to the focal points of the study areas.

1.1.1 Material properties and stability

In their work, Letcher and Waytashek (2014) used a home-type 3D printer to apply tensile, bending, and fatigue tests to samples printed with commercial PLA filament, accessible to a home user. They printed samples at 0, 45, and 90° raster orientation angles to test the effects of part strength orientation, determined all sample sizes according to ASTM D638 standards, and printed the samples at 100% fill density. Tensile test samples were tested at room temperature with a displacement speed of 5 mm/min. They also conducted tensile tests on PLA filaments, performing experiments at inter-head distances of 200 mm and pulling speeds of 500, 200, 50, and 5 mm/min. Tensile tests on printed samples found that 45° raster-oriented samples had the highest strength. In fatigue testing, 90° raster-oriented samples showed the least resistance to fatigue loads, while 45° and 0° raster-oriented samples had very similar fatigue lives, necessitating further research. They also examined the printed samples under a microscope and determined the sizes of voids formed during the printing process [25].

Kaygusuz et al., (2018) the effect of parameters such as fill density and nozzle temperature on MPs of materials printed with PLA in a 3D printer was examined. Tensile test specimens printed according to ASTM D638- Type 4 standard were tested at room temperature with a displacement speed of 5 mm/min. It was observed that an increase in nozzle temperature resulted in an increase in mechanical strength of specimens. Scanning Electron Microscope (SEM) images showed that the increase in nozzle temperature reduced the porous structure in the specimen. A decrease in fill density reduced tensile strength of the specimen, while SEM images also showed a significant reduction in the number of fibers carrying the load in direction of tension [26].

In a thesis by Çiçek (2019), the effect of fill rates on MPs of samples produced from PLA and Acrylonitrile Butadiene Styrene (ABS) filaments using Fused Deposition Modeling (FDM) technology was investigated. Samples produced at fill rates of 25, 50, 75, and 100% were subjected to tensile tests at a speed of 5 mm/min. This test revealed that the strength of ABS filament was higher than that of PLA. It was also reported that as the fill density increased, the strength of samples increased correspondingly. It was noted that samples made from ABS and PLA filaments broke in a brittle manner and showed limited elongation after exceeding yield strength in their tensile graphs [27].

Mansingh et al. (2023) the explore development of eco-friendly composites using 3D printing technology, combining chitin and chitosan with PLA. This study reveals that adding chitin and chitosan reduces strength and stiffness of PLA composites, with the lowest tensile and flexural strengths observed at a 0.5 wt% reinforcement concentration. Despite these reductions, the composites exhibit enhanced ductility compared to neat PLA, suggesting potential applications like food packag-

ing, although further research is needed to optimize MPs and interfacial bonding [28].

1.1.2. Composite materials

Sajna et al. (2016) reported on the effect of moisture absorption and accelerated weather conditions on properties of graft copolymer compatible PLA bionanocomposites. They submerged the samples in distilled water baths at room temperature for 30 days, measuring the amount of moisture absorbed at each time interval. They noted that adding C30B nanoclay and graft copolymer to fiber-reinforced PLA composites reduced the rate of moisture absorption. They examined the changes in MPs caused by moisture absorption using tensile and impact tests, stating that exposure to moisture significantly reduced MPs. They characterized the morphology of biocomposites using SEM and bionanocomposites using Transmission Electron Microscopy (TEM), also reporting the effect of accelerated weather conditions on MPs and confirming the results with SEM analysis [29].

Arrieta et al. (2017) created blends from PLA and Polyhydroxybutyrate (PHB) materials through a melt blending approach for food packaging applications, as an alternative to traditional petrochemical-based polymers. They highlighted that PHB, with a similar melting temperature and high crystallinity properties, was a good candidate for blending with PLA. They mentioned that PHB acted as a nucleating agent for PLA, enhancing the mobility, mechanical strength, and barrier performance of the blend. Fouirer Transform Infrared Spektrofotometre tests indicated that the spectral profiles of PLA and PHB, being semi-crystalline polymers, were significantly influenced by their physical states and crystalline structures. The presence of PLA component accelerated the hydrolytic degradation of PHB, while PHB crystallized PLA, leading to materials with higher barrier performance and better mechanical strength [30].

Ausejo et al. (2018) researched the effects of print direction and hydrolytic degradation at 50 °C and 70 °C on properties of dumbbell-shaped samples produced by 3D printing from commercial PLA and Polylactic Acid/Polyhydroxyalkanoates (PLA/PHA) filaments. They printed the samples in both horizontal and vertical directions. They found that middle section of horizontally printed PLA/PHA samples, being at the same temperature as bottom layer's platform, had a higher crystallization rate than vertically printed samples. The middle part of vertically printed samples, being further from and cooler than the platform, showed the lowest crystallization rate. They determined that the contact time of the samples with 3D printer platform during printing led to an increase in the crystalline phase. They concluded that horizontally 3D-printed PLA and PLA/PHA samples were more regular and emphasized the importance of considering 3D printing direction as a significant parameter when designing applications for 3D printed materials [31].

Ayrilmis (2018) investigated the effect of print thickness on surface roughness and wettability of 3D-printed samples made from commercial wood flour/PLA filament (30% wood flour and 70% PLA by weight). They used four different print thicknesses: 0.05, 0.1, 0.2, and 0.3 mm for producing 3D-printed samples. They considered Ra, Rz, and Ry roughness values to evaluate the surface characteristics of the samples, which were measured using a surface roughness measurement device. They characterized the wettability behavior of the samples using the contact angle method (goniometer technique). They found that with decreasing print thickness, surface smoothness of the samples significantly increased, while the wettability of the samples significantly increased with increasing print thickness. They noted that as the print thickness decreased, production time increased due to longer print times, thereby increasing the total cost. Considering the test results and print time, they suggested that optimal print thickness for 3D-printed wood flour/PLA composite filaments should be 0.2 mm [32].

In his master's thesis, Patan (2019) used ABS and chopped carbon fiber-reinforced ABS filaments to produce tensile test specimens with a 3D printer according to ASTM D638-Type 1 code and experimentally examined their MPs. He applied load to the specimens in tensile test conducted according to ASTM standards at a pulling speed of 5 mm/min until failure occurred. Using the experimental results, he numerically analyzed maximum stresses and deformation energies of the specimens in ANSYS software according to von Mises criterion. Mechanical experiments showed that flexural and compressive strengths of carbon fiber-reinforced ABS specimens were respectively 23.9% and 14.75% higher than those of unreinforced ABS specimens. Analytical stress analyses conducted with experimental mechanical results as input modeled tensile, compressive, and bending behaviors of both types of specimens with minimal deviations [33].

Przekop et al. (2020) discussed the search for superior materials by composite making due to some disadvantages of PLA like low impact strength, poor gas barrier, and low crystallization rate, similar to other biopolymers. They identified graphite as a candidate for modifying PLA due to its low cost, excellent thermal, and electrical properties. They emphasized that graphite significantly improved the lubricating properties of polymeric materials, reducing friction and increasing wear resistance. They tested the wear, mechanical, and chemical properties of specimens produced with 1, 2.5, 5, 7.5, and 10% weight ratios of graphite, also conducting measurements after aging. They took SEM images of the specimens before and after friction tests. They found a significant reduction in wear with increasing graphite content and determined that PLA+10% graphite composite specimen had a wear rate three times lower than the reference PLA specimen. After aging, PLA+10% graphite composite specimen had 11% lower breaking stress, 47% lower impact strength, and 21% higher Young's modulus com-

pared to the reference PLA specimen. Additionally, the addition of graphite significantly increased hydrophobic properties of composites and raised the material's glass transition temperature [34].

Uzun and Erdoğdu (2020) worked on 1.75 mm diameter composite PLA filaments reinforced with 20% copper and 20% carbon fiber, as well as Frosch brand PLA filaments. They produced tensile specimens from each filament using FDM method in a 3D printer and obtained TEM images of the fracture surfaces of test result specimens. Following their experiments, they determined that tensile strengths of composite filaments produced by reinforcing PLA material with copper and carbon fiber decreased. They emphasized that this decrease in strength was due to the reinforcements reducing the continuity of the matrix and weakening the interface adhesion. While PLA specimens broke more ductilely compared to copper and carbon fiber-reinforced specimens, copper-added composite PLA specimen broke in a brittle manner [35].

Thakur et al. (2024) conducted a study on the optimization and machine learning prediction of MPs in hybrid additive manufacturing of PLA-CF-PLA sandwiched composite structures. The research focused on enhancing MPs of these composites through the manipulation of fabrication parameters such as carbon fiber orientation, nozzle temperature, and bed temperature. Utilizing Classification and Regression Trees for machine learning, the study successfully predicted optimal settings for manufacturing, highlighting significant implications for the application of these composites in aerospace, automotive, and biomedical engineering [36].

1.1.3. Biodegradability and recycling

Rajeshkumar et al. (2021) present a comprehensive review on the development and application of environmentally friendly, renewable, and sustainable PLA-based natural fiber reinforced composites. This study examines the synthesis, degradation, applications, and manufacturing methods of PLA composites, emphasizing the beneficial impact of natural fiber reinforcements on properties of PLA. It aims to provide a holistic understanding of PLA-based biocomposites for academicians, industry personnel, and researchers, highlighting their significance in promoting sustainable and eco-friendly material solutions across various industries [37].

Rezvani Ghomi et al. (2021) conducted a life cycle assessment for PLA to position it as a low-carbon material, addressing its entire life cycle from production to end-of-life options. The study highlights the potential of PLA to reduce greenhouse gas emissions and its dependency on energy sources by optimizing the conversion process. The research underlines the significant role of PLA in the shift towards more sustainable materials, emphasizing the importance of improving recycling infrastructures and processes to further minimize its environmental impact [38].

Zhang and Thomas (2011) investigated the biodegradation, thermal, and MPs of PLA/PHB biopolymers mixed in ratios of 25, 50, 75, and 100%. According to their SEM imaging, PHBs exhibited irregular fractures, while PLAs had typical surface fractures seen in an amorphous polymer. They argued that the irregular fractures in PHBs were due to their crystalline structure [39].

Kamau-Devers et al. (2019) investigated the hydrothermal degradation, moisture absorption, morphology, and thermal conductivity of wood flour-filled PLA bio-composites. They conditioned composites containing 0, 10, and 30% by weight wood flour either fully immersed in water or in a completely dry state at four temperatures (7, 25, 35, and 47 °C). They noted that the increase in temperature led to an increase in moisture uptake and crystallinity amount. The drops in glass transition and melting temperatures associated with the increases in crystallinity levels of water-immersed samples were clearly determined compared to dried PLA samples [40].

Kakanuru and Pochiraju (2020) studied the moisture absorption and age-related degradation of parts made from PLA, Silicon Carbide (SiC) filled PLA composites, and ABS using Fused Filament Fabrication (FFF). They compared the hygroscopic stability of PLA and PLA/SiC composite specimens with ABS specimens. Both filaments and tensile test specimens were aged in distilled water at 50 °C and 70 °C for 140 days or until complete degradation. They defined the degradation of the polymer by observing differences in moisture absorption-desorption characteristics and deterioration in tensile strength. Experimental results showed that PLA and 20% SiC/PLA specimens degraded within 58 days at 50 °C, while SiC/PLA specimens with a higher SiC content maintained their stability for 140 days. They observed large voids in the material due to decomposition, with SEM images confirming the void geometry between aged and unaged specimens [41].

In review study of Nandhini et al. (2023), authors focus on the production and application of lignin and PLA for bioplastics and valuable chemicals, emphasizing their potential in mitigating global warming and plastic pollution through sustainable solutions. The document covers various production techniques, microbial degradation pathways, and conversion of these biopolymers into high-value chemicals such as muconic acid, hydrouronic acid, adipic acid, and terephthalic acid. Highlighting the environmental benefits, the review discusses the significance of deriving biopolymers from bioresources and organic waste, showcasing advancements in biopolymer production technology, degradation mechanisms, and their wide-ranging industrial applications. Unfortunately, specific author and publication year details were not captured in the quoted text [42].

1.1.4. Application areas

Siracusa et al. (2020) aimed to produce entirely bio-based blends based on two polyesters, PHB and PLA, as real competitors to replace petroleum polymers in the packaging industry. They highlighted PHB, main and most common-

ly used member of PHA family, showing great potential to replace fossil-based synthetic packaging. They prepared PHB/PLA blends in different ratios. They noted that in its homopolymeric state, PHB exhibited a high stereoregularity leading to a high degree of crystallinity up to 70-75% by weight. They stated that the optimal combination of biopolymer crystal entities (crystals, lamellae, spherulites) and inter-crystalline tie chains supported suitable MPs such as a high modulus of elasticity around 2.5-3 GPa and tensile strength at break around 35-40 MPa. They emphasized that the expansion lamellae and spherulite morphology of this biopolymer formed a good barrier structure with suitable low permeability values for atmospheric gas components and water vapor [43].

Johansson et al. (2023) examine the impact of lignin acetylation on MPs of lignin-PLA biocomposites, aiming to enhance sustainability in applications such as automotive and aerospace. The study demonstrates that acetylation improves interfacial adhesion between lignin and PLA, resulting in increased impact strength, thermal stability, and moisture repellency. These findings suggest acetylated lignin's potential in creating lighter, sustainable composite materials without compromising performance, marking a significant step towards the development of environmentally friendly biocomposites [44].

Tripathi et al. (2021) review durable PLA-based blends and biocomposites, emphasizing their role in supporting a low carbon economy. They discuss the environmental impact of traditional plastics and potential of PLA-based products to reduce the carbon footprint by replacing fossil carbon with renewable carbon. The review covers recent advancements in enhancing PLA durability, including the use of synthetic plastics, fibers, natural fibers, and biocarbon. It also examines the effects of various additives on PLA's processability, heat resistance, and MPs, alongside current and prospective applications in automotive, electronics, medical, textile, and housing sectors [45].

Ferreira et al. (2021) in "Sustainability" examine the production of eco-sustainable materials from PLA/High-density biopolyethylene bioblends, improved by compatibilizing agents like poly (ethylene octene) and ethylene elastomer grafted with glycidyl methacrylate, enhancing their mechanical, and morphological properties. This study contributes to the development of environmentally friendly materials, showcasing significant improvements in impact strength and thermal stability, highlighting the potential for creating new eco-materials for sustainable development [46].

1.1.5. Chemical modifications and innovations

In their study, Harris and Lee (2010) evaluated the durability of PLA by exposing it to high temperature and humidity conditions over several weeks. Samples were exposed to conditioned environments for 1, 4, 8, and 12 weeks, during which the crystallinity content increased from 10.8% to 51%. They determined that this was due to the preferential hydrolysis of the amorphous material, increased crystallization of shorter chains, and plasticization with moisture, indicating that these results meant increased chain mobility during conditioning [47].

Porfyris et al. (2018) worked to establish a basic degradation mechanism and kinetics for the accelerated hygrothermal aging of two commercial grades of PLA, one semi-crystalline and one amorphous. During moisture and temperature conditioning at 70 °C and 80% relative humidity, they monitored water uptake, molecular weight, carboxylic end group concentration, and thermal properties, observing significant chain scission. They used an epoxy-based chain extender, an aromatic carbodiimide, and aromatic and aliphatic poly carbodiimides as additive materials. While the epoxy-based additive showed no stabilizing effect, the other three carbodiimide-based additives were found effective as anti-hydrolysis agents at a 1% concentration, especially in the amorphous grade [48].

Guo et al. (2019) aimed to enhance electrical and thermal conductivity of PLA/wood flour/thermoplastic polyurethane composites using FDM. They noted that the fracture surface of pure PLA was smooth, indicating a typical brittle fracture. Graphite appeared as flake-like layers, and graphite flakes were randomly distributed within the polymer matrix. Mechanical tests on the samples showed that tensile strength and elongation at break of composites increased with addition of 5-20% by weight of graphite, reaching a maximum with 10% graphite addition. They observed that as the graphite content increased, the continuity of matrix changed, and due to poor dispersion caused by agglomeration, the toughness of the composite decreased, and brittleness increased, similar to other studies in the field [49].

The study by Alkan Goksu (2024) explores enhancing the sustainability of PLA via ketene-based chain extension. This innovative approach addresses PLA's limited stability by increasing its molecular weight and melt viscosity through the introduction of branching. Utilizing a modular chain extender that forms highly reactive ketene intermediates, the research demonstrates a notable increase in PLA's molecular weight and improved thermal properties. These advancements suggest potential applications in packaging, highlighting the chain extender's versatility in tailoring PLA's structure for diverse applications, thereby advancing its sustainability and utility [50].

Ramezani Dana and Ebrahimi (2023) present a comprehensive review on PLA-based polymers, discussing their synthesis, properties, and applications. They delve into polymerization methods, highlighting lactic acid condensation, azeotropic dehydration, and ring-opening polymerization as key techniques. The review emphasizes PLA's mechanical, rheological, and biodegradation properties, showcasing its versatility for applications in biomedical, packaging, and additive manufacturing sectors. Authors also explore strategies for enhancing PLA's performance, such as blending and copolymerization, underscoring its potential as a sustainable alternative in various industries [51].

Table 1. Synthesizing some research efforts on PLA and its composites

Study References	Main Focus	Key Findings	Implications
Letcher and Waytashek (2014) [25]	Effects of raster orientation in 3D printing with PLA.	Orientation affects mechanical strength; 45° orientation shows highest strength.	Optimization of 3D printing parameters for desired properties.
Mansingh et al. (2023) [28]	Development of eco-friendly composites with chitin, chitosan, and PLA.	Reduction in strength and stiffness but enhanced ductility with chitin and chitosan reinforcement.	Suggests potential in food packaging, with a need for further research on MPs and interfacial bonding.
Sajna, Nayak and Mohanty (2016) [29]	Impact of nanoclay and copolymers on PLA composites' moisture absorption.	Reduced moisture absorption and mitigated mechanical property degradation.	Enhances PLA's use in environments prone to moisture.
Arrieta et al. (2017) [30]	Use of PLA and PHB blends for food packaging.	Improved barrier and MPs; potential for food packaging applications.	Provides a sustainable alternative to conventional packaging.
Ausejo et al. (2018) [31]	Print direction and layer thickness in 3D printed PLA objects.	Direction and thickness affect crystallization and MPs.	Importance of print settings in 3D printing applications.
Ayrilmis (2018) [32]	Surface roughness and wettability of 3D-printed wood flour/PLA composites.	Print thickness impacts surface smoothness and wettability.	Optimal print settings for specific application needs.
Przekop et al. (2020) [34]	PLA composites with graphite for enhanced properties.	Graphite improves wear resistance and thermal conductivity.	Expands PLA's utility in electrical and thermal applications.
Uzun and Erdoğdu (2020) [35]	MPs of copper and carbon fiber-reinforced PLA.	Reinforcements decrease tensile strength but modify PLA's mechanical properties.	Considerations for PLA composites in structural applications.
Thakur et al. (2024) [36]	Optimization of MPs in PLA-CF-PLA composites.	Successful prediction of optimal manufacturing settings via machine learning.	Significant implications for aerospace, automotive, and biomedical engineering applications.
Rajeshkumar et al. (2021) [37]	PLA-based natural fiber reinforced composites.	Highlighting the beneficial impact of natural fiber reinforcements on PLA properties.	Promoting sustainable and eco-friendly material solutions across various industries.
Rezvani Ghomi et al. (2021) [38]	Life cycle assessment of PLA.	PLA's potential to reduce greenhouse gas emissions and energy dependency.	Importance of improving recycling infrastructures and processes to minimize environmental impact.
Johansson et al. (2023) [44]	Impact of lignin acetylation on PLA biocomposites.	Acetylation improves interfacial adhesion, impact strength, thermal stability, and moisture repellency of lignin-PLA biocomposites.	Advances in creating sustainable, high-performance composite materials for automotive and aerospace applications.
Tripathi et al. (2021) [45]	Durability of PLA-based blends and biocomposites.	Advancements in enhancing PLA durability and reducing carbon footprint.	Support for a low carbon economy with potential applications in various sectors.
Ferreira et al. (2021) [46]	Production of eco-sustainable materials from PLA bioblends.	Improvements in mechanical, thermal, and morphological properties through compatibilizing agents.	Contribution to the development of new eco-materials for sustainable development.
Ramezani Dana & Ebrahimi (2023) [51]	PLA-based polymers synthesis, properties, and applications.	Discussion on polymerization methods and PLA's versatile properties.	Emphasizes PLA's potential as a sustainable alternative in biomedical, packaging, and additive manufacturing sectors.

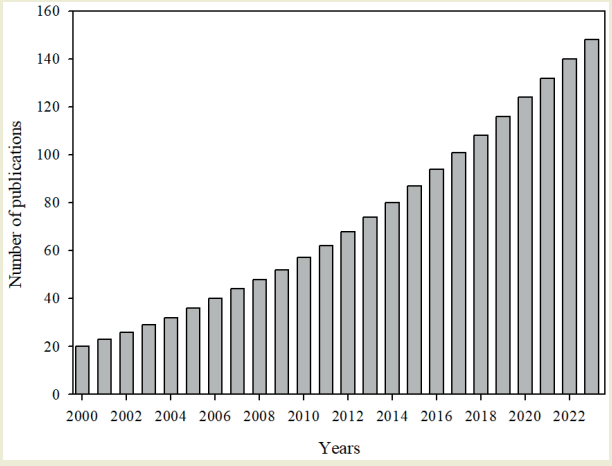

Figure 1. Number of publications on PLA sustainable applications (2000-2023 years)

Table 1 synthesizes the research efforts into PLA and its composites, emphasizing the versatility of PLA as a material for various applications, from packaging to 3D printing and beyond. It also underscores the ongoing research needs to enhance PLA's properties for specific uses, ensuring it remains a viable and sustainable alternative to traditional polymers. Figure 1 shows the developments in the number of comprehensive studies on PLA applications between 2000 and 2023.

1.1.6. Applied examples and industrial collaborations

Showcasing various case studies and partnerships that highlight PLA's potential in replacing traditional petroleum-based plastics across diverse industries. For instance, in the packaging industry, a collaboration between academic institutions and major companies has led to the development of PLA-based biodegradable

packaging, which significantly reduces carbon footprints compared to conventional materials. In the automotive sector, a project with a leading automotive manufacturer demonstrates the use of PLA composites for interior components, achieving a notable reduction in part weight and enhancing end-of-life recyclability. Additionally, in the biomedical field, collaborative efforts between research centers and medical companies have produced bioresorbable PLA implants that simplify surgical procedures and reduce overall healthcare costs. These examples not only validate PLA's versatility and sustainability but also underscore its growing acceptance and implementation in key sectors, effectively bridging the gap between research and practical deployment.

2. Discussions

The discussions around the studies on PLA and its composites touch on several critical aspects of material science, environmental sustainability, and technological advancements in polymer applications. Here are some key points of discussion derived from the findings of these studies:

Hydrolytic degradation of PLA under high humidity and temperature conditions, as observed by Harris and Lee (2010), raises important considerations for its outdoor applications or in environments where these conditions prevail [47]. This necessitates further exploration into additives or blending partners like PHB, which can enhance moisture resistance while retaining or improving PLA's biodegradability. The improvement in mechanical and thermal properties through the blending of PLA with PHB, as shown by Zhang and Thomas (2011), indicates a promising strategy for widening the use of biopolymers in more demanding applications [39]. This blending approach not only improves material properties but also supports the use of renewable resources, aligning with sustainability goals. The impact of raster orientation on MPs of 3D printed PLA objects, highlighted by Letcher and Waytashek (2014), underscores the importance of printing strategies in achieving desired performance characteristics [25]. This opens up discussions on the optimization of 3D printing parameters to tailor properties for specific applications, balancing between strength, flexibility, and material usage. Layer adhesion and porosity are critical factors affecting strength and durability of 3D printed PLA objects. The findings necessitate a deeper understanding of the relationship between printing temperature, speed, layer thickness, and the resulting microstructure of PLA objects to optimize print quality and functional performance. The studies emphasize PLA's biodegradability as a major advantage over conventional plastics, positioning it as a key player in reducing plastic pollution. However, discussions around the conditions required for PLA degradation (such as industrial composting facilities) highlight the need for improved waste management infrastructure to fully realize the environmental benefits. The addition of fillers and copolymers to PLA not only modifies its properties but also impacts its biodegradability and recycling processes. There is a need for comprehensive life cycle assessments to understand the trade-offs between improved material properties and environmental impact. The exploration of PLA composites with various fillers (such as nanoclay, graphite, and SiC) opens new avenues for research into bio-based materials with enhanced electrical, and MPs. These advancements could lead to PLA's increased adoption in electronics, automotive components, and other high-value applications. Food packaging applications of PLA and PHB blends, as researched by Arrieta et al. (2017), offer a sustainable alternative to petroleum-based packaging. Further studies could focus on the barrier properties, safety, and regulatory compliance of these materials to facilitate their acceptance and use in the food industry [30]. The role of advanced manufacturing techniques in customizing the properties of PLA for specific uses, particularly in the medical field for biocompatible implants and drug delivery systems, represents a significant area for future research. The ability to tailor PLA's degradation rate, mechanical strength, and interaction with biological tissues could lead to innovative healthcare solutions.

Mansingh et al. (2023) delve into the development of eco-friendly composites using 3D printing technology, combining PLA with chitin and chitosan. Although these additions reduce the strength and stiffness of PLA composites, they increase ductility, suggesting potential for applications such as food packaging, pending further optimization [28]. Thakur et al. (2024) focus on optimizing MPs in hybrid additive manufacturing of PLA-CF-PLA composites, employing machine learning to predict optimal fabrication parameters. Their work has significant implications for aerospace, automotive, and biomedical engineering, highlighting the versatility of PLA composites [36]. Rajeshkumar et al. (2021) and Rezvani Ghomi et al. (2021) focus on the development and life cycle assessment of PLA-based natural fiber reinforced composites, underscoring their environmental benefits and importance of enhancing recycling infrastructures [37,38]. Nandhini et al. (2023) underscore the potential of lignin and PLA in the production of bioplastics and high-value chemicals, such as muconic acid and adipic acid. Their review illuminates the environmental advantages of deriving these biopolymers from bioresources and organic waste, presenting advancements in production technologies and microbial degradation pathways [42]. Johansson et al. (2023) examine the impact of lignin acetylation on MPs of lignin-PLA biocomposites, demonstrating improvements in impact strength and thermal stability. This suggests acetylated lignin's potential in creating sustainable materials for automotive and aerospace applications [44]. Tripathi et al. (2021) and Ferreira et al. (2021) both highlight the production and development of eco-sustainable materials from PLA blends and biocomposites, emphasizing improvements in mechanical, and morphological properties and their role in supporting a low carbon economy [45,46]. Alkan Goksu (2024) explores the enhancement of PLA's sustainability through ketene-based chain extension, which improves its molecular weight and thermal properties.

This approach opens up new possibilities for PLA in packaging applications, showcasing its increased utility and sustainability [50]. Ramezani Dana and Ebrahimi (2023) present a comprehensive review on PLA-based polymers, discussing their synthesis, properties, and various applications. Their review emphasizes the versatility of PLA and strategies for enhancing its performance, further underscoring PLA's potential as a sustainable alternative in multiple industries [51].

In summary, discussions surrounding PLA and its composites revolve around balancing material properties with environmental sustainability, leveraging technological advancements for customization, and addressing the infrastructural needs for biopolymer degradation. These conversations underscore the importance of interdisciplinary research and collaboration among scientists, engineers, policymakers, and industry stakeholders to overcome current limitations and unlock the full potential of PLA in various applications.

3. Conclusions

In this comprehensive exploration of the advancements, challenges, and potential applications of PLA and its composites, alongside lignin-based materials, we have delved into the significant strides made in the realm of bioplastics. The synthesis of research findings underscores the pivotal role these materials play in the development of sustainable alternatives to conventional plastics, catering to an array of industrial applications while addressing environmental concerns. This conclusion aims to encapsulate the essence of our findings, highlighting the innovation in bioplastic properties, advancements in production technologies, environmental implications of adopting these materials, and the challenges and future directions that research in this field is poised to take.

- Investigation reveals substantial enhancements in the physical properties of PLA through various strategies, including molecular structure modifications and incorporation of natural additives and composites. Such innovations extend PLA's utility beyond its traditional confines, enabling its application in demanding sectors such as automotive, aerospace, and advanced packaging solutions. The blending of PLA with PHB and the integration of nanoclay and graft copolymers illustrate the material's improved mechanical and thermal properties, making it a formidable contender to petrochemical-based plastics.

- Progression in production technologies for PLA and lignin-based materials marks a significant milestone in the bioplastics domain. Techniques such as chain extension and acetylation enhance mechanical, thermal, and morphological properties, showcasing the potential of these biopolymers to rival traditional plastics. These advancements are instrumental in propelling bioplastics into a competitive position, offering sustainable alternatives that do not compromise on performance.

- Environmental advantages of PLA and lignin-based materials are profoundly highlighted through life cycle assessments, which advocate for their role in mitigating global warming and reducing the carbon footprint. The adoption of these materials aligns with global sustainability goals, emphasizing their importance in the transition towards a low-carbon economy. Moreover, the biodegradability of PLA presents an eco-friendly solution to plastic pollution, although the conditions under which degradation occurs necessitate further exploration to optimize application and disposal strategies.

- Despite the promising advancements, the research underscores several challenges that need addressing. The sensitivity of PLA to moisture and environmental stressors, alongside the need for enhanced MPs and durability, presents significant hurdles. Future research must focus on optimizing formulations and processing conditions for specific applications, including 3D printing and packaging, to overcome these obstacles. Additionally, the development of efficient recycling processes and the exploration of microbial degradation pathways are crucial for integrating PLA and lignin-based materials into a circular economy.

In conclusion, body of research on PLA, its composites, and lignin-based materials paints an optimistic picture of future of bioplastics. With their potential to replace conventional plastics in numerous applications, these materials stand at the forefront of the sustainability movement. However, the realization of their full potential requires a concerted effort in research and development to address the existing challenges. The path forward involves not only enhancing the properties of bioplastics but also establishing a comprehensive framework for their production, application, and disposal that prioritizes environmental integrity. As we continue to innovate and refine these materials, their role in fostering a sustainable future becomes increasingly evident, marking a significant step towards reducing our reliance on fossil-based plastics and mitigating the environmental impact of plastic pollution.

This review has collated key advancements in the development of PLA and its composites, demonstrating its potential as a sustainable alternative to petroleum-based plastics. The study emphasizes PLA's improved mechanical properties, its applicability in diverse fields like 3D printing and biomedicine, and its environmental benefits. Future research should focus on overcoming its existing limitations such as moisture sensitivity and thermal resistance, and on enhancing its recyclability. Addressing these challenges will further establish PLA as a cornerstone of sustainable material solutions.

Acknowledgments

Authors would like to thank Kastamonu University and project unit staff for the support of the project numbered KÜBAP-1/2023-18.

Research Ethics

Ethical approval not required.

Author Contributions

The author(s) accept full responsibility for the content of this article and have approved its submission.

Competing Interests

The author(s) declare that there are no competing interests.

Research Funding

Not reported.

Data Availability

Not applicable.

References

[1] Naser, A. Z., Deiab, I., & Darras, B. M. (2021). Poly (lactic acid) (PLA) and polyhydroxyalkanoates (PHAs), green alternatives to petroleum-based plastics: A review. *RSC Advances*, *11*(28), 17151-17196. https://doi.org/10.1039/D1RA02390J

[2] Wu, Y., Gao, X., Wu, J., Zhou, T., Nguyen, T. T., & Wang, Y. (2023). Biodegradable polylactic acid and its composites: Characteristics, processing, and sustainable applications in sports. *Polymers*, *15*(14), 3096. https://doi.org/10.3390/polym15143096

[3] Ilyas, R. A., Sapuan, S. M., Harussani, M. M., Hakimi, M. Y. A. Y., Haziq, M. Z. M., Atikah, M. S. N., & Asrofi, M. (2021). Polylactic acid (PLA) biocomposite: Processing, additive manufacturing and advanced applications. *Polymers*, *13*(8), 1326. https://doi.org/10.3390/polym13081326

[4] Fattahi, F. S., Khoddami, A., & Avinc, O. (2020). Sustainable, renewable, and biodegradable poly (lactic acid) fibers and their latest developments in the last decade. In *Sustainability in the Textile and Apparel Industries: Sourcing Synthetic and Novel Alternative Raw Materials* (pp. 173-194). Springer. https://doi.org/10.1007/978-3-030-38013-7_9

[5] De Smit, K., Marien, Y. W., Van Steenberge, P. H. M., D'hooge, D. R., & Edeleva, M. (2023). Playing with process conditions to increase the industrial sustainability of poly (lactic acid)-based materials. *Reaction Chemistry & Engineering*, *8*(7), 1598-1612. https://doi.org/10.1039/D2RE00577H

[6] Mehmood, A., Raina, N., Phakeenuya, V., Wonganu, B., & Cheenkachorn, K. (2023). The current status and market trend of polylactic acid as biopolymer: Awareness and needs for sustainable development. *Materials Today: Proceedings*, *72*, 3049-3055. https://doi.org/10.1016/j.matpr.2022.08.387

[7] Ebrahimi, F., & Ramezani Dana, H. (2022). Poly lactic acid (PLA) polymers: From properties to biomedical applications. *International Journal of Polymeric Materials and Polymeric Biomaterials*, *71*(15), 1117-1130. https://doi.org/10.1080/00914037.2021.1944140

[8] Ilyas, R. A., Zuhri, M. Y. M., Aisyah, H. A., Asyraf, M. R. M., Hassan, S. A., Zainudin, E. S., & Sari, N. H. (2022). Natural fiber-reinforced polylactic acid, polylactic acid blends and their composites for advanced applications. *Polymers*, *14*(1), 202. https://doi.org/10.3390/polym14010202

[9] Di Lorenzo, M. L., & Androsch, R. (2018). Industrial applications of poly (lactic acid). Cham: Springer. https://doi.org/10.1007/978-3-319-75459-8

[10] Pérez-Fonseca, A. A., Rodrigue, D., Martín Del Campo, A. S., & Robledo-Ortíz, J. R. (2024). Polylactic acid-agave fiber biocomposites: Processing, properties, weathering performance, and biodegradation. In *Polylactic Acid Composites* (pp. 13-30). De Gruyter. https://doi.org/10.1515/9783111067285-002

[11] Cao, D. (2024). Increasing strength and ductility of extruded polylactic acid matrix composites using short polyester and continuous carbon fibers. *The International Journal of Advanced Manufacturing Technology*, 1-17. https://doi.org/10.1007/s00170-023-12887-9

[12] Nagarajan, V., Mohanty, A. K., & Misra, M. (2016). Perspective on polylactic acid (PLA) based sustainable materials for durable applications: Focus on toughness and heat resistance. *ACS Sustainable Chemistry & Engineering*, *4*(6), 2899-2916. https://doi.org/10.1021/acssuschemeng.6b00321

[13] Dong, Y., Milentis, J., & Pramanik, A. (2018). Additive manufacturing of mechanical testing samples based on virgin poly (lactic acid)(PLA) and PLA/wood fibre composites. *Advances in Manufacturing*, *6*, 71-82. https://doi.org/10.1007/s40436-018-0211-3

[14] Anderson, I. (2017). Mechanical properties of specimens 3D printed with virgin and recycled polylactic acid. *3D Printing and Additive Manufacturing*, *4*(2), 110-115. https://doi.org/10.1089/3dp.2016.0054

[15] Vidakis, N., Petousis, M., Kourinou, M., Velidakis, E., Mountakis, N., Fischer-Griffiths, P. E., & Tzounis, L. (2021). Additive manufacturing of multifunctional polylactic acid (PLA)—Multiwalled carbon nanotubes (MWCNTs) nanocomposites. *Nanocomposites*, *7*(1), 184-199. https://doi.org/10.1080/20550324.2021.2000231

[16] Yılmaz, M., Yılmaz, N. F., Kılıç, A., & Mazı, H. (2024). Investigation of manufacturability of in-situ crosslinked polylactic acid (PLA) and peroxide composite in additive manufacturing. *Journal of the Faculty of Engineering and Architecture of Gazi University*, *39*(2), 859-867. https://doi.org/10.17341/gazimmfd.1213974

[17] Wang, X., Huang, L., Li, Y., Wang, Y., Lu, X., Wei, Z., & Liu, Y. (2024). Research progress in polylactic acid processing for 3D printing. *Journal of Manufacturing Processes*, *112*, 161-178. https://doi.org/10.1016/j.jmapro.2024.01.038

[18] González-López, M. A., González-López, J. A., Reyes-Morales, Q. L., Pereyra, I., & Mayen, J. (2024). Modifying the manufacturing process of high-graphite content polylactic acid filament for advanced energy and sensing applications in 3D

printing. *Polymer, 292*, 126661. https://doi.org/10.1016/j.polymer.2023.126661

[19] Demir, S., Yüksel, C., & Akpınar, F. (2024). Investigation of the mechanical response of hexagonal lattice cylindrical structure fabricated with polylactic acid 3D printing. *Journal of Materials Engineering and Performance*, 1-14. https://doi.org/10.1007/s11665-024-09155-6

[20] Bayram, M., Ustaoglu, A., Kursuncu, B., Hekimoglu, G., Sari, A., Uğur, L. O., & Ozbakkaloglu, T. (2024). 3D-printed polylactic acid-microencapsulated phase change material composites for building thermal management. *Renewable and Sustainable Energy Reviews*, *191*, 114150. https://doi.org/10.1016/j.rser.2023.114150

[21] Sharma, S., Gupta, V., Mudgal, D., & Srivastava, V. (2024). Optimization of polydopamine coating process for poly lactic acid-based 3D printed bone plates using machine learning approaches. *Polymer Engineering & Science*. https://doi.org/10.1002/pen.26546

[22] Fahim, I. S., Abdelrahman, K., Mostafa, A., & Hazem, N. (2024). Polylactic acid-based bionanocomposites: Synthesis, properties, and applications. In *Advances in Bionanocomposites* (pp. 93-116). Elsevier. https://doi.org/10.1016/B978-0-323-91764-3.00014-0

[23] Molinari, G., Parlanti, P., Aliotta, L., Lazzeri, A., & Gemmi, M. (2024). TEM morphological analysis of biopolymers: The case of Poly (Lactic Acid)(PLA). *Materials Today Communications*, *38*, 107868. https://doi.org/10.1016/j.mtcomm.2023.107868

[24] Tessanan, W., Phinyocheep, P., & Amornsakchai, T. (2024). Sustainable materials with improved biodegradability and toughness from blends of poly (lactic acid), pineapple stem starch and modified natural rubber. *Polymers*, *16*(2), 232. https://doi.org/10.3390/polym16020232

[25] Letcher, T., & Waytashek, M. (2014). Material property testing of 3D-printed specimen in PLA on an entry-level 3D printer. In *ASME International Mechanical Engineering Congress and Exposition, Proceedings (IMECE)*. https://doi.org/10.1115/IMECE2014-39379

[26] Kaygusuz, B., & Özerinç, S. (2018). 3 Boyutlu yazıcı ile üretilen PLA bazlı yapıların mekanik özelliklerinin incelenmesi. *Makine Tasarım ve İmalat Dergisi*, *16*(1), 1-6.

[27] Çiçek, Ö. Y. (2019). Eriyik yığma modelleme ile üretilen ABS ve PLA parçaların mekanik özelliklerinin değişken dolgu oranlarında karakterizasyonu ve sayısal modellemesi (Master's thesis). İstanbul Teknik Üniversitesi/Fen Bilimleri Enstitüsü, İstanbul.

[28] Mansingh, B. B., Binoj, J. S., Tan, Z. Q., Wong, W. L. E., Amornsakchai, T., Hassan, S. A., & Goh, K. L. (2023). Characterization and performance of additive manufactured novel bio-waste polylactic acid eco-friendly composites. *Journal of Polymers and the Environment*, *31*(6), 2306-2320. https://doi.org/10.1007/s10924-023-02758-5

[29] Sajna, V., Nayak, S. K., & Mohanty, S. (2016). Weathering and biodegradation study on graft copolymer compatibilized hybrid bionanocomposites of poly(lactic acid). *Journal of Materials Engineering and Performance*, *25*(7), 2895-2906. https://doi.org/10.1007/s11665-016-2151-z

[30] Arrieta, M. P., Samper, M., Aldas, M., & López, J. (2017). On the use of PLA-PHB blends for sustainable food packaging applications. *Materials*, *10*(9), 10087. https://doi.org/10.3390/ma10091008

[31] Ausejo, J. G., Rydz, J., Musioł, M., Sikorska, W., Janeczek, H., Sobota, M., Włodarczyk Szeluga, J. U., Hercog, A., & Kowalczuk, M. (2018). Three-dimensional printing of PLA and PLA/PHA dumbbell-shaped specimens of crisscross and transverse patterns as promising materials in emerging application areas: Prediction study. *Polymer Degradation and Stability, 156*, 100-110. https://doi.org/10.1016/j.polymdegradstab.2018.08.008

[32] Ayrilmis, N. (2018). Effect of layer thickness on surface properties of 3D printed materials produced from wood flour/PLA filament. *Polymer Testing, 71*, 163-166. https://doi.org/10.1016/j.polymertesting.2018.09.009

[33] Patan, Z. Y. (2019). Karbon fiber takviyeli ABS kompozitlerin FDM 3D yazıcı ile üretimi ve Ansys ile modellenmesi (Master's thesis). Çanakkale Onsekiz Mart Üniversitesi/Fen Bilimleri Enstitüsü, Çanakkale.

[34] Przekop, R. E., Kujawa, M., Pawlak, W., Dobrosielska, M., Sztorch, B., & Wieleba, W. (2020). Graphite modified polylactide (PLA) for 3D printed (FDM/FFF) sliding elements. *Polymers*, *12*(6), 1250. https://doi.org/10.3390/polym12061250

[35] Uzun, M., & Erdoğdu, Y. E. (2020). Eriyik yığma modellemesi ile üretimde takviyesiz ve takviyeli PLA kullanımının mekanik özelliklere etkisinin araştırılması. *Iğdır Üniversitesi Fen Bilimleri Enstitüsü Dergisi*, *10*(4), 2800-2808. https://doi.org/10.21597/jist.799230

[36] Thakur, V., Kumar, R., Kumar, R., Singh, R., & Kumar, V. (2024). Hybrid additive manufacturing of highly sustainable polylactic acid-carbon fiber-polylactic acid sandwiched composite structures: Optimization and machine learning. *Journal of Thermoplastic Composite Materials*. https://doi.org/10.1177/08927057231180186

[37] Rajeshkumar, G., Seshadri, S. A., Devnani, G. L., Sanjay, M. R., Siengchin, S., Maran, J. P., ... & Anuf, A. R. (2021). Environment friendly, renewable and sustainable poly lactic acid (PLA) based natural fiber reinforced composites–A comprehensive review. *Journal of Cleaner Production, 310*, 127483. https://doi.org/10.1016/j.jclepro.2021.127483

[38] Rezvani Ghomi, E., Khosravi, F., Saedi Ardahaei, A., Dai, Y., Neisiany, R. E., Foroughi, F., ... & Ramakrishna, S. (2021). The life cycle assessment for polylactic acid (PLA) to make it a low-carbon material. *Polymers*, *13*(11), 1854. https://doi.org/10.3390/polym13111854

[39] Zhang, M., & Thomas, N. L. (2011). Blending polylactic acid with polyhydroxybutyrate: The effect on thermal, mechanical, and biodegradation properties. *Advances in Polymer Technology*, *30*(2), 67-79. https://doi.org/10.1002/adv.20235

[40] Kamau-Devers, K., Kortum, Z., & Miller, S. A. (2019). Hydrothermal aging of bio-based poly(lactic acid) (PLA) wood polymer composites: Studies on sorption behavior, morphology, and heat conductance. *Construction and Building Materials, 214*, 290-302. https://doi.org/10.1016/j.conbuildmat.2019.04.098

[41] Kakanuru, P., & Pochiraju, K. (2020). Moisture ingress and degradation of additively manufactured PLA, ABS and PLA/SiC composite parts. *Additive Manufacturing*, *36*, 101529. https://doi.org/10.1016/j.addma.2020.101529

[42] Nandhini, R., Sivaprakash, B., Rajamohan, N., & Vo, D. V. N. (2023). Lignin and polylactic acid for the production of bioplastics and valuable chemicals. *Environmental Chemistry Letters*, *21*(1), 403-427. https://doi.org/10.1007/s10311-022-01505-x

[43] Siracusa, V., Karpova, S., Olkhov, A., Zhulkina, A., Kosenko, R., & Iordanskii, A. (2020). Gas transport phenomena and poly-

mer dynamics in PHB/PLA blend films as potential packaging materials. *Polymers*, *12*(3), 647. https://doi.org/10.3390/polym12030647

[44] Johansson, M., Skrifvars, M., Kadi, N., & Dhakal, H. N. (2023). Effect of lignin acetylation on the mechanical properties of lignin-poly-lactic acid biocomposites for advanced applications. *Industrial Crops and Products*, *202*, 117049. https://doi.org/10.1016/j.indcrop.2023.117049

[45] Tripathi, N., Misra, M., & Mohanty, A. K. (2021). Durable polylactic acid (PLA)-based sustainable engineered blends and biocomposites: Recent developments, challenges, and opportunities. *ACS Engineering Au*, *1*(1), 7-38. https://doi.org/10.1021/acsengineeringau.1c00011

[46] Ferreira, E. D. S. B., Luna, C. B. B., Siqueira, D. D., dos Santos Filho, E. A., Araújo, E. M., & Wellen, R. M. R. (2021). Production of eco-sustainable materials: Compatibilizing action in poly (lactic acid)/high-density biopolyethylene bioblends. *Sustainability*, *13*(21), 12157. https://doi.org/10.3390/su132112157

[47] Harris, A. M., & Lee, E. C. (2010). Heat and humidity performance of injection molded PLA for durable applications. *Journal of Applied Polymer Science*, *115*, 1380-1389. https://doi.org/10.1002/app.30815

[48] Porfyris, A., Vasilakos, S., Zotiadis, C., Papaspyrides, C., Moser, K., Schueren, L., Buyle, G., Pavlidou, S., & Vouyiouka, S. (2018). Accelerated ageing and hydrolytic stabilization of poly(lactic acid) (PLA) under humidity and temperature conditioning. *Polymer Testing*, *68*, 315-332. https://doi.org/10.1016/j.polymertesting.2018.04.018

[49] Guo, R., Ren, Z., Bi, H., Xu, M., & Cai, L. (2019). Electrical and thermal conductivity of polylactic acid (PLA)-based bio composites by incorporation of nano-graphite fabricated with fused deposition modeling. *Polymers*, *11*(3), 549. https://doi.org/10.3390/polym11030549

[50] Alkan Goksu, Y. (2024). Enhancing the sustainability of poly (lactic acid) (PLA) through ketene-based chain extension. *Journal of Polymers and the Environment*, 1-14. https://doi.org/10.1007/s10924-023-03171-8

[51] Ramezani Dana, H., & Ebrahimi, F. (2023). Synthesis, properties, and applications of polylactic acid-based polymers. *Polymer Engineering & Science*, *63*(1), 22-43. https://doi.org/10.1002/pen.26193